DISSERTATION

MEASUREMENT OF MUON NEUTRINO CHARGED-CURRENT NEUTRAL PION PRODUCTION IN LIQUID ARGON WITH THE ICARUS T600 DETECTOR AT FERMILAB

Submitted by

Lane M. Kashur

Department of Physics

In partial fulfillment of the requirements

For the Degree of Doctor of Philosophy

Colorado State University

Fort Collins, Colorado

Spring 2026

Doctoral Committee:

Advisor: Michael Mooney

Joshua Berger
Kazuhiro Terao
Mahdi Nikdast

ABSTRACT

MEASUREMENT OF MUON NEUTRINO CHARGED-CURRENT NEUTRAL PION PRODUCTION IN LIQUID ARGON WITH THE ICARUS T600 DETECTOR AT FERMILAB

At ICARUS and the broader Short-Baseline Neutrino Program, few neutrino interaction channels offer as much utility as those producing neutral pions, which are an important background to electron neutrino searches and provide a standard candle for calibrating the electromagnetic shower energy scale. Beyond this, measurements of neutrino-induced neutral pions offer a probe of resonant interactions that are relevant to future accelerator neutrino experiments like the Deep Underground Neutrino Experiment. In this thesis, a measurement of charged-current muon neutrino interactions in liquid argon with a single neutral pion in the final state is presented, making use of neutrino interaction events recorded with the ICARUS T600 detector at Fermilab while exposed to the Booster Neutrino Beam. Event selection is carried out with a fully-automated machine learning reconstruction framework, allowing for the extraction of single-differential cross section measurements as a function of muon and neutral pion kinematic observables.

ACKNOWLEDGEMENTS

This PhD would not be possible without the support of many colleagues, friends, and family members. I'm appreciative of my committee for providing technical feedback on my analysis over the years while remaining approachable and down to earth. My advisor, Mike Mooney, has been a constant source of knowledge and guidance during my PhD. Despite having research interests across multiple experiments and managing a small army of students, Mike was always sure to set time aside to discuss projects and check in to see how things were going. I'm fortunate to have worked alongside other members of Mike's research group at CSU, and would particularly like to thank Justin Mueller for always being available with advice and Dan Carber for going through the trenches of analysis development with me.

My understanding of experimental neutrino physics has been shaped by the incredible scientists, engineers, and technicians in the SBND, ICARUS, and DUNE collaborations. While there are far too many to name, I owe special thanks to a select few who consistently went above and beyond to support my research goals. Early in my PhD, the technical prowess and engineering ingenuity of Jay Jablonksi and Dave Warner was crucial for getting the Colorado Argon Test Stand up and running for the first time. At Fermilab, Vito Di Benedetto's guidance on computing practices and unfailing accessibility have enabled many of the workflows employed in my analyses. The same can be said for Geoff Savage, who is perhaps one of the busiest people at the lab due to his invaluable operational support of multiple experiments. I am also grateful to the SLAC group for their expertise in LArTPC event reconstruction. In particular, tireless efforts from Francois Drielsma have paved the way for physics measurements like the ones presented in this thesis and beyond. Similarly, I'd like to thank Jaesung Kim for serving as an indispensable point of reference for neutrino cross section extraction procedures.

My time at CSU and Fermilab has introduced me to many colleagues that are now some of my closest friends. At CSU, my graduate school cohort included members of the infamous party office. Many shenanigans were had with Evan, Byron, Tarkon, and Andrew, and I wouldn't trade

the camping trips or after-work beers with this group for anything. The Fermilab-based real-sbnd also deserves a special acknowledgment. Known for organizing the Coloma collaboration meeting, this group has shown me that living in Illinois isn't so bad if you're surrounded by the right people.

Most importantly, I am tremendously grateful to my family for their unconditional support over the course of my academic career. This includes my dad and stepmom, Matt and Brenda, who never questioned my choice to pursue a PhD in experimental particle physics, even if it made explaining what your son does for a living a bit tricky at times. My mom, Deb, has been my biggest cheerleader through thick and thin, supporting me in every endeavor. Finally, I am forever indebted to my wife, Lan, for her infinite patience, encouragement, and reassurance when the going got tough during my PhD. Words can't describe how much it's meant to have you by my side these last few years and I can't wait to see what's in store next for us.

DEDICATION

To my friends and family, whose support has been unwavering over my academic career.

TABLE OF CONTENTS

LIST OF TABLES

LIST OF FIGURES

Chapter 1

Introduction

Serving as the far detector for the Short-Baseline Neutrino (SBN) Program, ICARUS is a neutrino detector designed to address anomalous results from the LSND and MiniBooNE experiments, where excesses of electron-like events could possibly be interpreted as originating from light sterile neutrinos. One key to resolving these anomalies is the search for electron neutrinos in a predominantly muon neutrino beam, for which ICARUS and the Short-Baseline Near Detector (SBND) rely on liquid argon time projection chamber (LArTPC) technology. With excellent calorimetry and fine-grained spatial resolution, LArTPCs allow for the precise measurement of electron neutrino interactions at ICARUS.

Equally important to the success of ICARUS is characterization of backgrounds that can mimic the electron neutrino appearance signal. Primary among these backgrounds is the production of neutral pions, or π^0s, which predominantly decay electromagnetically to photons. Neutral pion production is mostly attributed to baryon resonances in neutrino-nucleon interactions that occur at the GeV scale, which is also the relevant energy scale for the upcoming Deep Underground Neutrino Experiment (DUNE). An ICARUS analysis centered around neutral pions therefore not only informs us about the SBN Program's most significant background, but also provides a probe for the types of neutrino interactions expected at next-generation oscillation experiments.

This thesis reports the flux-averaged differential cross section measurement of charged-current muon neutrino interactions in liquid argon with a single π^0 in the final state, hereafter referred to as ν_μ CC π^0 interactions:

$$\nu_\mu + \mathrm{Ar} \rightarrow 1\mu^- + 1\pi^0 + 0\pi^\pm + X. \tag{1.1}$$

Here, X represents any final state particles that are not muons or charged pions. The omittance of charged pions in the final state aims to exclude charged-current coherent pion production from the analysis, therefore allowing the cross section measurement to probe the resonant production mode

that is more relevant to the SBN Program. While similar topologies involving muon antineutrinos are indistinguishable in LArTPCs, the flux is comparatively smaller ($\sim$6%, see Section 4.2) and neutrino cross sections are typically twice as a large as antineutrino cross sections [1].

Few charged-current π^0 measurements exist on liquid argon, and a high-statistics cross section measurement of this channel at ICARUS will help constrain uncertainties in modeling resonant neutrino-nucleon interactions. The ν_μ CC π^0 differential cross section measurement as a function of muon and neutral pion kinematic variables is reported in this work, with event selection being carried out by a novel machine-learning reconstruction framework. Benefiting from high purity and excellent resolution in reconstructed variables, this selection makes the extraction of precise, finely-binned differential cross sections possible.

Organization of this thesis as is follows. Chapter 2 introduces the physics of neutrinos and their interactions with matter, as well as the phenomenon of neutrino oscillation. Chapter 3 highlights neutrino oscillation experiments, with an emphasis on accelerator neutrino experiments. The SBN Program and the LArTPC technology are discussed in Chapter 4, while the ICARUS detector is described in Chapter 5. Chapter 6 details the simulation and reconstruction of neutrino interactions at ICARUS, followed by an overview of the ICARUS calibration program in Chapter 7. Chapter 8 introduces the ν_μ CC π^0 selection, and Chapter 9 discusses systematic uncertainties relevant to the selection. The culmination of this work is presented in Chapter 10 with the ν_μ CC π^0 cross section measurement, followed by concluding remarks in Chapter 11.

Chapter 2

Neutrino Physics

This chapter provides an overview of neutrino physics, including a review of the Standard Model and significant milestones in the field for historical context. Section 2.1 introduces basic properties of the neutrino and its placement in the Standard Model. Section 2.2 provides an overview of neutrino interactions with matter and introduces modes of neutral pion production. Finally, Section 2.3 highlights the phenomenology of neutrino oscillations.

2.1 Neutrinos and the Standard Model

Neutrinos are elementary particles, or subatomic particles that are not composed of any smaller constituents. Elementary particles and the fundamental forces that govern their interactions are described by the Standard Model of particle physics, a theoretical framework rooted in quantum field theory. The Standard Model broadly contains two classes of particles: fermions and bosons. Fermions are half-integer spin particles that obey Fermi-Dirac statistics, and can be further divided into three generations of quarks and leptons. The quarks include up/down quarks, strange/charm quarks, and bottom/top quarks in the first, second, and third generations, respectively. Leptons include the electron and electron neutrino, the muon and muon neutrino, and the tau particle and tau neutrino. In contrast, bosons have integer spin and obey Bose-Einstein statistics. Gauge bosons act as force carriers and include gluons, photons, and $W^{\pm}$/Z bosons which mediate the strong, electromagnetic, and weak forces, respectively. The Standard Model also includes one scalar boson, the Higgs boson, a manifestation of the Higgs field that is responsible for most massive elementary particles acquiring their mass. Figure 2.1 shows the Standard Model particles and a summary of their properties. Particles in the Standard Model also have antiparticle counterparts with the same mass but opposite charge-like quantum numbers, with the exception that certain particles are their own antiparticles. Antiparticles are not explicitly shown in Figure 2.1, but are typically denoted by the placement of a bar over the relevant particle symbol (e.g. $\bar{\nu}_e$ is an electron antineutrino).

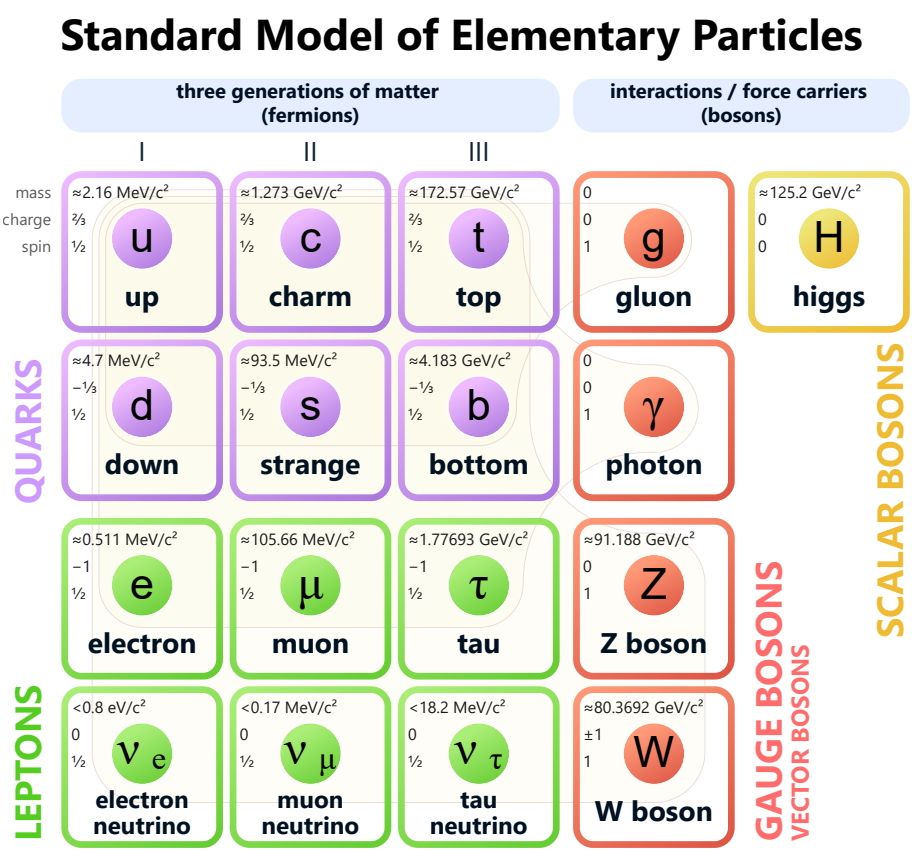

Figure 2.1: The Standard Model of particle physics. Image from Wikimedia Commons.

Within the Standard Model, neutrinos are neutral leptons. Given photons couple directly to charged particles to mediate the electromagnetic force, the neutrino's absence of electric charge means it does not interact electromagnetically. Nor are neutrinos subject to strong interactions, a property reserved for quarks due to the color charge they carry. Instead, neutrinos interact almost exclusively through the weak interaction force via couplings to $W^{\pm}$ and Z bosons. It is worth noting that as massive particles, neutrinos are also subject to the force of gravity, though mention of two caveats is warranted. For one, the gravitational force is not included in the Standard Model and a "graviton" force carrier has yet to be discovered. Secondly, the mass of the neutrino is miniscule, and was long assumed to be zero. Cosmological constraints limit the three flavor-mass sum to be less than 0.12 eV [2], which is less than one millionth the mass of the electron.

2.2 Interactions with Matter

Interactions between neutrinos and other matter particles occur via the weak interaction force, as mentioned in the previous section. As an example, consider the case of inverse beta decay - the process through which the neutrino was discovered by Frederick Reines and Clyde Cowan in 1956 [3]. In this process, an antineutrino scatters off a proton by exchanging a W^- boson, resulting in a positron and neutron as shown in Equation 2.1.

$$\bar{\nu}_e + p \rightarrow e^+ + n \tag{2.1}$$

Being mediated by the electrically-charged W boson, inverse beta decay and similar interactions are called *charged-current* (CC) interactions. In the context of neutrino scattering with ordinary matter (e.g. protons, neutrinos, and electrons), charged-current interactions are characterized by the conversion of a neutrino into its corresponding lepton, or vice versa. On the other hand, if an interaction involving a neutrino is mediated by the electrically-neutral Z boson, the interaction is referred to as being *neutral-current* (NC), and no lepton conversion occurs. Depictions of charged-current and neutral-current neutrino interactions with matter are shown in Figure 2.2, where A is a nuclear target and X represents resultant final-state particles.

Further classification of neutrino interactions is possible when the elasticity of the interaction is considered. Broadly speaking, the lower the energy of the involved neutrino, the more likely an interaction is to be "elastic", meaning the nuclear target remains intact and no new particles are

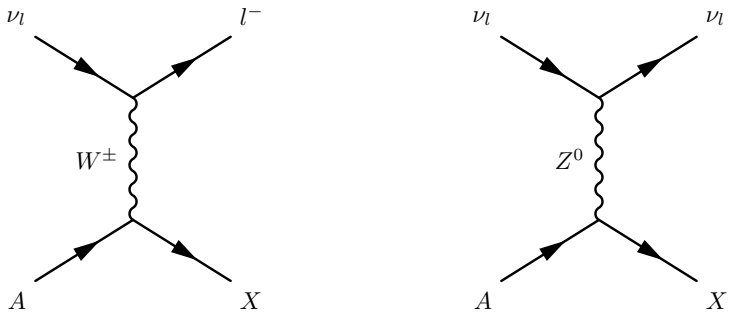

Figure 2.2: Feynman diagrams for charged-current (left) and neutral-current (right) neutrino interactions.

created. Conversely, higher-energy neutrinos transfer more energy to nuclear targets, increasing the probability for the interaction to be "inelastic" and for the set of particles in the final state to be different than those in the initial state. Distinct neutrino interaction modes are listed below, with dominant modes shown as a function of neutrino energy in Figure 2.3.

- **Coherent Elastic Scattering (CEvNS):** Interaction in which an incident neutrino scatters off a nucleus, which then recoils as a whole. No other final-state particles are produced. CEvNs has been probed using targets ranging from argon to cesium, and is seen to occur for incident neutrino energies up to approximately 50 MeV for medium-sized nuclei such as these.

- **Quasielastic Scattering (QE):** Interaction in which an incident neutrino scatters off an individual proton or neutron within the nucleus; also known as 1 particle and 1 hole (1p1h). This is the dominant interaction mode for neutrinos with energy less than 1 GeV. Pure QE interactions can also be mimicked by "QE-like" interactions featuring multinucleon final states, such as meson exchange currents (MEC) involving 2 particles and 2 holes (2p2h).

- **Resonant Production (RES):** Interaction in which an incident neutrino scatters off an individual proton or neutron within the nucleus, with the neutrino energy sufficient enough to excite a baryon resonance. The baryon resonance quickly decays into a nucleon-pion pair most typically. This interaction mode is dominant for neutrino energies in the 1–4 GeV range.

- **Coherent Pion Production (COH):** Interaction in which an incident neutrino scatters inelastically off the nucleus, which then recoils as a whole. COH results in a forward-going lepton and pion and has been observed over a wide range of energies, despite contributing less to the total neutrino-nucleus cross section than resonant interactions.

- **Deep Inelastic Scattering (DIS):** Interaction in which an incident neutrino scatters off individual quarks within protons and neutrons inside of the nucleus. DIS is capable of producing

many outgoing hadrons and is the dominant interaction mode for neutrinos with energies greater than 5 GeV.

2.2.1 Modes of CC π^0 Production

Charged-current neutral pion production occurs directly through resonant interactions and deep inelastic scattering, with the dominant mode at energies relevant to the SBN Program being resonant production. To highlight this, Figure 2.4 shows the breakdown of signal ν_μ CC π^0 events by interaction mode in an ICARUS simulation of neutrinos from the Booster Neutrino Beam (BNB) - the primary neutrino beam of the SBN Program. Approximately 85% of signal events are estimated to be resonant in origin, roughly a factor of eight greater than those produced through DIS. The vast majority of neutral pions at ICARUS specifically emanate from the $\Delta(1232)$ resonance, which has a mass of 1.232 GeV and decays via the strong interaction to a nucleon and pion in approximately 10^{-23} seconds. Feynman diagrams associated with these resonant interactions are

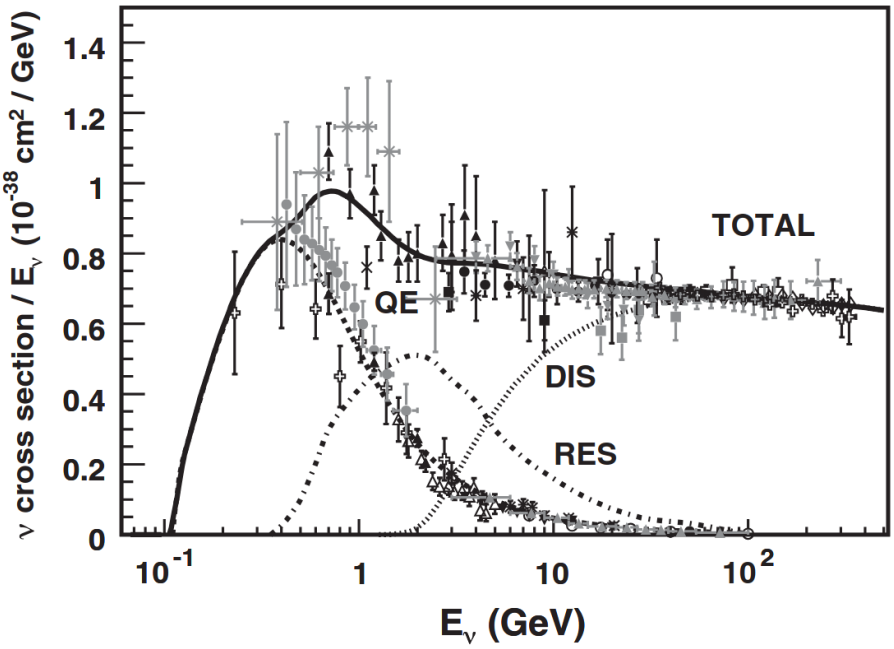

Figure 2.3: Measured quasielastic and total cross sections for charged-current neutrino interactions on a variety of target nuclei as a function of neutrino energy. Also shown are simulated predictions for the contributing processes [1].

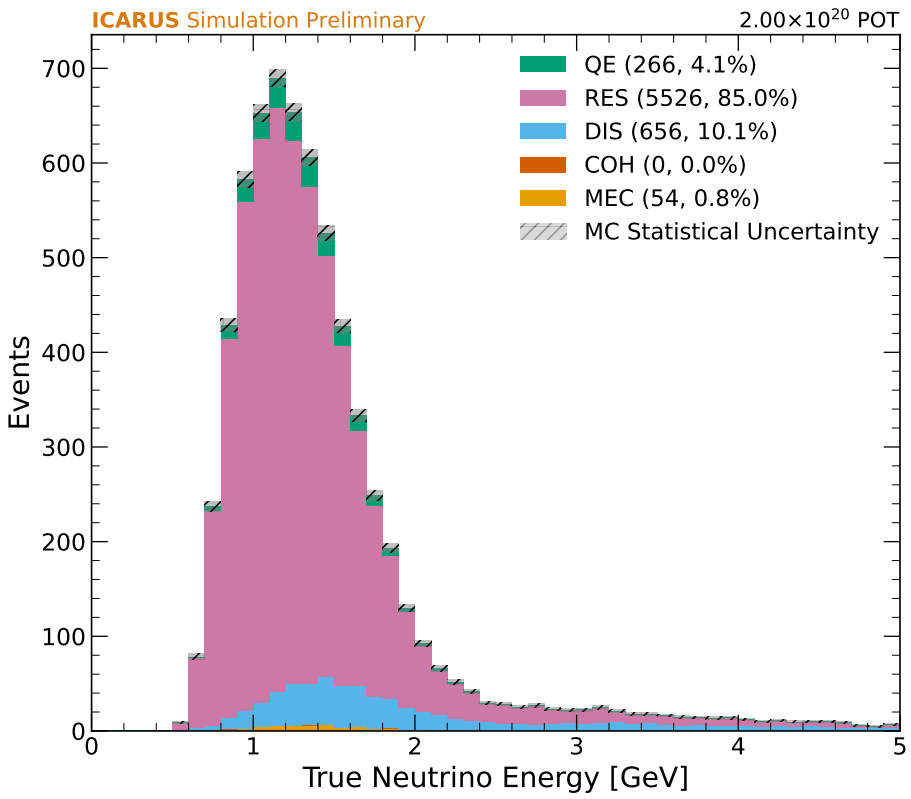

Figure 2.4: Interaction type breakdown of ν_μ CC π^0 interactions as a function of neutrino energy using ICARUS BNB simulation. The number of events is scaled to 2×10^{20} protons on target.

depicted in Figure 2.5. More on the modeling of this resonance, as well as the ICARUS simulation in general, can be found in Section 6.1.

Additionally, quasielastic and meson exchange current interactions can produce final-state topologies that include neutral pions. These neutral pions are not produced as primary particles, but are instead the result of hadronic re-interactions within the nucleus known as final-state interactions (FSI). As an example, consider a muon neutrino CCQE interaction in which a muon and proton are produced through the exchange of a W boson with a neutron. The recoiling proton has a nonzero chance of re-interacting with another nucleon, producing a charged pion in the process. Then, the charged pion may undergo a charge-exchange interaction (e.g. $\pi^+ + n \rightarrow \pi^0 + p$), resulting in a final-state neutral pion. Pion absorption can also indirectly lead to final states containing single neutral pions, such as the case of a DIS interaction producing a charged pion and neutral pion, where only the neutral pion escapes the nucleus.

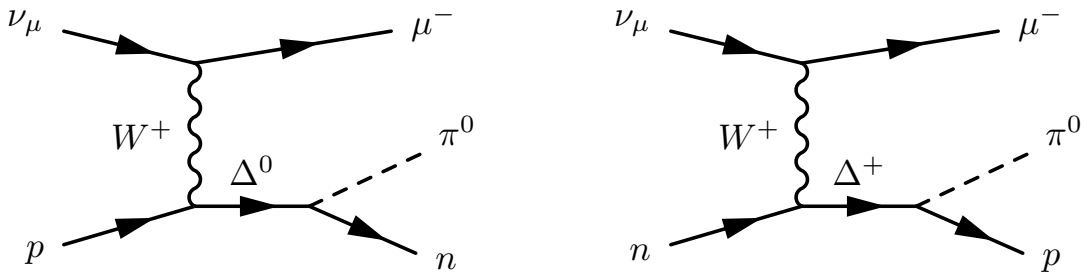

Figure 2.5: Example Feynman diagrams for resonant π^0 production.

2.2.2 Previous ν_μ CC π^0 Measurements

Measurements of CC π^0 production have been reported previously by a small number of experiments. In 2011, the K2K collaboration reported the ratio of the inclusive CC π^0 cross section to the CCQE cross section on a polystyrene target [4]. The same year, total and differential cross sections on mineral oil were measured for a semi-inclusive CC π^0 selection by the MiniBooNE collaboration [5]. The MINERvA collaboration would similarly report semi-inclusive CC π^0 measurements the following year using hydrocarbon as the nuclear target [6]. Most recently, the MicroBooNE collaboration has measured CC π^0 production on argon, including an inclusive total cross section measurement and semi-inclusive differential cross section measurement [7]. A summary of previous measurements can be found in Table 2.1.

The ICARUS BNB ν_μ CC π^0 measurement presented in this thesis provides a valuable addition to the aforementioned data points. While first results correspond to an exposure of approximately 2×10^{19} protons on target (POT), the projected exposure of the final analysis is a factor of ten larger (see Chapter 8). Given the statistics of the target dataset and the comparatively higher selection efficiency relative to previous analyses (see Section 8.3), it is expected that this analysis will result in the largest sample of neutrino-induced neutral pions on argon to-date. Furthermore, an adjacent selection has been developed in parallel for the near detector of the SBN Program, the Short-Baseline Near Detector (SBND). The SBND ν_μ CC π^0 analysis will culminate in the

Experiment	Target	POT [e20]	E_ν [GeV]	Signal	Measurement(s)
K2K	C_8H_8	0.20	1.3	$1\mu^- X\pi^0$	$\frac{\sigma_{CC\pi^0}}{\sigma_{CCQE}}(E_\nu)$
MiniBooNE	CH_2	6.27	0.965	$1\mu^- 1\pi^0 0\pi^\pm$	$\langle\sigma\rangle_\Phi$, $\sigma(E_\nu)$, $\frac{d\sigma}{dx}$
MINERvA	CH	3.04	3.6	$1\mu^- 1\pi^0 0\pi^\pm$	$\sigma(E_\nu)$, $\frac{d\sigma}{dx}$
MicroBooNE	Ar	6.86	0.8	$1\mu^- 1\pi^0 0\pi^\pm$	$\langle\sigma\rangle_\Phi$, $\frac{d\sigma}{dx}$

Table 2.1: Summary of previous ν_μ CC π^0 measurements. In the "Signal" column, X indicates signifies at least one neutral pion. In the "Measurement(s)" column, $\sigma(E_\nu)$ is the total cross section as a function of neutrino energy, $\langle\sigma\rangle_\Phi$ is the flux-averaged total cross section, and $\frac{d\sigma}{dx}$ is the flux-averaged differential cross section as a function of x (typically muon or neutral pion kinematic observables).

most statistically significant measurement of neutrino-induced neutral pions, regardless of nuclear target.

2.3 Neutrino Oscillations

Neutrino oscillations refer to the phenomenon of neutrinos changing flavor, or oscillating, as they travel through space and matter. That is to say, a neutrino produced with initial flavor α may be detected as a different flavor β after traveling some distance. The first observation of neutrino oscillations was by Ray Davis in the late 1960s as part of the Homestake experiment, where electron neutrinos from the Sun could be detected via inverse beta decay in a large tank of cleaning fluid [8]. While the Homestake experiment was able to successfully count solar neutrinos for the first time, the measured flux of these neutrinos was only a third of that predicted by the Standard Solar Model (SSM). This became known as the "solar neutrino problem" and its solution would not be found for more than three decades. In 2001, the Sudbury Neutrino Observatory (SNO) measured the fraction of electron neutrinos from the Sun to be consistent with the SSM [9]. This was possible due to the capability of SNO to measure the flux of all neutrino flavors instead of solely electron neutrinos. In conjunction with findings from the Super-Kamiokande experiment that showed the flux of atmospheric neutrinos to be dependent on zenith angle [10], these results provided conclusive proof for neutrino oscillations and resolved the solar neutrino problem.

Neutrino oscillations are a consequence of flavor mixing, which refers to the fact that the three known flavors of neutrinos, ν_e, ν_μ, and ν_τ, are superpositions of three neutrino mass eigenstates,

ν_1, ν_2, and ν_3. Flavor and mass eigenstates are related by a unitary 3×3 mixing matrix:

$$|\nu_\alpha\rangle = \sum_j U_{\alpha j} |\nu_j\rangle \tag{2.2}$$

$$|\nu_j\rangle = \sum_\alpha U^*_{\alpha j} |\nu_\alpha\rangle \tag{2.3}$$

where α and j enumerate the flavor and mass basis states, respectively. Known as the Pontecorvo-Maki-Nakagawa-Sakata (PMNS) matrix, U is typically parametrized by three mixing angles, θ_{12}, θ_{23}, and θ_{13}, and one phase, δ_{CP}. The mixing angles describe the degree of mixing between neutrino flavors, while δ_{CP} describes the degree of charge-parity (CP) violation (if any) in the leptonic sector. In its expanded form, the PMNS matrix can be written as

$$\begin{aligned}
U &= \begin{bmatrix} U_{e1} & U_{e2} & U_{e3} \\ U_{\mu 1} & U_{\mu 2} & U_{\mu 3} \\ U_{\tau 1} & U_{\tau 2} & U_{\tau 3} \end{bmatrix} \\
&= \begin{bmatrix} 1 & 0 & 0 \\ 0 & \cos\theta_{23} & \sin\theta_{23} \\ 0 & -\sin\theta_{23} & \cos\theta_{23} \end{bmatrix} \begin{bmatrix} \cos\theta_{13} & 0 & \sin\theta_{13} e^{-i\delta_{\text{CP}}} \\ 0 & 1 & 0 \\ -\sin\theta_{13} e^{i\delta_{\text{CP}}} & 0 & \cos\theta_{13} \end{bmatrix} \begin{bmatrix} \cos\theta_{12} & \sin\theta_{12} & 0 \\ -\sin\theta_{12} & \cos\theta_{12} & 0 \\ 0 & 0 & 1 \end{bmatrix} \\
&= \begin{bmatrix} c_{12}c_{13} & s_{12}c_{13} & s_{13}e^{-i\delta_{\text{CP}}} \\ -s_{12}c_{23} - c_{12}s_{23}s_{13}e^{i\delta_{\text{CP}}} & c_{12}c_{23} - s_{12}s_{23}s_{13}e^{i\delta_{\text{CP}}} & s_{23}c_{13} \\ s_{12}s_{23} - c_{12}c_{23}s_{13}e^{i\delta_{\text{CP}}} & -c_{12}s_{23} - s_{12}c_{23}s_{13}e^{i\delta_{\text{CP}}} & c_{23}c_{13} \end{bmatrix}
\end{aligned} \tag{2.4}$$

where $c_{ij} \equiv \cos\theta_{ij}$ and $s_{ij} \equiv \sin\theta_{ij}$.

The time-dependent Schrödinger equation states that the evolution of a neutrino flavor eigenstate in time under the assumption of a vacuum is given by

$$|\nu_\alpha(t)\rangle = \sum_j U_{\alpha j} e^{-i(E_j t - p_j L)} |\nu_j(0)\rangle \approx \sum_j U_{\alpha j} e^{-i\frac{m_j^2 L}{2E}} |\nu_j(0)\rangle\,, \tag{2.5}$$

where E, p, and m represent the energy, momentum, and mass of each neutrino mass eigenstate, respectively. The distance the neutrino has traveled since creation is denoted by L, the baseline. The final approximation is valid under the assumption of relativistic neutrinos with mass eigenstates treated as plane waves of constant energy. Then, the probability of a neutrino being detected in flavor state β after being produced in flavor state α and traveling for time t in a vacuum is given by the absolute square of the amplitude $\langle \nu_\beta | \nu_\alpha(t) \rangle$:

$$\begin{aligned} P(\nu_\alpha \to \nu_\beta) &= |\langle \nu_\beta | \nu_\alpha(t) \rangle|^2 \\ &= \delta_{\alpha\beta} - 2 \sum_j \sum_k Re(U^*_{\alpha j} U_{\beta j} U_{\alpha k} U^*_{\beta k}) \sin^2(\frac{\Delta m^2_{jk} L}{4E}) \\ &+ 2 \sum_j \sum_k Im(U^*_{\alpha j} U_{\beta j} U_{\alpha k} U^*_{\beta k}) \sin^2(\frac{\Delta m^2_{jk} L}{2E}), \end{aligned} \tag{2.6}$$

where Δm^2_{jk} is the squared mass difference, or $m^2_j - m^2_k$.

From Equation 2.6, it can be seen that the probability of three-flavor neutrino oscillation directly depends on six parameters: three mixing angles $\{\theta_{12}, \theta_{13}, \theta_{23}\}$, two squared mass differences $\{\Delta m^2_{21}, \Delta m^2_{31}\}$, and a single complex phase δ_{CP}. The imaginary term in Equation 2.6 vanishes in the case of $\delta_{\text{CP}} = 0$ or π, while any other values imply the presence of CP-violation in the neutrino sector. The oscillation probability is additionally dependent on the neutrino baseline (L) and energy (E), which can serve as controllable parameters in the design of specific neutrino oscillation experiments, as will be discussed in the following chapter.

Given Equation 2.6 depends on the magnitude of Δm^2_{jk} and not its sign, oscillations in a vacuum are insensitive to the sign of Δm^2_{21} and Δm^2_{31}. This is not the case for neutrino oscillations in matter, where neutrinos are subject to a potential that arises from charged-current coherent forward scattering with electrons in dense media. As the neutrinos propagate through the material, their oscillation probability is governed by effective parameters that depend on both the potential and the sign of the relevant squared mass difference, as opposed to the vacuum parameters introduced previously. Solar neutrino experiments, which are introduced in Section 3.1.1, have relied on the prominence of this effect for neutrinos traversing the solar medium in order to determine

the sign of Δm^2_{21}, which is now known to be positive. The sign of Δm^2_{31} has yet to be determined, meaning a degeneracy exists in the ordering of the Standard Model neutrino masses. The scenario where $m_1 < m_2 < m_3$ is typically referred to as "normal mass ordering", whereas the condition $m_3 < m_1 < m_2$ is referred to as "inverted mass ordering". Along with determining the degree of CP-violation in the neutrino sector, resolving the neutrino mass ordering is a primary goal of future oscillation experiments.

Chapter 3

Neutrino Oscillation Experiments

Neutrino oscillation experiments are designed to measure the neutrino flavor mixing parameters and resolve the neutrino mass ordering. These experiments may vary by neutrino source and baseline, but generally fall under two main classifications: appearance and disappearance experiments. Neutrino appearance experiments utilize neutrino sources of predominantly one flavor and search for different flavors after traveling a defined distance, while neutrino disappearance experiments measure the reduction in flux of a particular neutrino flavor after a defined distance.

To begin this chapter, Section 3.1 will provide an overview of the different types of neutrino oscillation experiments. Section 3.2 will then describe anomalies seen at short-baseline neutrino oscillation experiments and their implications.

3.1 Types of Neutrino Oscillation Experiments

The different types of neutrino oscillation experiments are discussed in this section, beginning with solar neutrino experiments in Section 3.1.1. Experiments with a focus on atmospheric neutrinos are then highlighted in Section 3.1.2, before reactor neutrino experiments are examined in Section 3.1.3. The section concludes with an introduction to accelerator neutrino experiments, providing an overview of both short and long-baseline designs.

3.1.1 Solar Neutrino Experiments

With a flux on the order of 10^{11} per square centimeter per second at Earth's surface, neutrinos emanating from the Sun make up the most abundant neutrino source available for neutrino oscillation experiments. Solar neutrinos are produced exclusively as electron neutrinos in nuclear fusion reactions, with the vast majority (99%) originating as by-products from the proton-proton (pp) chain. A small fraction (1%) of solar neutrinos are also hypothesized to originate from the Carbon-Nitrogen-Oxygen (CNO) cycle, which is theorized to be dominant for stars larger than the

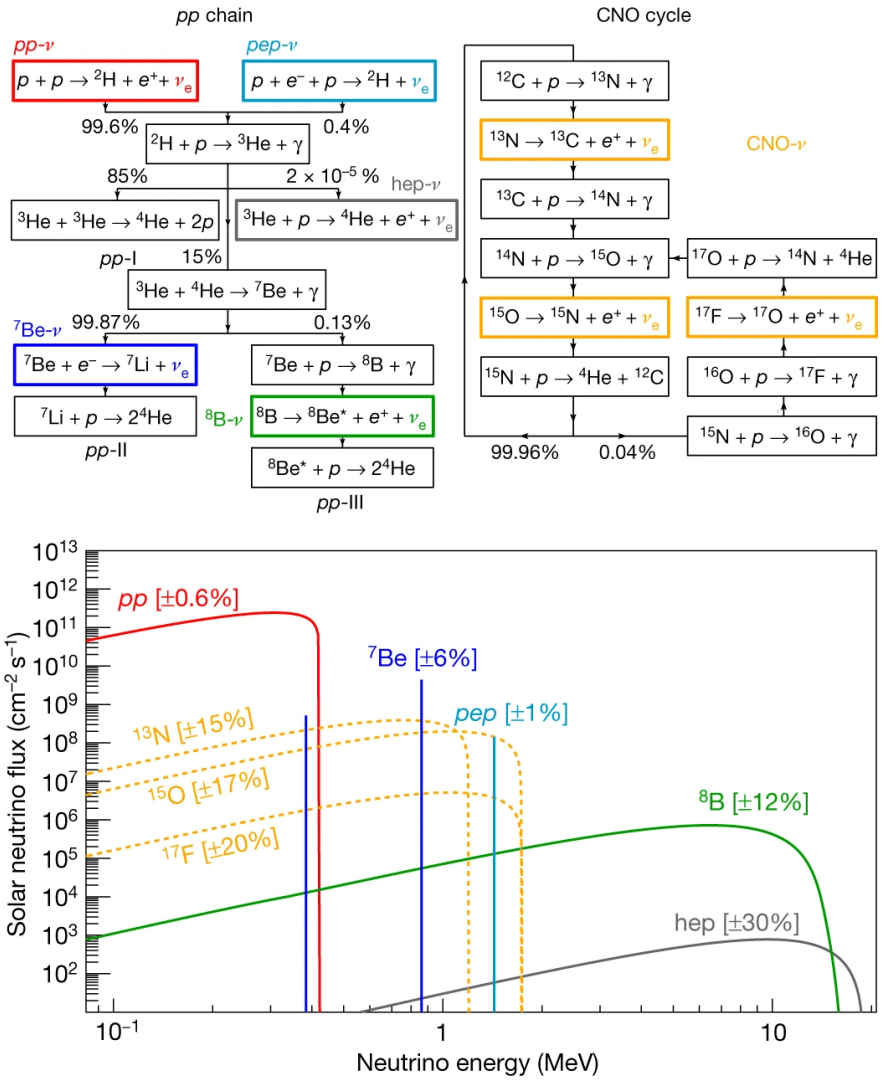

Figure 3.1: The pp and CNO cycles. The vertical scale is given in units of $\text{cm}^{-2}\text{s}^{-1}\text{MeV}^{-1}$ for continuum sources and in $\text{cm}^{-2}\text{s}^{-1}$ for monoenergetic sources [11].

Sun. The pp chain and CNO cycle are shown in Figure 3.1, along with their respective fluxes as a function of neutrino energy.

Solar neutrino experiments measure electron neutrino disappearance and have utilized a wide range of detector technologies to date. First generation experiments relied on radiochemical methods of detection, while modern detectors typically employ water Cherenkov or liquid scintillator technology given their real-time detection capabilities. Largely using data collected at Homestake, SAGE, GALLEX, Borexino, Super-K, and SNO, global fit analyses have been able to determine the oscillation parameters θ_{12} and Δm^2_{21}, often referred to as the "solar" mixing parameters.

With additional constraints from reactor experiments, these values are $\sin^2\theta_{12} = 0.308^{+0.012}_{-0.011}$ and $\Delta m^2_{21} = (7.49^{+0.19}_{-0.19}) \times 10^{-5}$ eV^2 [12].

3.1.2 Atmospheric Neutrino Experiments

Atmospheric neutrinos are a result of collisions between high-energy cosmic rays from outer space and atomic nuclei in Earth's atmosphere. In these collisions, cascades of secondary mesons are formed which primarily decay to muons and muon neutrinos. These muons also go on to decay, producing muon neutrinos, electrons, and electron neutrinos in the process. While far less abundant than solar neutrinos (flux of 1 cm^{-2} s^{-1}), the energy spectrum of atmospheric neutrinos is comparatively more varied and peaked toward higher energies. The measured energy spectra of atmospheric ν_μ and ν_e fluxes from various experiments are shown in Figure 3.2.

Experiments that measure atmospheric neutrinos are primarily sensitive to the disappearance of muon neutrinos and have provided measurements of θ_{23} and Δm_{31} - the "atmospheric" mixing parameters. Given that these neutrinos can travel anywhere from 15 km (cosmic-ray interaction height in atmosphere) to 13,000 km (approximate diameter of earth) before reaching a detector, these experiments often measure their zenith angle distributions as a proxy for neutrino oscillations. This is possible due to the neutrino's travel distance through Earth being a function of the zenith angle, and the neutrino oscillation probability ultimately being dependent on the ratio of this travel distance to the neutrino's energy (L/E in Equation 2.6). Global fits to data collected by the Super-Kamiokande and IceCube collaborations, both of which use Cherenkov light collected by photomultiplier tubes for neutrino signal detection, have provided values of $\sin^2(\theta_{23}) = 0.470^{+0.017}_{-0.013}$ and $\Delta m^2_{31} = 2.513^{+0.021}_{-0.019}$ eV^2 [12].

3.1.3 Reactor Neutrino Experiments

Nuclear reactors serve as a rich, human-generated source of electron antineutrinos where fragments produced in the fission of heavy isotopes undergo beta decay to reach stability. Specifically, the fission of ^{235}U, ^{238}U, ^{239}Pu, and ^{241}Pu isotopes is responsible for the vast majority of reactor antineutrinos, which are produced on the scale of 10^{20} $\bar{\nu}_e$/s per reactor. Because beta decays result

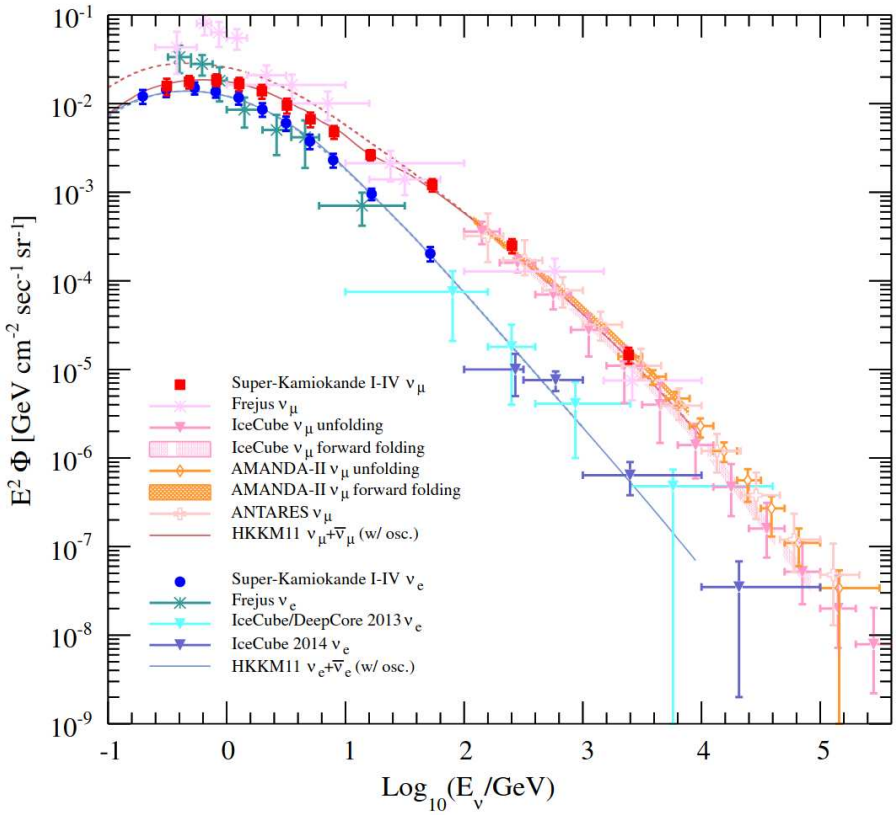

Figure 3.2: The measured energy spectra of the atmospheric ν_e and ν_μ fluxes [13].

in low-energy antineutrinos, the energy spectrum of reactor antineutrinos is peaked at low energies, with negligible contributions above 10 MeV.

Reactor neutrino experiments measure electron antineutrino disappearance, most commonly relying on inverse beta decay with a liquid scintillator target for detection. Depending on the baseline at which neutrinos are detected, these experiments are able to probe different oscillation parameters. Global fit analyses have provided the value of $\sin^2(\theta_{13}) = 0.02215^{+0.00056}_{-0.00058}$, which is primarily constrained by short-baseline (~1 km) reactor experiments like Double-CHOOZ, Daya Bay, and RENO [12]. On the other hand, the KamLAND experiment features a baseline of approximately 180 km and has used its $\bar{\nu}_e$ disappearance measurement to help constrain the solar oscillation parameters mentioned previously [14].

3.1.4 Accelerator Neutrino Experiments

Particle accelerators act as another human-generated source of neutrinos, and as the neutrino source of the SBN Program, will be the focus of the remainder of this chapter. The basic principle in accelerator-based neutrino experiments is to accelerate a beam of protons to nearly the speed of light before colliding the protons with a fixed target, producing mesons which ultimately decay to neutrinos. This process generally starts with the production of a hydrogen ion source which is accelerated linearly, stripped of its electrons, and further accelerated via synchrotron(s) to reach energies as high as $\mathcal{O}(100)$ GeV. Upon collision of the proton beam with the fixed target (usually beryllium or graphite), pions and other secondary particles are generated. It is the decay of these pions, as well as the secondary decay of muons, that leads to the creation of neutrinos and antineutrinos:

$$\pi^+(\pi^-) \rightarrow \mu^+(\mu^-) + \nu_\mu(\bar{\nu_\mu}) \tag{3.1}$$

$$\mu^+(\mu^-) \rightarrow e^+(e^-) + \bar{\nu_\mu}(\nu_\mu) + \nu_e(\bar{\nu_e}) \tag{3.2}$$

Other mesons are also produced in the collision of the proton beam with the target, though far less frequently than pions. Kaons, for example, contribute to intrinsic ν_e and $\bar{\nu}_e$ fluxes in the neutrino beams of the SBN Program, which will be discussed in more detail in Section 4.2.

Some experiments utilize beam stops that absorb negatively-charged pions while allowing positively-charged pions to decay at rest and produce low-energy muon neutrinos, muon antineutrinos, and electron neutrinos. It is more common, however, to produce neutrinos from pion decay-in-flight. This is achieved by first using a magnetic focusing horn with configurable polarity to focus the pions in one of two modes. Forward horn current (FHC) mode selects positively-charged pions, leading to a predominantly muon neutrino beam. Reverse horn current (RHC) mode selects negatively-charged pions, leading to a predominantly muon antineutrino beam. Regardless of horn current, the charged pions then enter an evacuated decay pipe with length designed to maximize the number of pion decays while simultaneously minimizing the number of muon decays. Finally,

a beam dump made of aluminum, steel, or concrete is used to absorb all non-neutrino particles. The end result is a well-collimated neutrino (or antineutrino) beam with energy up to tens of GeV, depending on the energy of the initial proton beam.

Accelerator-based neutrino experiments are often grouped into two categories: short-baseline (SBL) and long-baseline (LBL) experiments. Categorization depends on an experiment's baseline to energy ratio (L/E from Equation 2.6), which also determines the physics sensitivities for each category. SBL experiments have small L/E values ($\mathcal{O}(1)$ km/GeV), so Equation 2.6 suggests the oscillation probability is minimal for all but large values of Δm^2. On the other hand, LBL experiments have L/E values of $\mathcal{O}(100\text{-}1000)$ km/GeV, maximizing oscillation probabilities for the Standard Model neutrinos toward measurement of neutrino mixing parameters. Through both disappearance and appearance searches, the MINOS, T2K, and NOvA experiments have helped in constraining parameters in global fits and have shown good agreement with solar, atmospheric, and reactor experiments. Figure 3.3 shows regions of confidence for the parameters $\sin^2\theta_{23}$, $\sin^2\theta_{13}$, Δm^2_{32}, and Δm^2_{31} as determined with data from experiments in numerous neutrino oscillation sectors, and is highlighted by a clear refinement of the allowed parameter space with the inclusion of LBL accelerator neutrino data.

The next generation of LBL experiments, featuring DUNE and Hyper-K, will continue to constrain parameters while also determining the degree of CP-violation in the neutrino sector and the correct neutrino mass ordering. Figure 3.4 shows DUNE sensitivities to the determination of CP-violation and the neutrino mass ordering as a function of the true value of δ_{CP}. CP-violation can be observed with 5σ significance for 50% of δ_{CP} values after $\sim$10 years of run-time, while the neutrino mass ordering can be established with 5σ significance in just two to three years.

3.2 Short-Baseline Neutrino Anomalies

While long-baseline accelerator neutrino experiments have produced results consistent with solar, atmospheric, and reactor neutrino measurements, the same cannot be said for short-baseline accelerator neutrino experiments. As one example, consider the Liquid Scintillator Neutrino De-

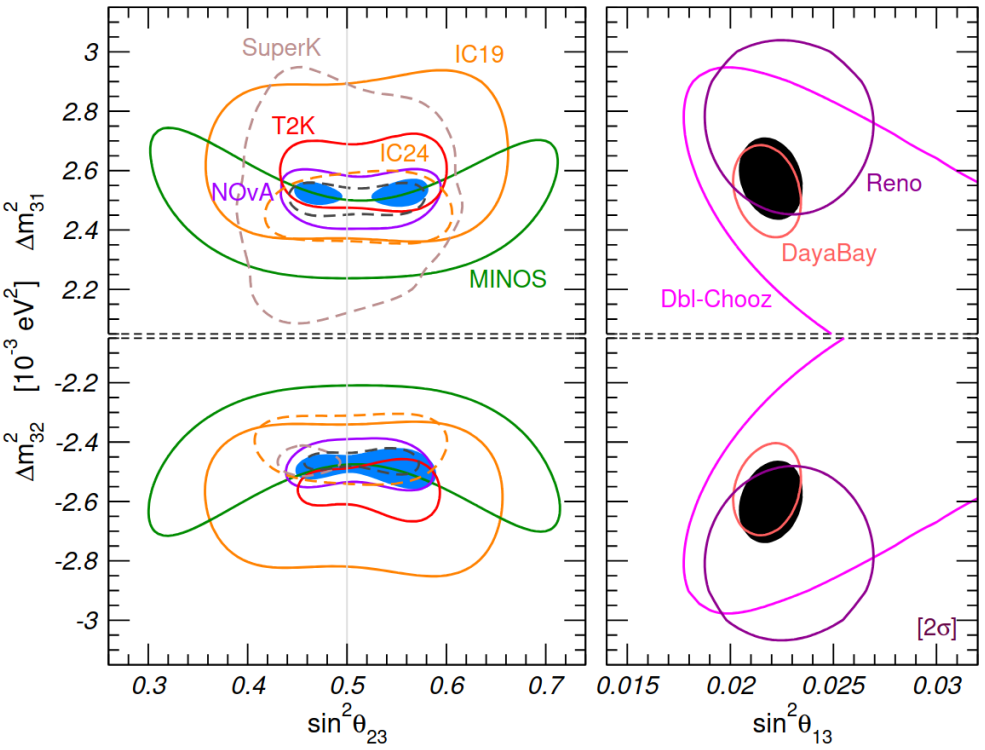

Figure 3.3: Confidence regions at the 95.45% confidence level in the plane of $\sin^2\theta_{23}$ and Δm^2_{32} (bottom left), $\sin^2\theta_{23}$ and Δm^2_{31} (upper left), $\sin^2\theta_{13}$ and Δm^2_{32} (bottom right), and $\sin^2\theta_{13}$ and Δm^2_{31} (upper right). In the left panel, the blue shaded region corresponds to the parameter space allowed by LBL accelerator experiments combined with data from IceCube's 2019 analysis, while the black dashed line corresponds to data from LBL accelerator experiments combined with data from IceCube's 2024 analysis and Super-Kamiokande [12].

tector (LSND). Operating from 1993 to 1998, LSND collected data from a muon antineutrino beam with ∼30 MeV average energy over a baseline of approximately 30 m. Having been sourced from pion decay-at-rest, the beam was extremely pure and contained only a small fraction of electron antineutrinos, allowing for a low-background oscillation search of $\bar{\nu}_\mu \to \bar{\nu}_e$ appearance. To identify electron antineutrinos, LSND utilized a tank of mineral oil doped with scintillating compound, relying on coincidence of Cherenkov light from the emitted positron and a delayed 2.2 MeV photon from neutron capture. Upon data analysis, the LSND collaboration observed an excess of electron antineutrino events over Standard Model backgrounds, corresponding to a 3.8σ deviation from expectation [16]. When viewed in the context of oscillations in the three-flavor paradigm, this excess

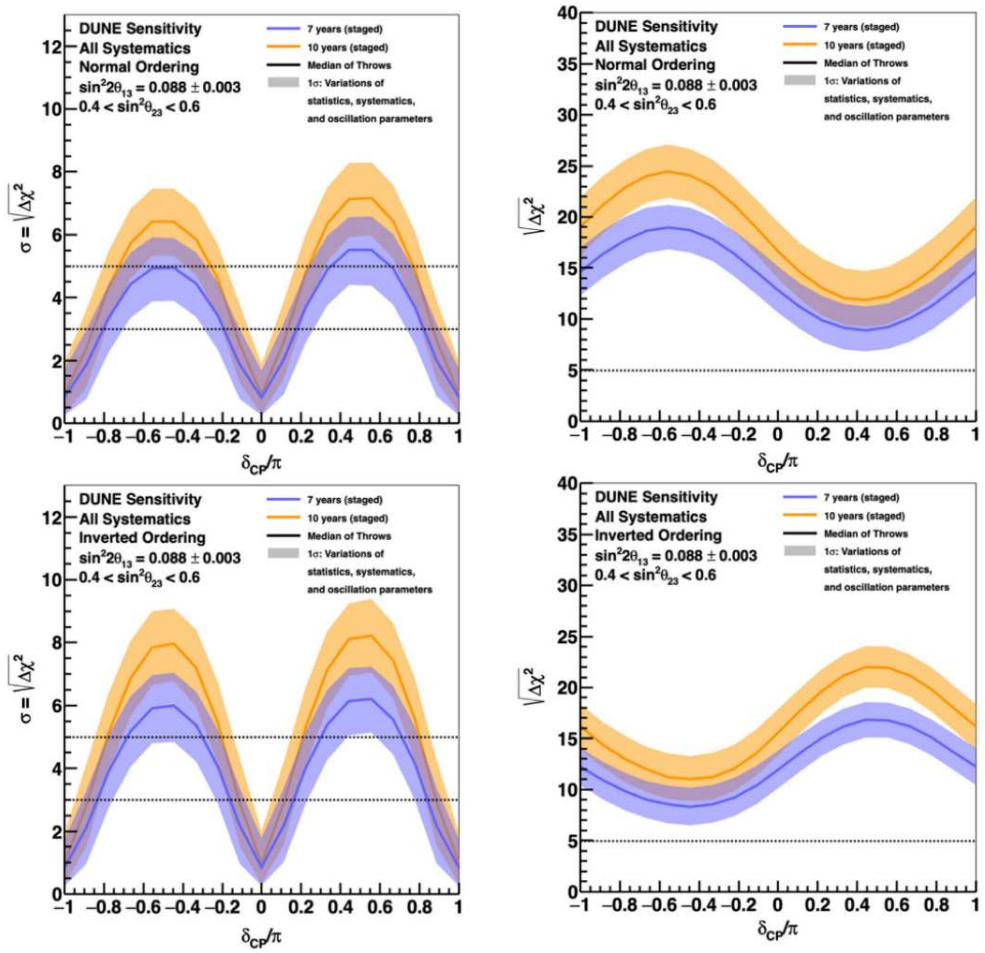

Figure 3.4: Significance of the DUNE determination of CP-violation (left) and the neutrino mass ordering (right) as a function of the true value of δ_{CP}, for seven (blue) and ten (orange) years of exposure, in both normal (top) and inverted (bottom) ordering [15].

implies a Δm^2 of $1.2\,\mathrm{eV}^2$, which is several orders of magnitude larger than the mass splittings measured in solar and atmospheric neutrino experiments.

As a follow-up to LSND, the Mini-Booster Neutrino Experiment (MiniBooNE) sought to measure neutrino oscillations over a similar L/E, but with a different experimental design than its predecessor. The MiniBooNE detector was located 541 m away from the Booster Neutrino Beam (BNB) target, where neutrinos and antineutrinos with average energy of $\sim$700 MeV were produced from pion decay-in-flight. Compared to LSND, the higher neutrino energies meant interactions at MiniBooNE would be dominated by CCQE scattering and the choice of decay-in-flight meant the experiment would be subject to a larger intrinsic ν_e background. MiniBooNE collected data from

2002 to 2019 and reported significant excesses of electron-like events in both neutrino and antineutrino operating modes. On their own, results from MiniBooNE correspond to a 4.7σ deviation from expectation, and when combined with results from LSND the significance increases to 6.0σ [17]. Reported excesses from each experiment are shown in Figure 3.5.

Anomalous results from LSND and MiniBooNE can be interpreted in a number of ways. The electron-like excesses could arise from various mechanisms under an oscillation hypothesis, the simplest of which involves the existence of a fourth, eV-scale neutrino in addition to those described in the Standard Model. However, given conclusive results from the Large Electron-Positron (LEP) collider that show only three neutrino flavor eigenstates couple to the Z boson [19], the fourth neutrino would not participate in weak interactions. This hypothetical neutrino has been dubbed the "sterile" neutrino, only interacting through the gravitational force and appearing in oscillations as $\nu_\mu \rightarrow \nu_{\text{sterile}} \rightarrow \nu_e$.

Alternatively, one could consider the possibility that the electron-like excesses are not the result of neutrino oscillations, but rather a misunderstood background. MiniBooNE in particular faced backgrounds from intrinsic ν_e contamination and misidentification of NC events, especially NC π^0s. While both of these backgrounds could be constrained with in-situ measurements, the latter is

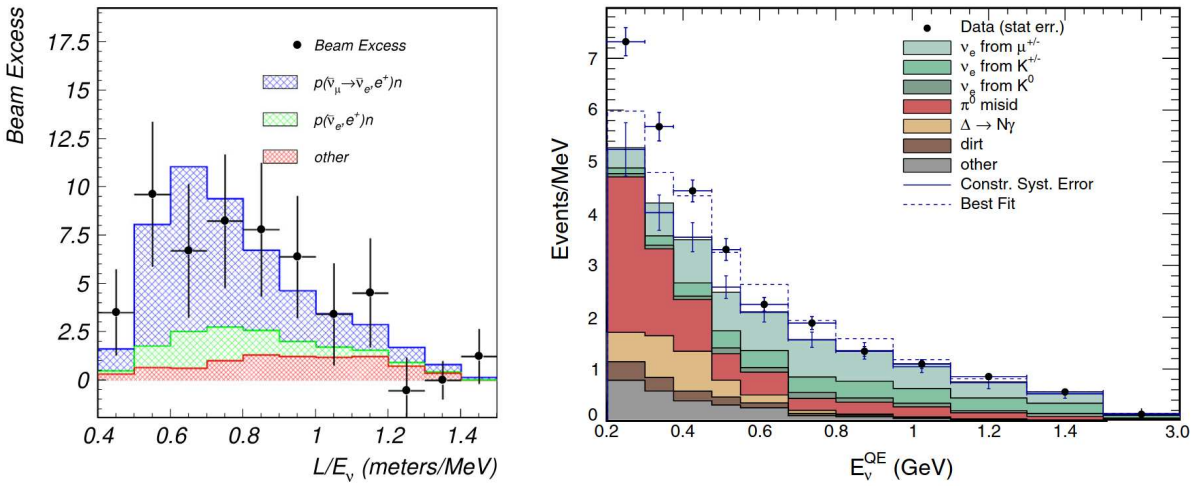

Figure 3.5: Distribution of observed events at LSND as a function of L/E [18] (left) and the MiniBooNE neutrino mode E_ν distribution for candidate quasielastic interactions [17] (right).

challenging due to limitations of Cherenkov light in identifying the neutrino interaction topology. Electrons and photons appear as indistinguishable rings on the walls of the detector, meaning the excess could be due to NC π^0s with overlapping or asymmetric pairs of photons. Similarly, events containing a single photon from radiative Δ decay could contribute to the excess. It is then clear that the ability to separate electrons and photons is key to resolving the short-baseline neutrino anomalies, motivating the detector technology choice for the SBN Program that is the subject of the next chapter.

Chapter 4

The Short-Baseline Neutrino Program

The Short-Baseline Neutrino Program, or SBN Program, is located at Fermi National Accelerator Laboratory and aims to resolve the anomalous neutrino oscillation results seen at LSND and MiniBooNE. Through use of multiple detectors located at different baselines in the same neutrino beam, the SBN Program specifically seeks to confirm or reject the existence of eV-scale sterile neutrinos. Additionally, and most relevant to the content of this thesis, the SBN Program features a rich cross section program that provides a means to characterize neutrino-argon interactions with high statistics.

This chapter will describe the SBN Program in detail, first providing a high-level overview before focusing on the technology relevant to the program. In Section 4.1, the goals and experimental configuration of the SBN Program are presented. Section 4.2 describes the neutrino beams relevant to the program. Lastly, Section 4.3 introduces liquid argon time projection chambers, which serve as the primary detector technology for experiments in the SBN Program.

4.1 Overview and Goals

The SBN Program consists of three LArTPC detectors located along the Booster Neutrino Beam (BNB) - a primarily muon neutrino beam with an average neutrino energy of $\sim$0.7 GeV. Nearest to the beam source is the 270-ton SBN near detector (SBND) at 110 m, followed by the 170-ton MicroBooNE detector at 470 m, and the 760-ton SBN far detector (ICARUS) at 600 m, as shown in Figure 4.1. In this configuration, simultaneous measurements of muon neutrino disappearance and electron neutrino appearance will enable the SBN Program to confirm or reject the existence of eV-scale sterile neutrinos. To facilitate this, the aforementioned baselines have been optimized to provide maximal sensitivity in the regions of oscillation phase space suggested to be relevant by LSND and MiniBooNE, as shown in Figure 4.2.

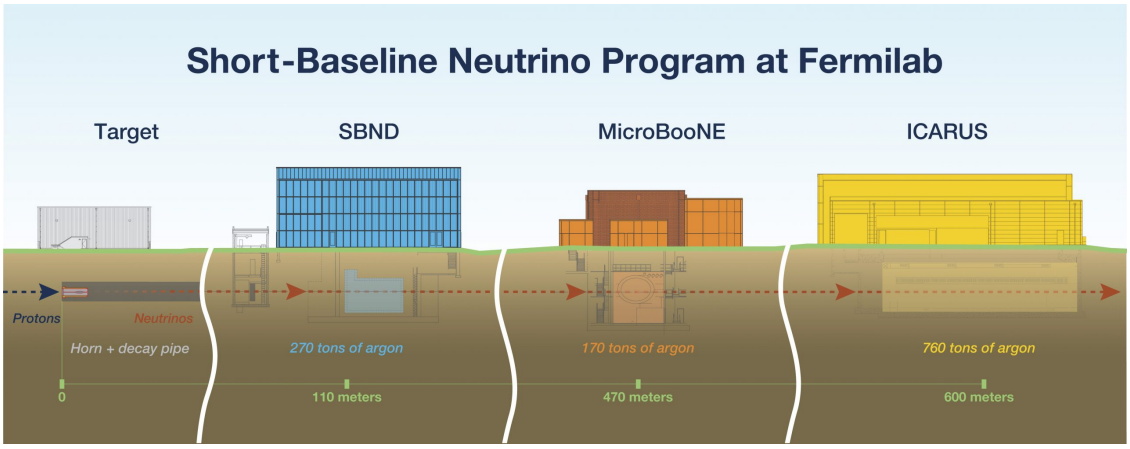

Figure 4.1: A schematic diagram of the SBN Program at Fermilab, showing SBND, MicroBooNE, and ICARUS from left to right. Image from Fermilab Visual Media Services.

Beyond oscillation physics, a plethora of neutrino cross section measurement opportunities exist within the SBN Program. Due to its close proximity to the BNB target, SBND will collect to the world's largest dataset of neutrino-argon interactions. By imaging $\sim$7000 neutrino interactions per day, SBND is primed to make high precision cross section measurements across both inclusive and exclusive channels. MicroBooNE and ICARUS report BNB cross section measurements as well, and are additionally positioned such that the detectors receive neutrinos from the off-axis Neutrinos from the Main Injector (NuMI) beam. Section 4.2 will report the flux of each beam in more detail. Measurements from all three detectors will contribute to building and constraining models for neutrino-nucleus interactions, which are among the leading source of systematic uncertainty for current and next generation oscillation experiments like NOvA [21], T2K [22], DUNE [23], and Hyper-K [24].

4.2 Neutrino Beams

The neutrino beams of the SBN Program are provided by the Fermilab accelerator complex, shown schematically in Figure 4.3. Beam creation begins with a 35 keV H^- ion source that is accelerated to 750 keV in a radio-frequency (RF) quadrupole, before further acceleration via a linear accelerator to 400 MeV. The H^- ions are subsequently stripped of their electrons before injection into the Booster, a 474 m circumference synchrotron operating at 15 Hz. Protons are accelerated to

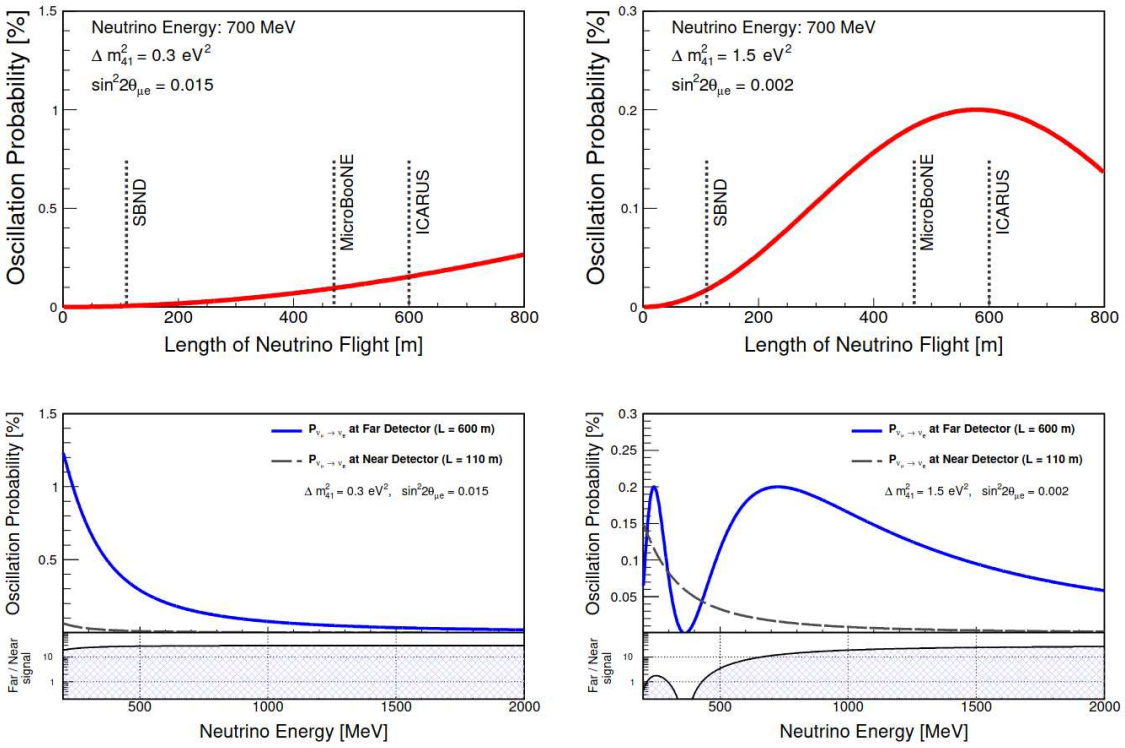

Figure 4.2: Neutrino oscillation probability for a 700 MeV neutrino as a function of baseline (top) and neutrino oscillation probability as a function of energy (bottom) for two sets of oscillation parameters [20].

8 GeV as they move through the RF cavities of the Booster, and are ultimately extracted in 1.6 µs long batches. Batches, which are further defined by their internal structure of 81 proton bunches with 2 ns width and 19 ns spacing, are then delivered to the BNB beam line for neutrino beam production or the Main Injector for further acceleration. In the latter case, six Booster batches are typically accelerated simultaneously in the Main Injector, given the synchrotron's 3.32 km circumference. These protons reach an energy of 120 GeV before delivery to the NuMI beamline.

4.2.1 Booster Neutrino Beam

Protons delivered to the BNB beamline are directed to a beryllium target, where collisions result in charged pions and other secondary particles as mentioned in Section 3.1.4. Charged secondary particles are then focused with a pulsed magnetic horn operating at 174 kA (−174 kA) before propagating through a 50 m long tunnel, where meson decays produce a predominantly neutrino (antineutrino) beam. The predicted neutrino flux for the neutrino operating mode (posi-

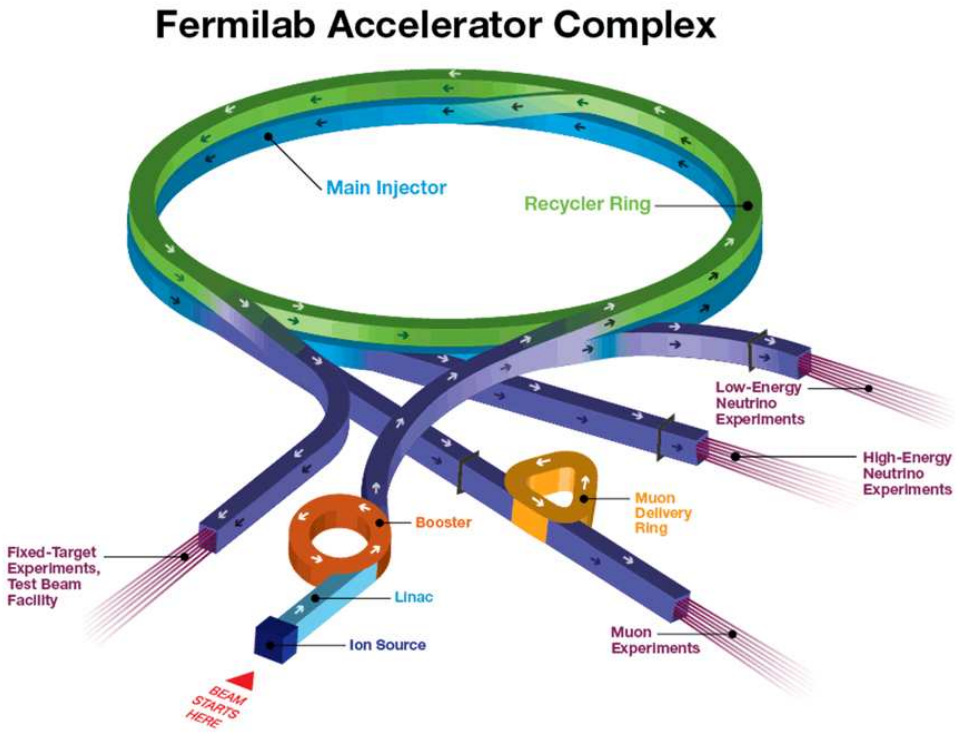

Figure 4.3: Schematic of the Fermilab accelerator complex, showing paths of protons used to create the BNB and NuMI beam are shown. Image from the Fermilab Accelerator Division.

tive horn current) is shown for each SBN detector in Figure 4.4. The flux is dominated by muon neutrinos ($\sim$93.6%), which arise primarily through pion decay in flight and have an average energy of 0.8 GeV. The remaining beam is comprised of muon antineutrinos ($\sim$5.9%) and electron neutrinos/antineutrinos at the sub-percent level. The prediction of neutrino beam flux is further discussed in the context of the ICARUS simulation in Section 6.1.1.

4.2.2 NuMI Beam

Protons delivered to the NuMI beamline are directed toward a graphite target, at which point secondary mesons from collisions are focused by a $\pm$200 kA two-horn system before entering a 675 m long decay tunnel. However, decays producing neutrinos that reach the off-axis SBN detectors (MicroBooNE at 8° and ICARUS at 6°) generally occur close to the beam target and before exiting the magnetic horn system. The effectiveness of horn focusing is reduced in these cases,

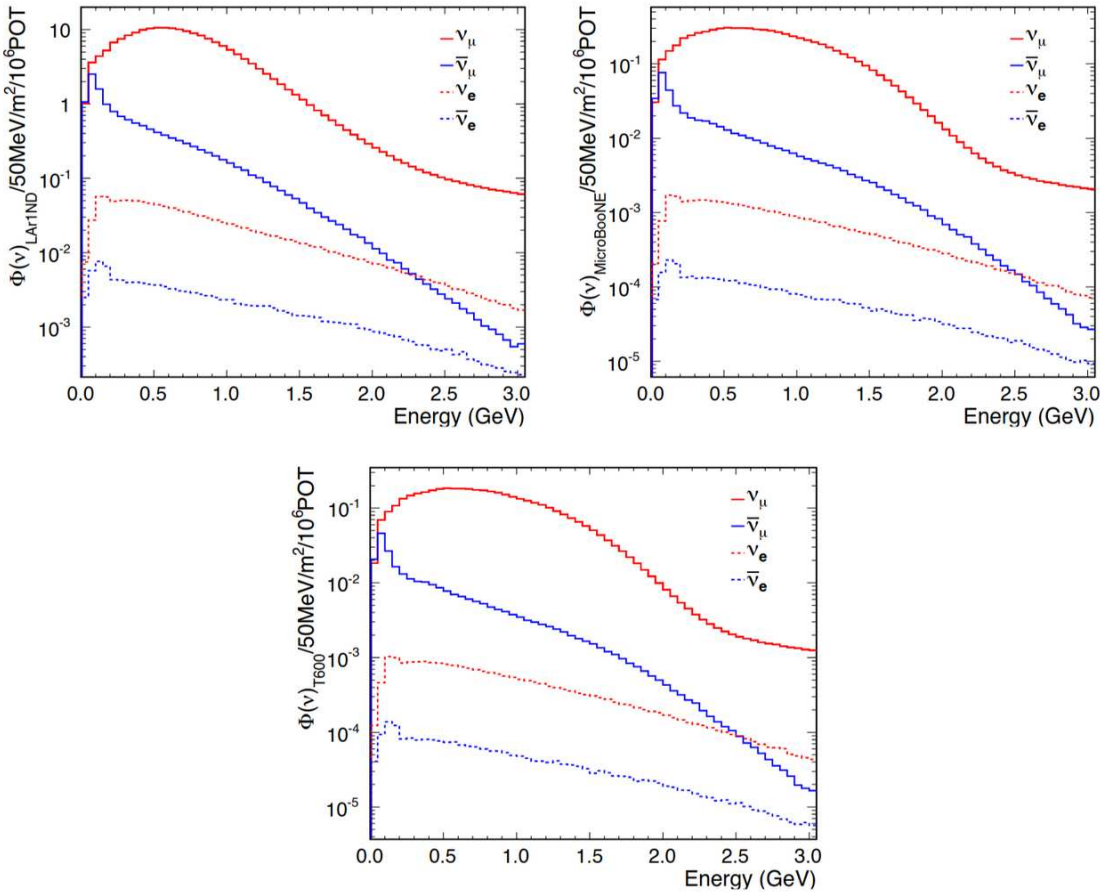

Figure 4.4: BNB flux prediction at the three SBN detectors: SBND (top left), MicroBooNE (top right), and ICARUS (bottom) [25].

resulting in smaller neutrino/antineutrino flux differences when compared to on-axis beams. The ν_μ:$\bar{\nu}_\mu$ and ν_e:$\bar{\nu}_e$ ratios from the simulated NuMI flux at ICARUS can be seen in Figure 4.5. These spectra also highlight the higher average energy of the NuMI beam ($E_\nu \sim 1.5\,\text{GeV}$) compared to the BNB, as well as enhanced electron neutrino and antineutrino components that arise primarily from three-body kaon decays.

4.3 LArTPC Technology

Detectors of the SBN Program are centered around fine-grained tracking calorimeters known as liquid argon time projection chambers (LArTPCs). Argon, which serves as both a neutrino interaction target and a detector medium, has a stable atomic configuration and therefore does not

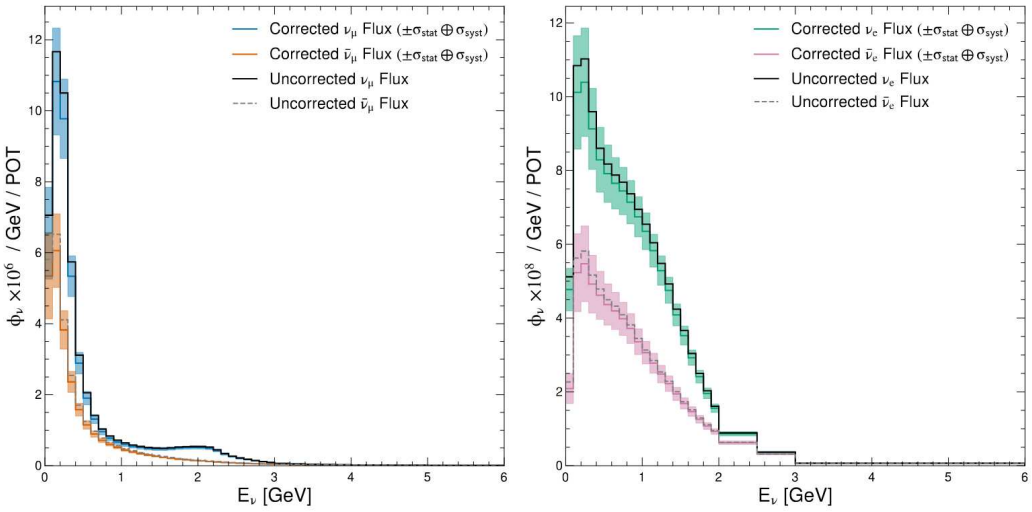

Figure 4.5: NuMI flux prediction for $\nu_\mu/\bar{\nu}_\mu$ (left) and for $\nu_e/\bar{\nu}_e$ (right) at ICARUS. The correction mentioned in the figure legend refers to a reweighting of simulated events based on measured hadron production cross section data [26].

contribute to the degradation of detector elements over time. Compared to other noble elements, argon is abundant in Earth's atmosphere and hence relatively cheap. Additionally, the high density of argon (1.393 g/cm^3) increases the probability of a neutrino interaction occurring within the detector. Furthermore, liquid argon is an attractive choice to the SBN Program due to its electron drift and scintillation light properties, which are discussed in the next section.

4.3.1 Operating Principles

When a neutrino interacts with an argon atom within a LArTPC, secondary particles may be produced that travel some distance within the detector. Charged particles with sufficient energy (the LAr work function is 23.6 eV) ionize argon atoms as they traverse the medium, while less energetic particles transfer their energy through atomic excitation. In the case of ionization, electrons are freed from argon atoms and subsequently subject to recombination with positively charged argon ions. When combined with a ground state argon atom, this process generates an excited dimer state. In the case of atomic excitation, an atomic electron is promoted to a higher-energy state and an excited dimer can be directly formed in the presence of a ground state argon atom. Regardless of production mechanism, the excited dimers eventually return to their ground states,

emitting 128 nm photons via radiative decay in the process. The decay time depends on the electron spin configuration of the dimer, with singlet states decaying in 6 ns and triplet states decaying in 1.6 µs. The emitted photons are collectively referred to as scintillation light, and their production is described in Equations 4.1 and 4.2.

$$\text{Ionization: } \mathrm{Ar}^{+} + \mathrm{Ar} + \mathrm{e}^{-} \rightarrow \mathrm{Ar}_2^{+} + \mathrm{e}^{-} \rightarrow \mathrm{Ar}_2^{*} \rightarrow \mathrm{Ar} + \mathrm{Ar} + \gamma \tag{4.1}$$

$$\text{Excitation: } \mathrm{Ar}^{*} + \mathrm{Ar} \rightarrow \mathrm{Ar}_2^{*} \rightarrow \mathrm{Ar} + \mathrm{Ar} + \gamma \tag{4.2}$$

The ionization electrons and scintillation photons discussed above make up the measurable signature of a neutrino interaction in a LArTPC. Through application of a strong ($\mathcal{O}(100)$ V/cm) electric field, ionization electrons are drifted toward an anode plane where detectable signals are induced. The electric field also serves to limit electron-ion recombination, as the rate of recombination decreases with increasing electric field strength. For a minimum ionizing particle (MIP) at 500 V/cm, the ionization signal yield is roughly 5000 e^{-} per millimeter of its trajectory, though some fraction of these are lost to electronegative impurities. Common impurities in argon include O_2 and H_2O, though these are typically minimized through use of a recirculating LAr filtration system. Scintillation photons are produced with a yield similar to ionization electrons and are collected by a photon detection system (PDS), typically comprised of photomultiplier tubes (PMTs) and/or silicon photomultipliers (SiPMs). Signals measured by the PDS provide the initial interaction time of the incident neutrino, and when coupled with knowledge of the ionization electron drift velocity in liquid argon, offer a means to determine the drift coordinate of neutrino interaction events in the LArTPC.

To create images of neutrino interactions, LArTPCs have traditionally relied on a series of wire planes that act as an anode for measuring ionization electron signals. For all SBN detectors, three wire planes are employed: two induction planes and an outer collection plane. On induction plane wires, bipolar signals are characterized by a positive peak as drift electrons approach the plane and a negative peak as they move past. Collection plane wires exhibit unipolar signals, given electrons

do not drift past these wires but are instead collected on them. Formation of these signals is illustrated in Figure 4.6, where induction planes are labeled U and V and the collection plane is labeled Y. Each wire plane is oriented at a different angle with respect to the others, meaning signals from a single plane provide a unique view of the interaction in two-dimensional wire-time space. Combining views from each plane then allows for three-dimensional spatial reconstruction of the interaction, which is further discussed in Section 6.3. Furthermore, integrating charge detected at the wire planes provides calorimetric information necessary to reconstruct the energies of the involved particles, and therefore the incident neutrino.

4.3.2 Shower Formation and Electron-Photon Separation

In the context of the SBN Program and its goal of resolving previous anomalous results from LSND and MiniBooNE, a critical function of the LArTPC is electron-photon separation. Electrons and positrons in liquid argon lose energy via ionization and bremsstrahlung radiation, with the lat-

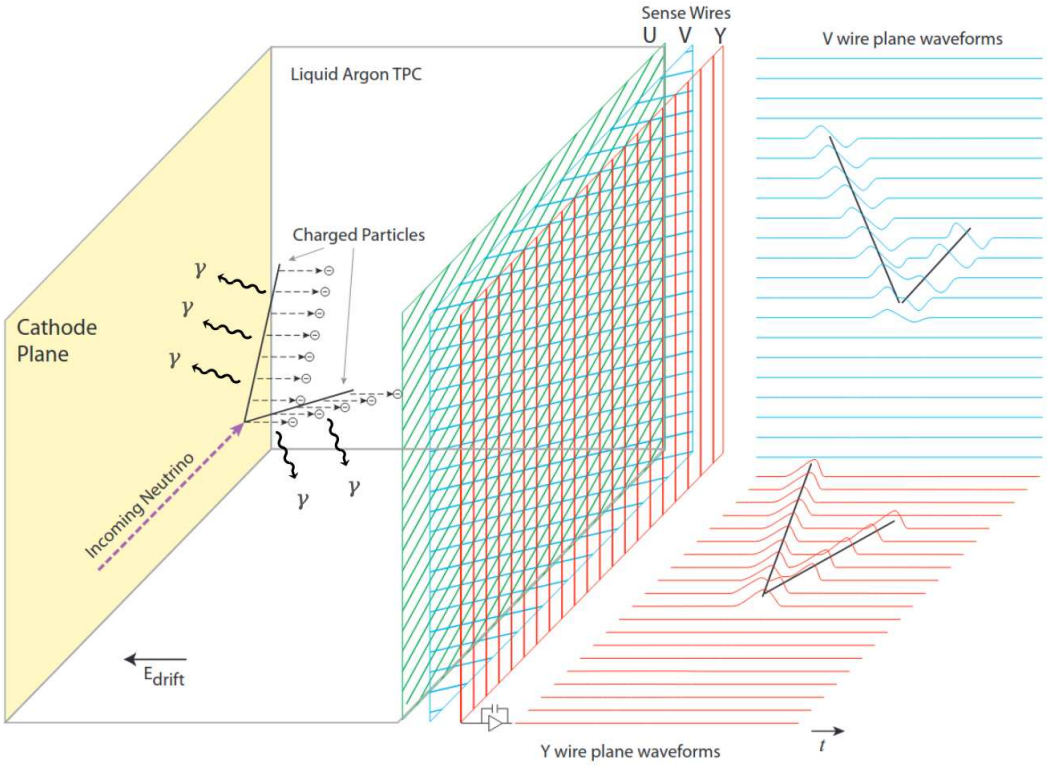

Figure 4.6: Illustration of signal formation within a LArTPC [27].

ter becoming the dominant process for those above a few tens of MeV, as shown in Figure 4.7a. Photons with energies beyond a few MeV lose energy predominantly via electron-positron pair production, while lower-energy photons are more likely to Compton scatter off of atomic electrons, as shown in Figure 4.7b. Within the SBN Program, electrons and photons from neutrino interactions are produced at the $\mathcal{O}(100)$ MeV energy scale and consequently induce electromagnetic cascades in which electrons and positrons produce photons via bremsstrahlung and photons produce electrons and positrons through pair production in a continuous cycle. The cycle continues until the involved particles no longer have the energy to radiate or pair produce, at which point the development of the electromagnetic cascade, or shower, ceases.

The longitudinal development of electromagnetic showers scales with the radiation length of argon, which is approximately 14 cm and defined as the average distance traversed for an electron to lose all but $1/e$ of its energy to bremsstrahlung radiation. The radiation length is related to the mean free path of photons by a factor of 7/9, meaning photons traverse $\sim$18 cm of the detector medium before leaving a trace of ionization, on average. This "gap" can be used as a distinguishing feature to separate photon showers from electron showers, as long as the detector can spatially

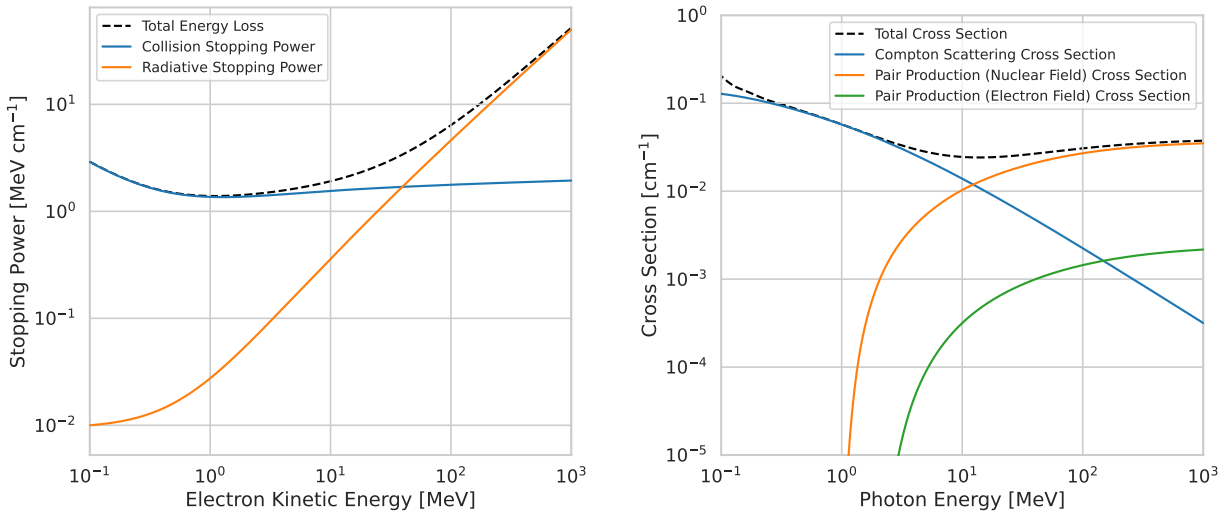

(a) **(b)**

Figure 4.7: (a) Electron energy loss in argon obtained from NIST ESTAR tables [28] and (b) photon cross sections in argon obtained from NIST XCOM tables [29].

resolve it. Given the anode plane wire spacing of SBN detectors ($\sim$3 mm), the drift speed of electrons in LAr ($\sim$1.55 mm/µs at 500 V/cm [30]), and the sampling rate of readout electronics involved (2-2.5 MHz), LArTPCs in the SBN Program are capable of $\mathcal{O}(1)$ millimeter-scale spatial resolution and can identify photons using their signature gap in the majority of cases.

For cases where the gap cannot be resolved, pair-producing photons can still be separated from electrons using calorimetric information. This is achieved by measuring the energy deposited per unit length at the track-like beginnings of electron and photon showers, typically referred to as the shower start dE/dx. Near the start of a photon shower, this quantity is double that of an electron shower given the presence of the electron-positron pair. An example of the electron-photon separation achievable through calorimetric means is shown for MicroBooNE data and simulation in Figure 4.8.

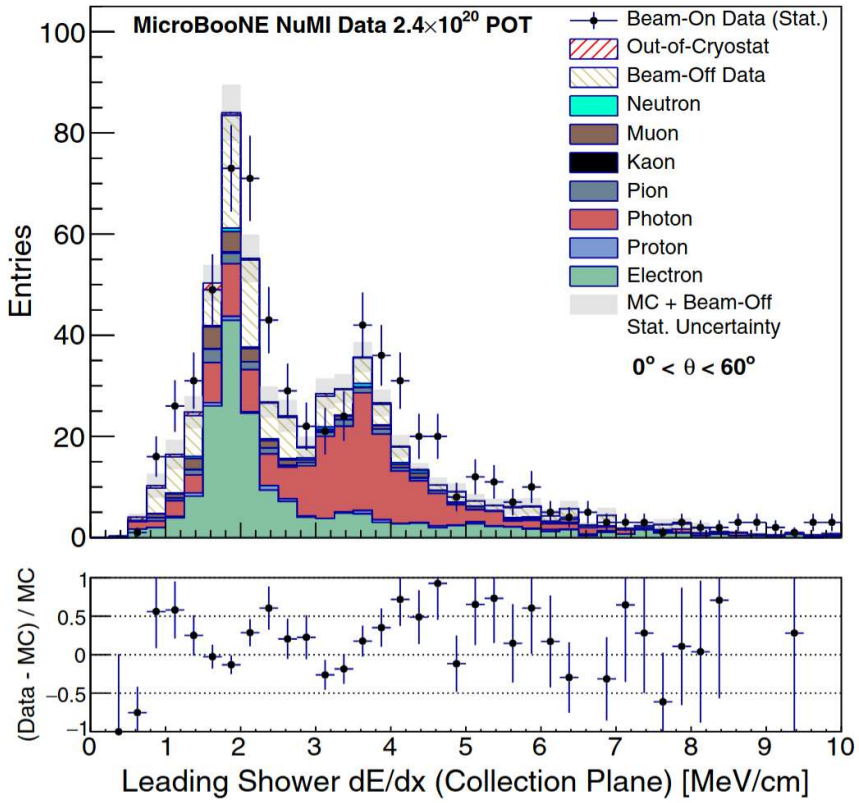

Figure 4.8: Shower start dE/dx measurements for neutrino candidates in the MicroBooNE detector [31]. Electron candidates are gathered in the peak near 2 MeV/cm, while photon candidates are near 4 MeV/cm.

Chapter 5

The ICARUS T600 Detector

Known formally as ICARUS T600, the ICARUS detector serves as the far detector for the SBN Program and is therefore key in measuring muon neutrino disappearance and electron neutrino appearance at the experiment. Beyond this, the ICARUS collaboration has long been associated with LArTPC research and development, with ICARUS T600 being the first large-scale detector to make use of the technology. This chapter will touch briefly on the history of ICARUS T600 followed by a discussion on the technical aspects of each detector subsystem.

5.1 History

Following the first proposal for the LArTPC in 1977 by Carlo Rubia, the ICARUS collaboration started an extensive R&D program in 1985 with the aim of operating a multi-kiloton LArTPC in the underground Laboratori Nazionali del Gran Sasso (LNGS). Though the multi-kiloton scale was never realized, the program culminated with the successful operation of the 760-ton ICARUS T600 detector, the largest of its kind at the time. Featuring two functionally-identical modules with internal dimensions of $3.6 \times 3.9 \times 19.6\,\mathrm{m}^3$, ICARUS T600 imaged cosmic ray muons in an initial technical run in 2001 and later collected neutrino data from the CERN Neutrino to Gran Sasso (CNGS) beam between 2010 and 2013.

By 2014, collaborators from SBND, MicroBooNE, and ICARUS had outlined the proposal for a short-baseline, three-detector neutrino oscillation program at Fermilab. In the same year, ICARUS T600 was moved to CERN, where it would undergo refurbishing before shipment to Fermilab. The refurbishing brought new cryostats, treatment of high-voltage cathodes for deformations, upgrades to the light collection system, and an overhaul of the TPC electronics - a necessity given the different operating conditions of LNGS (underground) and Fermilab (surface-level). ICARUS T600 was then shipped to Fermilab in 2017 before installation in the SBN Program's far detector building the following year (see Figure 5.1). Detector commissioning followed and would

Figure 5.1: Installation of ICARUS T600 at the SBN Program's far detector building. Photo from Reidar Hahn.

culminate with cryostat LAr filling and activation of all detector subsystems in 2020. Soon after, ICARUS T600 imaged its first cosmic-ray muons and BNB neutrinos at Fermilab, formally beginning its first period of physics data collection in 2021. More details on the timeline of ICARUS data collection are provided in Section 5.5.

5.2 TPC System

At the heart of the ICARUS detector are time projection chambers, which are contained in two cryostats housing 760 tons of liquid argon. Centrally installed in each cryostat is a high voltage cathode, with anode wire planes located approximately 1.5 m away on either side. The anode wire planes define the instrumented boundaries of the detector, containing 460 tons of active mass within their confines. By applying a voltage of −75 kV to each cathode and holding each anode at ground potential, four drift volumes, or TPCs, with electric field strength of 500 V/cm are created. Field uniformity, and therefore uniformity of electron drift velocity, is achieved in each TPC through a series of field shaping-electrodes with electric potentials linearly decreasing from the cathode.

TPCs are colloquially named according to their orientation with respect to the BNB direction, which runs approximately south to north. The westernmost (easternmost) cryostat is referred to as Cryostat West (East) and contains TPCs WW and WE (EW and EE). The ICARUS drift volumes are depicted schematically in Figure 5.2, while Figure 5.3a shows the key TPC components mentioned above.

In each TPC, the anode is comprised of three parallel wire planes at different orientations, as shown in Figure 5.3b. The plane nearest to the cathode is the first induction plane, containing 2112 horizontally oriented wires. The second induction plane and collection plane follow, each containing 5600 wires angled at $\pm 60^{\circ}$ from the horizontal. The distance between each of the wire planes, as well as the distance between wires in a given plane, is 3 mm. To extract ionization signals, groups of 64 wires are connected to warm external readout electronics via a series of feedthrough flanges. Specifically, each flange contains decoupling biasing boards (DBBs) that serve two important purposes: (1) application of bias voltage to wires and (2) signal transmission to front-end amplifiers. Distinct voltages of -250 V, -30 V, and 250 V are applied to the first

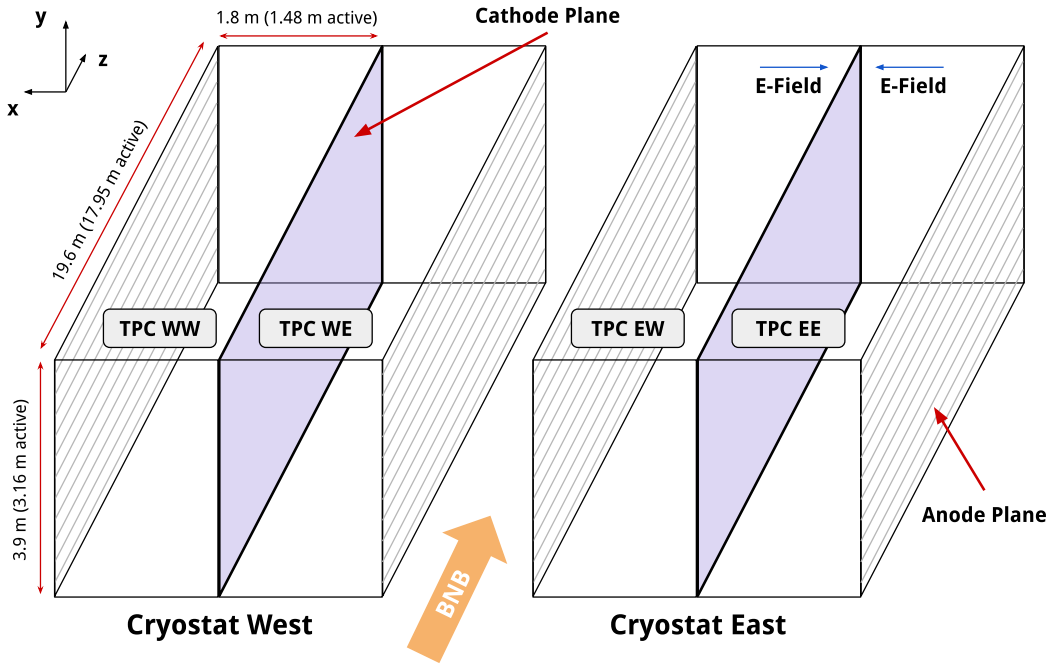

Figure 5.2: Schematic of the ICARUS T600 TPC system (not to scale). For simplicity, only a single wire plane is shown for each TPC.

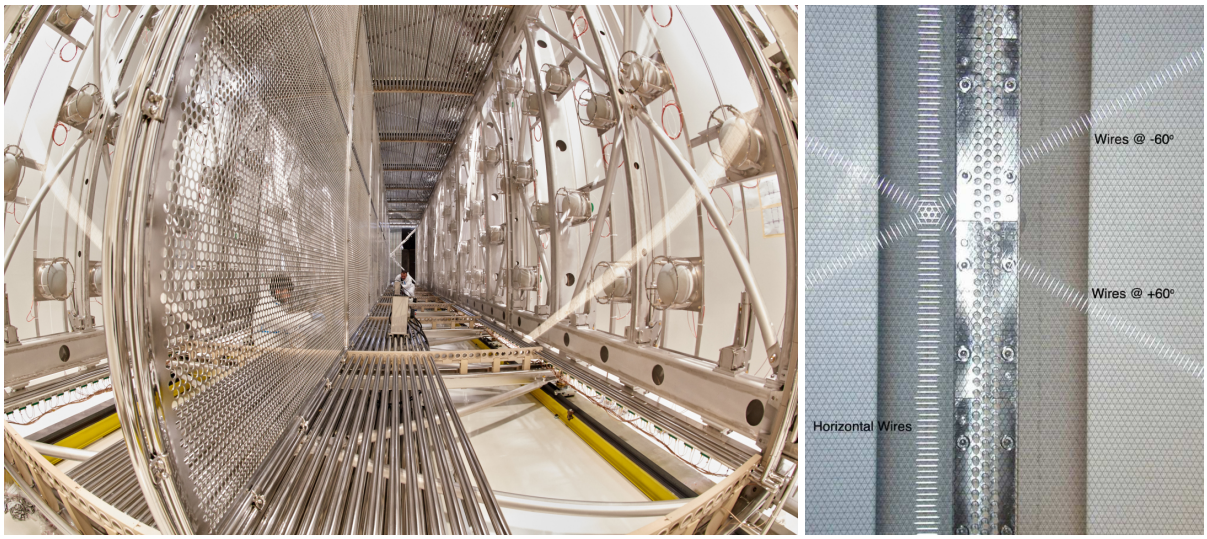

(a) **(b)**

Figure 5.3: Left: ICARUS T600 TPC during refurbishing at CERN, showing central cathode (vertical plane at left) and field cage electrodes (parallel to cathode at top/bottom). Right: ICARUS T600 TPC wire planes. Photos from the ICARUS collaboration.

induction, second induction, and collection plane respectively to ensure induction planes are transparent to passing ionization charge. The TPC wire readout electronics are shown in Figure 5.4. After signal amplification, a 12-bit analog-to-digital converter (ADC) is responsible for digitization, sampling TPC signals with 2.5 MHz frequency before interfacing with a field-programmable gate array (FPGA) for digital signal processing.

To ensure stable liquid argon temperature and purity, specially designed cryogenic systems are leveraged. ICARUS cryostats are double-walled such that liquid argon is isolated from external systems by a vacuum layer, keeping the temperature in each cryostat near 87.5 K. Further temperature management is achieved through circulation of liquid nitrogen around each cryostat and a surrounding layer of thermal insulation consisting of polyurethane foam. A purification system provides forced liquid argon recirculation, enabling ICARUS to maintain ultra-pure liquid argon with impurities less than 0.1 parts per billion O_2 equivalent. Liquid argon purity and its connection to detector calibration is further discussed in Section 7.1.

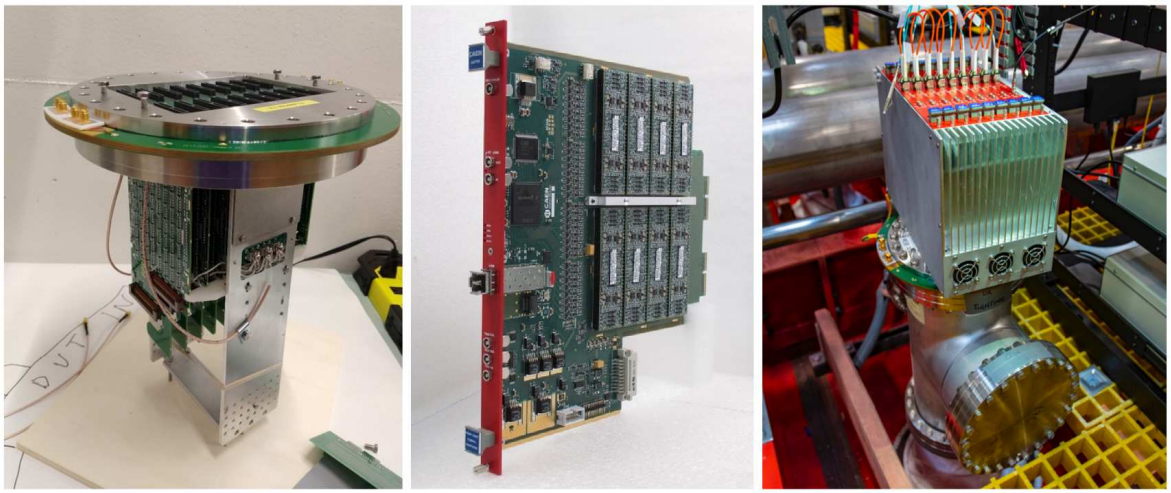

Figure 5.4: Left: An assembled feedthrough with DBBs installed. Middle: Front-end readout board housing amplifiers and ADCs. Right: Crate of nine front-end readout boards installed on top of a feedthrough flange. Photos from the ICARUS collaboration.

5.3 Photon Detection System

The ICARUS T600 photon detection system is comprised of a series of PMTs installed in each wire chamber and is responsible for the collection of scintillation light produced in neutrino and cosmic muon interactions with argon. Specifically, ninety 8-inch Hamamatsu PMTs are mounted approximately 5 mm behind the collection plane of each TPC, totaling to 360 PMTs for the entire detector. Each PMT surface is coated with tetra-phenyl butadiene (TPB) to shift photon wavelengths to the visible regime, given that the PMT glass is not transparent to 128-nm light. A photo of the ICARUS PMTs from one TPC is shown in Figure 5.5.

Each PMT is wired with high voltage and signal cables, which are routed to external electronics via separate feedthrough flanges. For signal digitization and waveform recording, 24 CAEN V1730B digitizers are employed, with each board containing a 14-bit ADC with 16 channels, 15 of which are used for PMT pulse acquisition. The remaining channel is used for the acquisition of ancillary signals, such as pulses from the ICARUS trigger system (see Section 5.5). In addition to readout electronics, each PMT is connected to a laser calibration system. Through use of optical fibers, light splitters, and an optical switch, PMTs are able to receive 60 ps pulses from a laser diode at 405 nm, allowing for studies of gain equalization and timing accuracy.

Figure 5.5: Mounted PMTs in an ICARUS TPC module. Photo from the ICARUS collaboration.

5.4 Overburden and Cosmic Ray Tagger

As a surface-level detector, ICARUS is exposed to a large flux of cosmic rays. The dominant component of this flux is cosmic muons, which are expected to pass through the active LAr volume at a rate of $\sim$17 kHz. This corresponds to approximately 17 cosmic-ray muons impinging upon the volume during the TPC drift window of $\sim$1 ms, making cosmic activity a significant background in the search for neutrinos at ICARUS. To mitigate this effect, a $\sim$3 m thick concrete overburden was installed in 2022 (see Figure 5.6a). Weighing five million pounds and consisting of three layers of concrete located above cryostats and all other detector components, the overburden reduces the cosmic muon flux by roughly 25% [32].

To identify residual cosmic activity, ICARUS utilizes a cosmic ray tagger (CRT) consisting of three subsystems: the top, bottom, and side CRTs. Each subsystem is fundamentally charac-

terized by two layers of plastic scintillating material for which coincidence logic can be applied to tag passing cosmic muons. The top CRT is divided into 123 modules, each of which contain two orthogonally oriented layers of eight scintillator strips. Covering a total surface area of 426 m^2, the top CRT alone is estimated to intercept nearly 80% of cosmic muons entering the ICARUS LArTPCs. The bottom CRT is located beneath the ICARUS cryostats, where fourteen refurbished modules from the Double Chooz experiment house 32 scintillating strips per layer in a parallel configuration. The side CRT utilizes repurposed modules from the decommissioned MINOS experiment. These modules form the internal and external layers of a series of eight walls surrounding the detector: one upstream, one downstream, and three per east and west side. Each module contains 20 scintillator strips and layers are oriented parallel to each other in all but the upstream wall. Part of the side CRT system can be seen in Figure 5.6b.

Light produced by cosmic muons passing through the ICARUS CRT modules is guided to photosensors by wavelength-shifting (WLS) fibers within each scintillator strip. Top CRT strips are instrumented with two WLS fibers, which are each connected to Hamamatsu SiPMs for light collection. In the bottom CRT, strips are equipped with one WLS fiber, and the 64 fibers from each module are individually connected to channels in a Hamamatsu PMT. Side CRT strips contain one

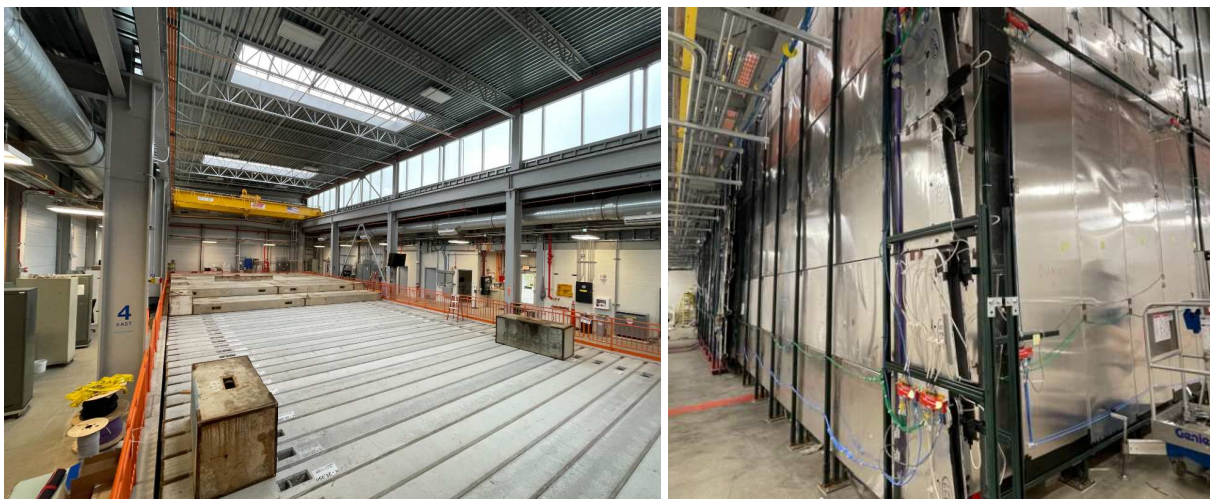

(a) **(b)**

Figure 5.6: Left: The ICARUS concrete overburden during installation. Right: The ICARUS side CRT. Photos from the ICARUS collaboration.

WLS fiber each, with optical readout handled by an array of ten Hamamatsu SiPMs (two fibers per SiPM). Given the SiPM-based light collection of the top and side CRTs, the subsystems share a common readout element in the form of the 32-channel CAEN DT5702 front-end board (FEB). Upon signal coincidence of SiPMs in each scintillator layer, the FEB issues a trigger for digitization of all channels. Custom FPGA-controlled FEBs are used to read out the bottom CRT and feature USB modules that are responsible for data processing and interfacing with data acquisition (DAQ) computers.

5.5 Trigger System and Data Collection

The ICARUS trigger system refers to the hardware implemented and logic applied in order to ensure detector subsystems efficiently collect data when desired. Two trigger logics with different functionality are employed by ICARUS: the "Majority" trigger and the "Minimum Bias" trigger. The Majority trigger, which is used in the collection of neutrino data, initiates detector readout upon coincidence of a sequence of PMTs with signals above a pre-defined threshold and a spill of the BNB or NuMI beam. By contrast, the Minimum Bias trigger initiates detector readout in the presence of a beam spill irrespective of the detection of scintillation light signals, and is typically used in studies of trigger efficiency.

In the implementation of the Majority trigger, ICARUS T600 modules are longitudinally segmented into three logical windows, each six meters in length and containing 60 PMTs (30 per TPC). The 6 m window length is motivated by the fact that at BNB and NuMI beam energies, neutrino interactions are generally contained to a small slice of the detector. Signals from adjacent PMTs within each window are paired and discriminated with a 13 photoelectron threshold, their coupled output forming a low-voltage differential signaling (LVDS) signal that is used in the trigger logic. If the LVDS signal multiplicity in at least one of the 6 m windows is above threshold, a signal known as the PMT trigger primitive is issued in the relevant module. The LVDS signal multiplicity threshold was chosen as five for ICARUS neutrino data collection, maximizing trigger efficiency while maintaining a sustainable data acquisition rate.

To determine temporal coincidence between PMT trigger primitives and neutrino beam gates (1.6 µs for BNB and 9.6 µs for NuMI), ICARUS relies on early warning signals from the Fermilab Accelerator Division. Arriving 35 and 730 ms before the arrival of protons to the BNB and NuMI targets, respectively, these signals mark the start of the beam spill gate. When a PMT trigger primitive occurs within the beam spill gate, a global trigger is issued, activating readout of detector subsystems. The TPC, PMT, and CRT systems are read out for 1.6 ms, 26 µs, and 6 ms around the trigger time, respectively, ensuring full coverage of charge and light signals associated with a neutrino interaction. A second "off-beam" gate is opened a fixed time after the beam spill gate and can be triggered upon in the same manner. Off-beam triggers provide a measurement of cosmic muons that are "in-time" with the neutrino beam through collection of an auxiliary dataset, which is necessary for background estimation in neutrino-based analyses. Figure 5.7 shows both on-beam and off-beam triggers for the BNB and NuMI beams, where the presence of neutrinos can be seen as an excess in on-beam triggers above off-beam triggers.

Upon the issuance of a global trigger, the ICARUS DAQ system is tasked with reading data from detector subsystems. The DAQ is based on the `artdaq` framework, a toolkit developed at Fermilab that offers data transfer and event-building capabilities [34]. Key `artdaq` software

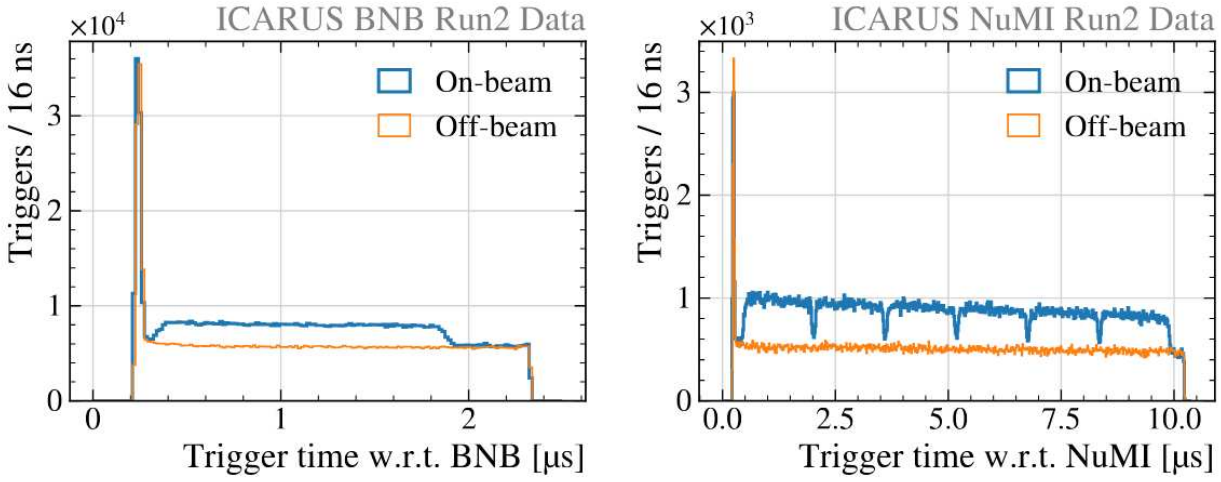

Figure 5.7: Profile of trigger time with respect to the beam gate time for the BNB (left) and NuMI (right) beams [33].

Table 5.1: Summary of ICARUS data collection runs. Neutrino beam exposure is reported in units of protons-on-target (POT). Forward horn current operating conditions are indicated by "FHC" and correspond to neutrino mode, while reverse horn current operating conditions are indicated by "RHC" and correspond to antineutrino mode.

	Run 1	Run 2	Run 3	Run 4
Start Date	June 2022	Dec. 2022	March 2024	Dec. 2024
End Date	July 2022	July 2023	July 2024	July 2025
BNB POT (FHC)	0.42×10^{20}	2.13×10^{20}	1.36×10^{20}	3.63×10^{20}
NuMI POT (FHC)	0.69×10^{20}	2.84×10^{20}	—	—
NuMI POT (RHC)	—	—	2.82×10^{20}	—

applications include "BoardReaders", which interface with detector subsystems and are responsible for packaging data into "fragments", and "EventBuilders" that aggregate data fragments into coherent events. For each global trigger, the BoardReader associated with the trigger system generates fragments containing information about the trigger type (Majority or Minimum Bias), gate type (on-beam or off-beam), and timestamps (trigger and gate). Trigger data fragments are then forwarded to EventBuilders, activating data requests from the TPC, PMT, and CRT BoardReaders. Data from each request forms the basis of an "Event" in the `art` event-processing framework, which is written to disk and serves as input to various downstream reconstruction paradigms.

ICARUS has collected neutrino beam data since 2021 and has featured four distinct collection periods, or runs, as of this writing. Table 5.1 summarizes the dates for each run, as well as the relevant neutrino beam exposure reported in units of protons-on-target (POT). As will be discussed in Chapter 8, the ν_μ CC π^0 analysis makes use of exclusively ICARUS Run 2 data.

Chapter 6

Simulation and Reconstruction

Comprehensive analyses at ICARUS require the ability to reconstruct neutrino and cosmic muon interactions that occur within the detector. This is not only necessary for measuring physics quantities with extracted data, but also for assessing backgrounds and systematic uncertainties with modeled interactions in simulation. This chapter will first outline the ICARUS simulation chain in Section 6.1 before discussing the reconstruction of interactions in simulation and data in Sections 6.2 and 6.3.

6.1 Simulation

At ICARUS, a dedicated Monte Carlo (MC) simulation chain allows for better interpretation of collected data and serves as a tool in evaluating various systematic effects. Based on the LArSoft software package [35], the ICARUS simulation chain is broken into several stages. The first stage involves the simulation of the neutrino beam flux, in which the number and flavor of neutrinos from the initial proton-beam target collision is predicted. Following this, the propagation of neutrinos to the detector geometry, as well as determination of whether or not a neutrino will interact with an argon atom, is handled. In the next stage, the particles produced in ν-Ar interactions are propagated through the detector volume and any secondary interactions are simulated. Finally, the detector response to ionizing particles is simulated, ultimately predicting the charge and light signals seen by various detector subsystems.

6.1.1 Beam Flux Simulation

Flux predictions for both neutrino beams offering exposure to ICARUS are based on the GEANT4 toolkit for simulating the passage of particles through matter [36]. Using a combination of theoretical and data-driven inputs, GEANT4 models initial proton interactions with the beam target as well as the propagation of secondary particles throughout materials in the beamline.

The BNB flux prediction is derived from the MiniBooNE flux simulation [37], while the NuMI flux prediction borrows from MINERvA [38] and NOvA [39] simulations. Both beam simulations are supplemented with existing hadron production data, with the BNB flux prediction being constrained with HARP data [40] and the NuMI flux prediction being tuned to NA49 [41] [42] and MIPP [43] data. The result of the beam flux stage of simulation yields the predicted flavor and energy composition of neutrinos that go on to be used as input to the next simulation stage, neutrino interaction modeling.

6.1.2 Simulation of Neutrino/Cosmic Interactions

Following the simulation of the neutrino beam flux, ν-Ar interactions are simulated. For this, ICARUS relies on the GENIE neutrino event generator [44], an open-source software suite used widely by the neutrino physics community. As a multipurpose tool, GENIE is tasked with propagating neutrinos to the detector geometry, establishing which neutrinos interact, determining neutrino interaction types, and generating final-state particles associated with interactions.

A factorized approach consisting of four steps is used to carry out these tasks. First, a nuclear model describes the initial state of nucleons involved in an interaction. At ICARUS, this is known as the Correlated Fermi Gas Model and is used to describe effects such as the Fermi motion of nucleons and Pauli suppression. Next, the primary neutrino-nucleon interaction is modeled according to cross sections of the various interaction processes, which form the total interaction cross section σ^{Total} when combined:

$$\sigma^{\text{Total}} = \sigma^{\text{QE}} + \sigma^{\text{MEC}} + \sigma^{\text{RES}} + \sigma^{\text{DIS}} + \sigma^{\text{Other}}. \tag{6.1}$$

In Equation 6.1, cross sections for quasielastic scattering, meson exchange current interactions, resonance production, and deep inelastic scattering are given by σ^{QE}, σ^{MEC}, σ^{RES}, σ^{DIS}, respectively. These interaction types were among those introduced previously in Section 2.2. The combined cross section for all other process not listed is given by σ^{Other}. While it is the total cross section that determines whether or not a neutrino will interact, the summed components

determine the type of interaction to occur through weighted random number generation. After an interaction type is determined, GENIE samples resultant particle kinematics from the relevant differential cross section model. A hadronization model then describes the production of neutrino-induced hadrons and a hadron transport model simulates the occurrence of final-state interactions as hadrons traverse the nucleus.

The ICARUS simulation chain uses GENIE v3.04.00 with a comprehensive model configuration named AR23_20i_00_000. Colloquially referred to as the SBN tune, the various models employed in this configuration are listed in Table 6.1. Of particular interest is resonance modeling, as this yields the predicted number of neutral pions produced directly in ν-Ar interctions. This interaction mode has historically been described by the Rein-Sehgal model [45], which applies the Feynman–Kislinger–Ravndal model of a relativistic quark harmonic oscillator [46] to neutrino-induced baryon resonances. An improvement upon this model which considers mass effects of the lepton is used in the SBN tune and is referred to as the Berger-Sehgal model [47]. Neutral pions can also be produced or absorbed in final-state interactions within the nucleus, which is governed by the INTRANUKE/hA model of hadron transport [48].

Table 6.1: Summary of the GENIE interaction model at ICARUS.

Interaction/Process	Model
Nuclear	Correlated Local Fermi Gas
Quasielastic Scattering	Valencia
2p2h	SuSAv2
Resonance	Berger-Sehgal
Coherent Pion Production	Berger-Sehgal
Deep Inelastic Scattering	Bodek-Yang
Hadronization	AGKY
Final State Interactions	INTRANUKE hA

In addition to neutrino events, it is critical to simulate the cosmogenic background at ICARUS. This is done with CORSIKA [49], a software program that simulates air showers initiated by high-energy cosmic-ray particles. The CORSIKA configuration used by ICARUS simulates a proton-only cosmic flux impinging on Earth's atmosphere, an assumption that has shown good agreement with cosmic data collected at the SBN Program. Use of a pre-generated CORSIKA database allows for the retrieval of secondary particle kinematics that would be seen at ICARUS, which are then simulated as starting from a plane twenty meters above the detector. At this point, the generated neutrinos and cosmic secondaries are ready to be propagated through the detector, which is discussed in the next section.

6.1.3 Detector Simulation

The next stage of simulation involves the propagation of particles, whether of neutrino or cosmic origin, through the various ICARUS detector components. Like the beam flux simulation, this stage relies on GEANT4 to produce trajectories for primary particles and the secondary particles that result from their interactions and decays. GEANT4 propagates particles in discrete "steps" that are defined by relevant physics processes and the simulated detector geometry until the particle decays, falls below a tracking threshold, or exits the detector. At each step, GEANT4 calculates the energy deposited by the particle, as well as the number of electrons and photons produced via ionization and scintillation, respectively. Energy depositions for a simulated ν_μ CC π^0 interaction at ICARUS are visualized in Figure 6.1.

Ionization electrons within each TPC volume are drifted toward the wire readout planes, a process through which they are subject to charge quenching from electron-ion recombination and absorption by electronegative impurities. It should be noted that first ICARUS analyses, including the one presented in this thesis, use the modified Box model [50] of recombination in simulation. Recombination effects in data, however, are corrected with the ellipsoid modified Box model (EMB) [51] that accounts for the track angle dependence of electron-ion recombination, result-

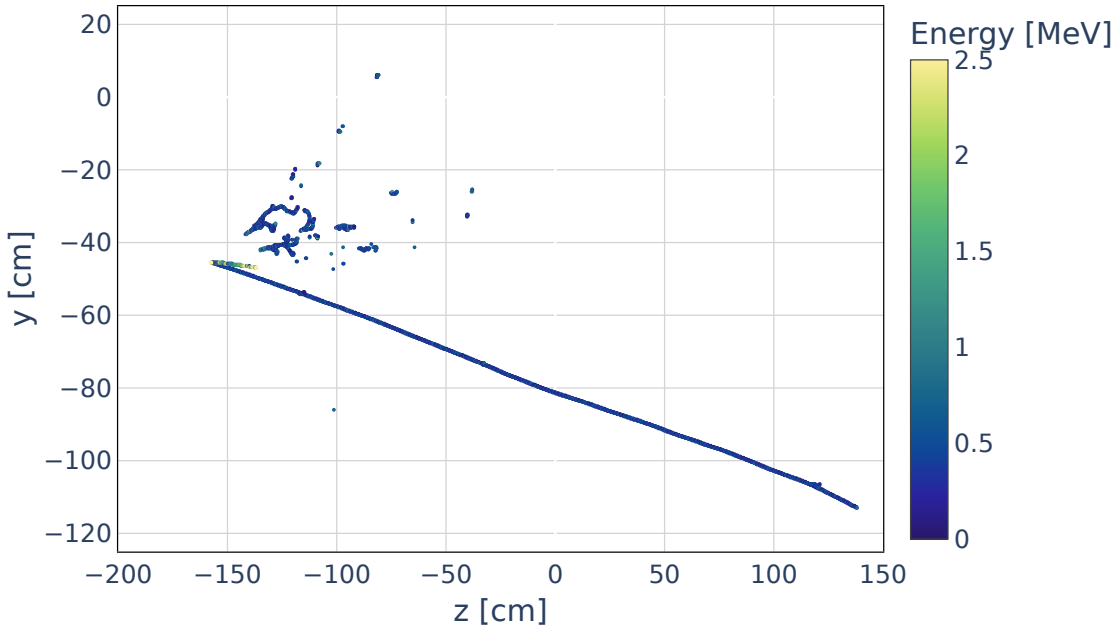

Figure 6.1: A simulated ν_μ CC π^0 interaction in the ICARUS detector, with deposited energy as calculated by GEANT4 represented by the color scale. The neutrino is incident from the left side of the image.

ing in improved particle identification accuracy. The difference in treatment between data and simulation is treated as a systematic uncertainty and is further discussed in Section 9.3.

Effects that modify the position of the drifting electron cloud are also simulated and include electric field distortions from space charge effects and diffusion, both of which are discussed in Chapter 7. While individual scintillation photons are not directly simulated, Rayleigh scattering and photon absorption processes are taken into account through a "photon library", a look-up table exploiting previously-computed likelihoods for photon propagation at any point in the detector.

To enable meaningful comparisons between simulation and collected ICARUS data, the signals observed at detector readout elements as a result of ionization electrons or scintillation photons must be simulated. The measured ionization signal on a given TPC anode wire is modeled as a convolution of the arriving electron distribution and a detector response function. While this model accounts for signal contributions from ionization electrons drifting in nearby wire regions ("2D convolution") [27] [52], a simplified approach in which these contributions are ignored ("1D convolution") is described here. Taking the measured ionization signal as $M(t')$, the convolution

of the original charge signal $S(t)$ and the detector response function $R(t, t')$ can be written as:

$$M(t') = \int_{-\infty}^{\infty} R(t, t') \cdot S(t), \tag{6.2}$$

where t is the signal arrival time and t' is the measurement time. The detector response function encompasses both the field response, which describes the current induced on a wire due to a single electron, and the electronics response, which describes the impact of shaping and amplification from readout electronics on the induced current. ICARUS uses the GARFIELD simulation program [53] to calculate field response functions, while a Bessel shaping function is used for modeling the electronics response. Field response functions are tuned through comparisons with waveforms from cosmic muon data, and resultant simulated signal waveforms are summed with simulated noise waveforms (which are also tuned with ICARUS data) to produce the ionization component of this stage's output [54].

As previously mentioned, the number of scintillation photons reaching the ICARUS PMTs is determined from the photon library. This quantity is then converted to a number of photoelectrons by considering the PMT quantum efficiency, accounting for factors such as the likelihood of TPB wavelength shifting occurring and the probability of photon conversion at the photocathode. Each photoelectron is represented by a single photoelectron response (SPR) function and the sum of all SPRs for a given PMT channel in combination with a simulated noise component yields the simulated optical waveform. The software emulation of the ICARUS trigger system can then use these waveforms to determine whether or not to keep an event in the simulated output, in accordance to the desired trigger logic of the simulation. Additionally, the CRT subsystem's response to energy deposited in scintillator strips is simulated. This includes the formation of the SiPM analog signal as well as the subsequent gain application and timestamp generation of CRT hits.

6.2 Low-Level Reconstruction

Neutrino event reconstruction refers to the process of building descriptive portraits of ν-Ar interactions from the signals produced in each detector subsystem, whether real or simulated. The successful reconstruction of a neutrino event should yield information pertaining to the type of interaction, the identification of secondary particles, and the energy of the incident neutrino. While ICARUS has developed multiple reconstruction algorithms to produce these final deliverables, they often share common inputs in the form of low-level quantities produced early in the reconstruction process, which are discussed in this section.

6.2.1 TPC Reconstruction

Event reconstruction within each ICARUS TPC begins with the processing of digitized wire readout waveforms. Waveforms first have their coherent noise component removed, at which point they are subject to a deconvolution procedure which aims to extract the original ionization signal. By applying a Fourier transformation to Equation 6.2, one obtains $M(\omega) = R(\omega) \cdot S(\omega)$, the measured signal in the frequency domain (ω has units of angular frequency). Rearranging this equation yields the original signal in the frequency domain, though an additional filter function, $F(\omega)$, is needed to attenuate high-frequency electronics noise that is amplified by the deconvolution procedure [27] [52]:

$$S(\omega) = \frac{M(\omega)}{R(\omega)} \cdot F(\omega). \tag{6.3}$$

The original signal in the time domain, $S(t)$, can then be found by applying the inverse Fourier transform to Equation 6.3. This signal, now in the form of unipolar charge distributions for each TPC wire plane, is the final output of the deconvolution. At the time of this writing, the Fourier transform employed by ICARUS for translating between the time and frequency domains assumes the induced signal on a wire to be independent of charge drifting past adjacent wires. This is referred to as a "1D deconvolution", though a more accurate method that considers both the time and wire dimensions ("2D deconvolution") will be used in future analyses.

To identify waveform regions that are likely to contain an ionization signal, deconvolved waveforms are subject to an algorithm that seeks to locate regions-of-interest, or ROIs [55]. Waveforms from a given anode wire plane are first used to form a 2D image in wire-time space, allowing for the use of morphological filters to enhance candidate signal regions in magnitude and extent. A predefined threshold is then applied to the image in order to identify ROIs that can ultimately be mapped back to the individual deconvolved waveforms. This procedure not only reduces the volume of collected data, but also increases the speed of downstream reconstruction algorithms.

A multi-Gaussian fit is performed on pulses in each ROI, and pulses with fit amplitudes above a predefined threshold (distinct from the ROI-finding threshold) are deemed to be "hits". Hits represent localized charge depositions in the detector and are defined by their total charge (Gaussian area), peak time (Gaussian mean), and width (Gaussian root mean square). As hits are meant to be consumed by later stages of reconstruction, the ICARUS hit-finding algorithm is well-optimized and highly efficient. However, success in identifying a signal ultimately depends on multiple factors, including TPC noise levels and particle trajectory angles with respect to the wire plane of interest. Further, the use of a threshold to define hits introduces an inherent loss of ionization signal for low-energy depositions. This is most relevant for electromagnetic showers and is accounted for in downstream calorimetric corrections, as discussed in Section 6.3.3.

6.2.2 PMT and CRT Reconstruction

Reconstruction of scintillation light at ICARUS is achieved through PMT waveform processing. Similar to TPC hit-finding, a threshold-based algorithm first identifies signals that are referred to as optical hits. Optical hits from one or more PMTs in temporal coincidence are then grouped to form what is referred to as an optical flash. The integral of all optical hits within one microsecond of the leading signal edge yields the total detected light for the optical flash, which is later associated with a single neutrino or cosmic-ray interaction within the TPC.

CRT reconstruction broadly refers to the process of converting raw data from CRT FEBs, which includes timestamps and digitized counts from every SiPM, to a format suitable for later analysis

stages. This involves the creation of data products known as CRT hits, defined by coincidences between adjacent CRT modules. For the top CRT, a hit is provided by a quadruple coincidence (four SiPMs from each module layer), while side CRT hits are found at the software level. When combined with PMT information, the CRT can be used as a powerful tool to reject cosmic-ray muons based on the time-of-flight between the two subsystems. A neutrino-induced muon exiting the LArTPC would be associated with a CRT hit produced at a later time than the optical flash, while the situation would be reversed for a cosmic-ray muon.

6.3 High-Level Reconstruction

Building from the low-level objects described in the previous section, the goal of high-level event reconstruction is to fully characterize neutrino interactions while simultaneously rejecting unwanted backgrounds like cosmic-ray muons. At ICARUS, two fully-automated high-level reconstruction frameworks exist: Pandora [56], which uses a multi-algorithm approach to LArTPC pattern recognition, and SPINE [57], a machine-learning based reconstruction chain. The ν_μ CC π^0 analysis in this thesis was carried out with SPINE, and a greater emphasis will therefore be placed on the SPINE framework in this section. However, given that Pandora was established at an earlier time than SPINE, it was the chosen high-level reconstruction framework for many calibration studies at ICARUS and will also be discussed in this section.

6.3.1 Pandora

Though originally designed with linear collider experiments in mind, the Pandora event reconstruction framework is well-established at many LArTPC experiments today. At ICARUS, over one hundred Pandora algorithms are used to build features of neutrino interactions starting from the 2D hits that serve as input. These algorithms are spread across two passes of reconstruction: (1) an initial pass optimized for cosmic-ray muons, and (2) a subsequent pass optimized for neutrino interactions. An outline of each Pandora event reconstruction pass is shown in Figure 6.2.

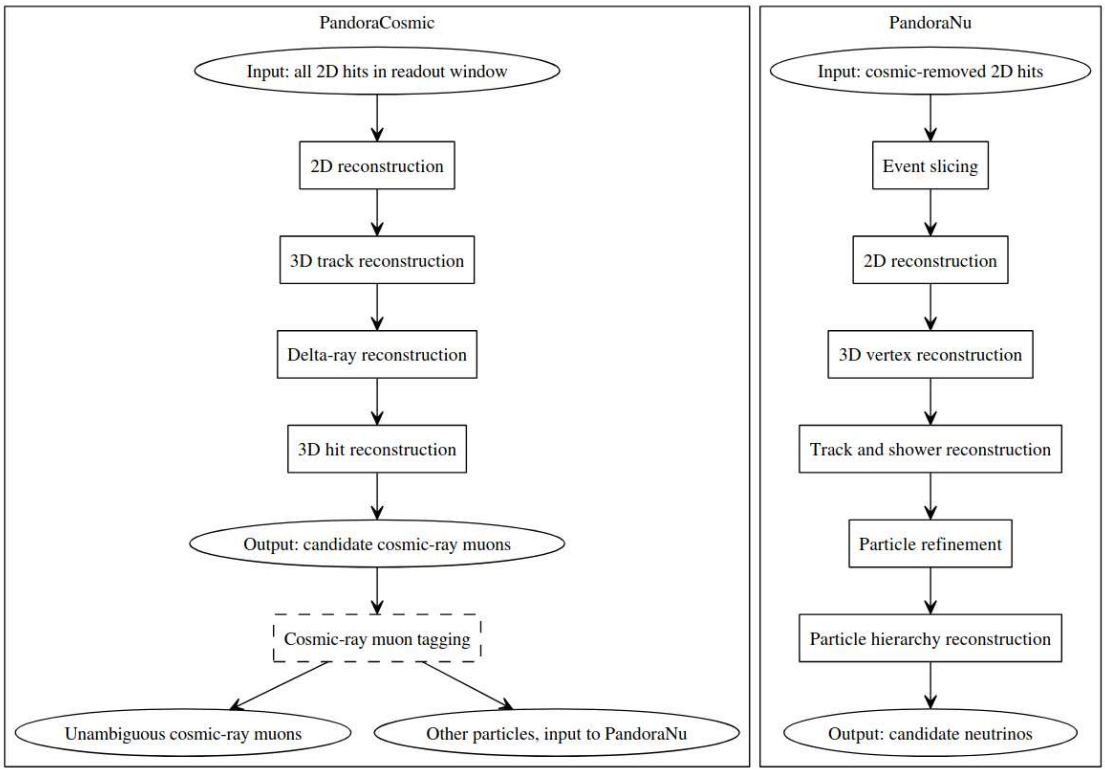

Figure 6.2: Diagram highlighting the two passes of Pandora event reconstruction used at ICARUS [56].

Known as *PandoraCosmic*, the beginning phase of Pandora reconstruction aims to reconstruct cosmic-ray muon trajectories in the ICARUS TPCs. To accomplish this, hits are first grouped into 2D clusters for each wire readout plane. These clusters are then matched across the three planes by considering the drift coordinate overlap between clusters and the wire plane geometry, resulting in a track-like object that contains clusters from multiple wire planes. If possible, the 3D position of each hit (or "space point") is determined by performing sliding linear fits to the clusters from other planes at the same drift coordinate. Additionally, the particle start (end) point is identified as the space point with the highest (lowest) vertical position. The output of PandoraCosmic is a candidate cosmic-ray muon, which is then passed to an external module for final classification. If the candidate is throughgoing, meaning the reconstructed trajectory passes through two faces of the detector other than the upstream and downstream faces, or contains space points that lie outside of the detector boundaries, the particle is deemed to be an unambiguous cosmic-ray muon.

The second phase of Pandora reconstruction, called *PandoraNu*, takes as input the subset of hits that have had all unambiguous cosmic-ray muon hits removed. Mirroring algorithms from PandoraCosmic, these hits are subject to 2D clustering, cross-plane matching, and 3D space point reconstruction. Space points are further divided by proximity and direction-based metrics into objects called "slices" that contain one candidate neutrino interaction. Beyond these steps, 3D neutrino vertex candidates are determined by matching the end points of 2D clusters across different planes and calculating a vertex score based on topology near the candidate vertex and knowledge of the beam direction, among other factors. The neutrino vertex is one of the variables used by a boosted decision tree (BDT) in the next step of reconstruction - the discrimination of track-like and shower-like particles. By combining multiple decision trees that rely on geometric and calorimetric information sequentially, the BDT assigns a "track score" between 0 and 1 to each particle, with scores close to 0 being shower-like and scores close to 1 being track-like. Particle refinement algorithms that collect missing remnants are then used to improve particle completeness. Finally, a particle hierarchy is assigned by working outward from the interaction vertex and building parent-daughter links along the way.

6.3.2 SPINE

Given the detailed nature of images produced in LArTPC experiments, techniques involving machine learning (ML) are generally well-suited for event reconstruction. At ICARUS, an end-to-end, deep-learning-based reconstruction chain known as SPINE (scalable particle imaging with neural embeddings) is applied in the selection and reconstruction of neutrino interactions. With 3D images of interaction events in the TPC as input, including both spatial information and reconstructed charge for each space point in the 3D image, SPINE uses a combination of convolutional neural networks (CNNs) and graph neural networks (GNNs) to perform clustering and identification of particles and interactions. Key components of the SPINE reconstruction chain are represented schematically in Figure 6.3 and are further discussed in the following subsections.

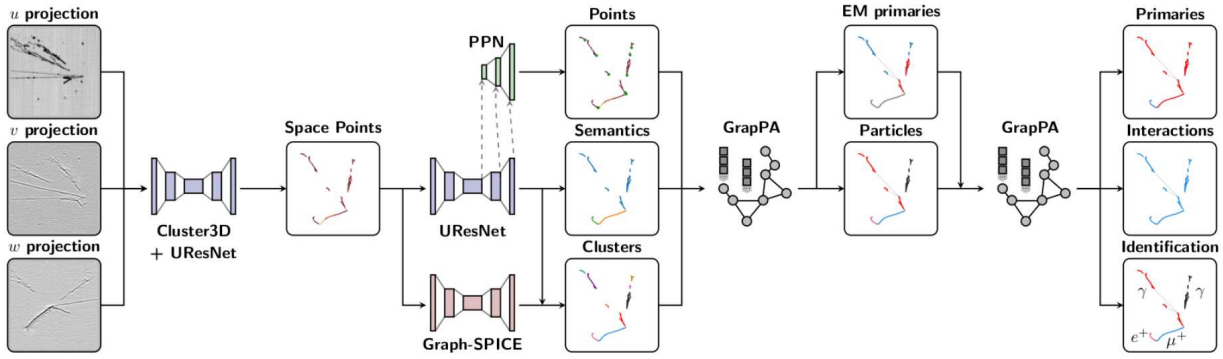

Figure 6.3: Schematic architecture of SPINE's end-to-end, machine-learning-based reconstruction chain for LArTPCs [57].

Tomographic Reconstruction

Before the SPINE reconstruction chain can deliver physics observables, 2D projections from each TPC wire plane must first be combined to form a 3D image. Known as tomographic reconstruction, this process begins by making all possible combinations of 2D hits across each wire plane that are consistent in time. A traditional algorithm called *Cluster3D* identifies these pairs of hits and forms 3D space points at the locations of intersecting wires. Designed to prioritize efficiency over purity, this process is highly effective at recovering the 3D positions of charge depositions at the cost of including tomographic artifacts corresponding to invalid combinations of 2D hits. Space points from an ICARUS data event, as well as the 2D hits used by Cluster3D to produce them, are shown in Figure 6.4.

Removal of tomographic artifacts, or "ghost points," is handled by a CNN architecture called *U-ResNet*. First popularized by its success in biomedical imaging [58], U-ResNet performs binary classification of space points, assigning them to ghost and non-ghost categories. Ghost points are removed, and the charge present in the image is rescaled by considering the number of times each hit is used in non-ghost space points. If a hit is used more than once, its charge is redistributed across the space points it contributes to. Non-ghost points, shown in Figure 6.5 for the same ICARUS data event as in Figure 6.4, are then passed on to the next stage of SPINE reconstruction.

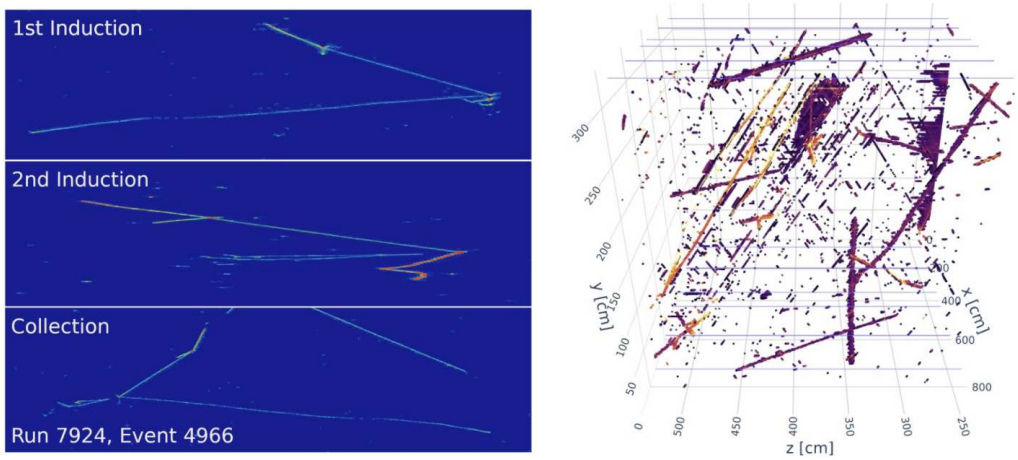

Figure 6.4: 2D hits from each wire plane corresponding to an ICARUS data event (left) and 3D space points from the same event as found by Cluster3D (right). Tomographic artifacts are notably visible in the 3D space point distribution and are a consequence of reconstruction with a projective wire readout.

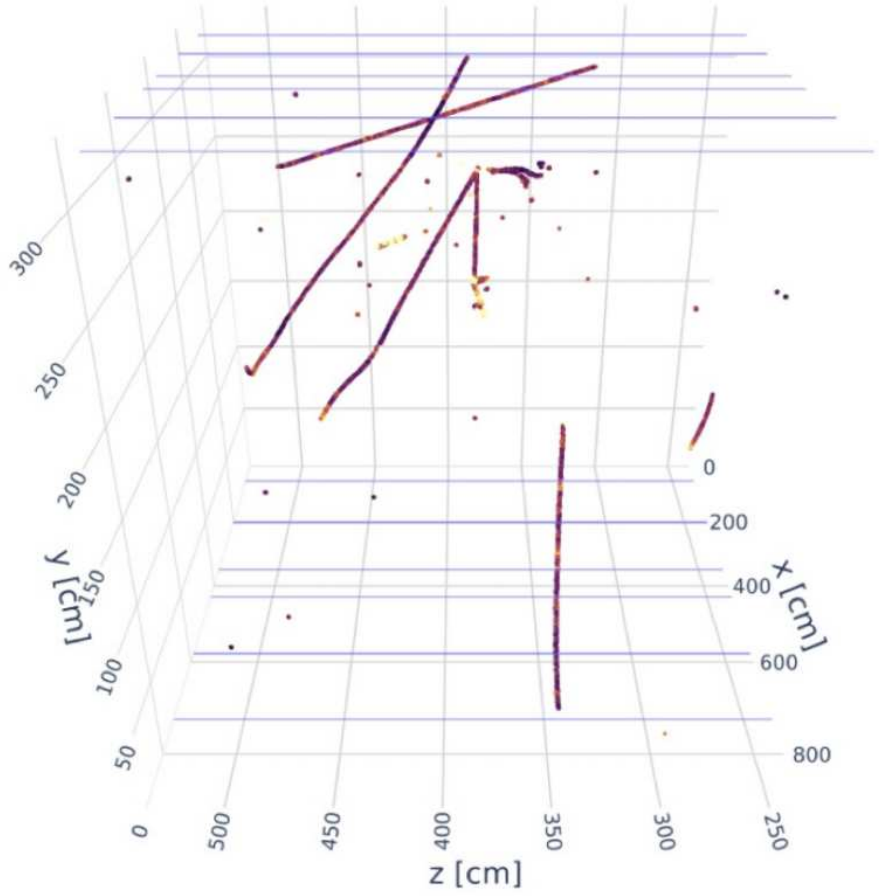

Figure 6.5: 3D space points from an ICARUS data event after the removal of tomographic artifacts.

Voxel-Level Feature Extraction and Dense Clustering

Space points from the tomographic reconstruction stage make up 3D images that are fed to the first module of the SPINE reconstruction chain: U-ResNet. Previously used for ghost point removal, U-ResNet is now tasked with particle-type classification of each 3D pixel, or voxel, and identification of points of interest. In the particle-type classification of voxels, scores are assigned for the following semantic classes:

- **Electromagnetic showers:** Electromagnetic cascades induced by electrons, positrons, and photons.
- **Tracks:** Track-like trajectories associated with muons and charged hadrons.
- **Michel electrons:** Electrons produced from the decay of muons.
- **Delta rays:** Knock-on electrons produced from the hard scattering of ionizing particles.
- **Low-energy depositions:** Isolated energy depositions produced from Bremsstrahlung and subsequent Compton scattering (or pair production) of photons.

The semantic class with the highest score is the predicted particle type for each voxel, and is used downstream in particle superstructure formation.

Within the U-ResNet architecture, additional convolutional layers are used to locate points of interest in each 3D image. Known as the Point Proposal Network (PPN), these convolutional layers are responsible for the prediction of track end points and shower start points. These quantities are then used as input for post-processing algorithms such as neutrino interaction vertex reconstruction and are also used directly in the calculation of numerous reconstructed observables that will be discussed in Section 8.4.

A final task involving CNNs is dense clustering, or the density-based clustering of space points that belong to common semantic classes. For this, a U-ResNet architecture named *Graph-SPICE* is employed. Graph-SPICE applies a coordinate transformation to input voxels such that clusters are

disconnected, then uses a nearest-neighbor algorithm to find connected components. The output of dense clustering is a collection of particle fragments for semantic types like tracks and showers.

Particle Superstructure Formation

Following dense clustering, the next stage of SPINE reconstruction centers on the aggregation of particle fragments into complete track and shower objects. Unlike previous steps that were achieved with CNNs, the task of particle aggregation makes use of GNNs due to the natural graph-like representation of particles. Specifically, the *GrapPA* (Graph Particle Aggregator) network treats particle fragments (e.g. spatially-separated shower fragments) as input graph nodes and the correlations between them (e.g. the invisible photons connecting them) as input graph edges. By leveraging features of these nodes and edges, such as PPN points and displacement vectors, GrapPA performs binary edge classification to group fragments belonging to the same particle instance together. The result is a series of updated nodes and edges representing particle objects that can be used in the next stage of reconstruction.

With distinct particle objects in hand, particles that originate from the same neutrino interaction can be grouped together. Known as interaction aggregation, this task again uses GrapPA - now using particle instances as input graph nodes and the gaps between them as input graph edges. At this stage, nodes are also assigned scores for particle identification (also known as PID) and "primaryness" (whether or not the particle originated from the neutrino interaction vertex). PID classification includes photons, electrons, muons, pions, and protons, while primary classification is either primary or non-primary. The output of this stage, and the final output of SPINE's neural networks, is a set of interactions and the particles belonging to them. An example of one such interaction from ICARUS data is shown in Figure 6.6.

Network Training

SPINE networks are trained in a supervised setting, meaning they rely on labeled datasets in which desired network outputs (e.g. semantic type, PID) are known a priori. With use of these labeled datasets, gradient-based methods of loss minimization are performed that allow the networks

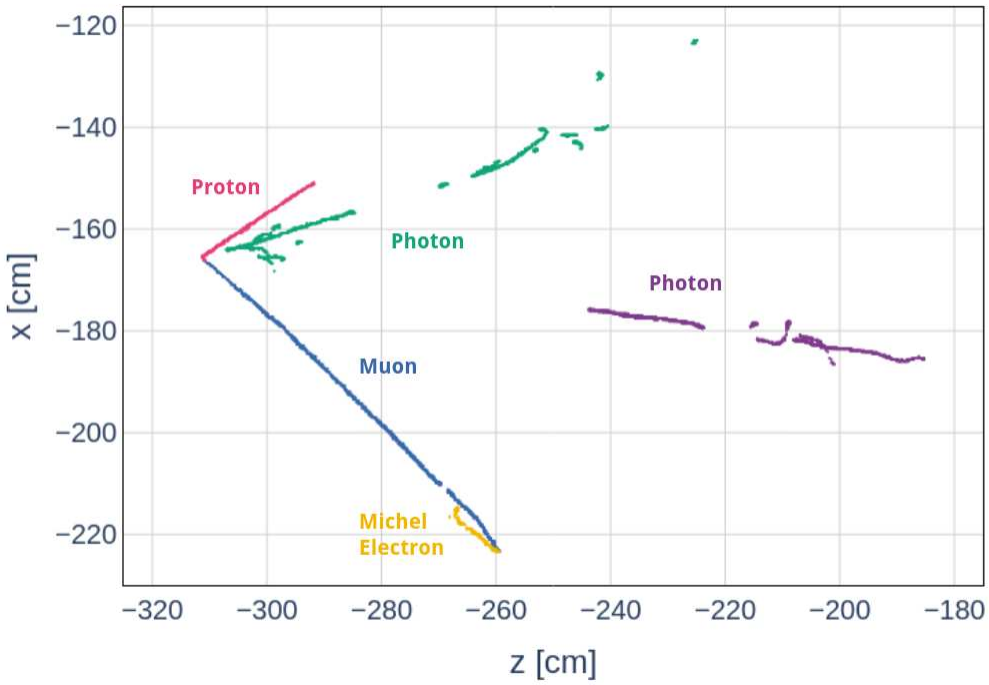

Figure 6.6: An interaction from ICARUS data that has been reconstructed with SPINE. Different colors represent distinct particle instances predicted by SPINE's neural networks.

to learn a mapping from input features to output targets. Network parameters are optimized in this process, and then applied to unlabeled datasets in order to infer relevant details.

Given the availability of truth information, MC simulation serves as the labeled dataset for training SPINE. To avoid any potential biases that could arise due to training on events from a specific neutrino interaction model, two physics-agnostic event generators are utilized:

- **Multi-Particle Vertex (MPV):** Generate a configurable number of particles emanating from a common vertex. Particles include electrons, positrons, muons, antimuons, charged pions, neutral pions, and protons.
- **Multi-Particle Rain (MPR):** Generate a configurable number of isolated particles that do not share a common vertex and originate from outside the detector, as to mimic cosmic activity. Particles include muons, antimuons, electrons, photons, and protons.

By design, MPV events are similar to what might be expected from a neutrino interaction, while MPR events mimic cosmic-ray secondaries passing through the detector. In each case, particle en-

ergies are sampled from pre-defined kinematic ranges that are intended to encompass the expected particle kinematics. As is the case with any other generator, particles from the MPV/MPR generators are passed through the detector simulation stage of the ICARUS simulation chain, ensuring detector effects are represented in the training datasets.

Post-Processing

Within the SPINE reconstruction framework, a series of non-machine-learning algorithms exist that are applied downstream of the neural network cascade mentioned in the previous subsections. Known as post-processors, these algorithms are responsible for the following tasks:

- **Particle direction reconstruction:** Reconstruct particle direction with respect to the particle start point. Direction is taken as the normalized mean direction of all space points belonging to the particle.
- **Track length reconstruction:** Reconstruct length of track-like particles by summing track segment lengths found through principal component analysis.
- **Interaction vertex reconstruction:** Identify location of prospective neutrino interaction vertex based on the confluence of track end points.
- **Fiducial volume classification:** Classify interactions as occurring within a configurable detector fiducial volume. This classification is based on the location of the reconstructed neutrino interaction vertex.
- **Optical flash association:** Determine matches between reconstructed charge clusters in each TPC and reconstructed optical flashes from PMTs. Comparisons are made between the expected mean photoelectron distribution across the PMTs associated with a charge cluster and the observed photoelectron distributions associated with the reconstructed optical flashes using a log-likelihood approach, allowing a score to be assigned to each cluster-flash pair.

- **Containment classification:** Classify interactions and particles as being contained or non-contained. An object is considered contained if all relevant space points are a minimum, configurable distance away from the faces of the detector active volume.

- **Particle energy reconstruction:** Estimate the kinetic energy of particles through a variety of means. The methods employed in this analysis are described in the following section.

6.3.3 Particle Energy Reconstruction

In order to estimate the energies of neutrinos incident on ICARUS, it is typically necessary to measure the energy of particles produced in ν-Ar interactions. Additionally, the reconstructed energies of these secondaries is critical in measuring differential cross sections as functions of kinematic observables. A range of techniques can be used to measure particle energies, with the chosen method often depending on whether the particle has been identified as a track or shower object and on whether or not the particle is fully-contained within the detector.

For particles with track-like signatures, a "best-estimate" approach is taken in energy reconstruction. First, the containment post-processor is used to determine if the particle is contained within the detector active volume. If so, the particle's kinetic energy is inferred from the Continuous Slowing Down Approximation (CSDA) that relates a particle's kinetic energy to its range in a material. Tabulated values from this approximation exist for numerous particles in liquid argon and are determined by integrating the inverse Bethe-Bloch formula. Figure 6.7 shows how this method of energy reconstruction compares to the true muon kinetic energy for a sample of contained muons in a simulation of BNB neutrinos and cosmics at ICARUS.

The energy of track-like particles that exit the detector cannot be estimated with the range-based approach, as the CSDA method requires the full extent of the track to be contained. Instead, kinematic information about the particle is inferred from small-angle deflections along its trajectory due to multiple Coulomb scattering (MCS). The Highland formula [59] relates the root mean

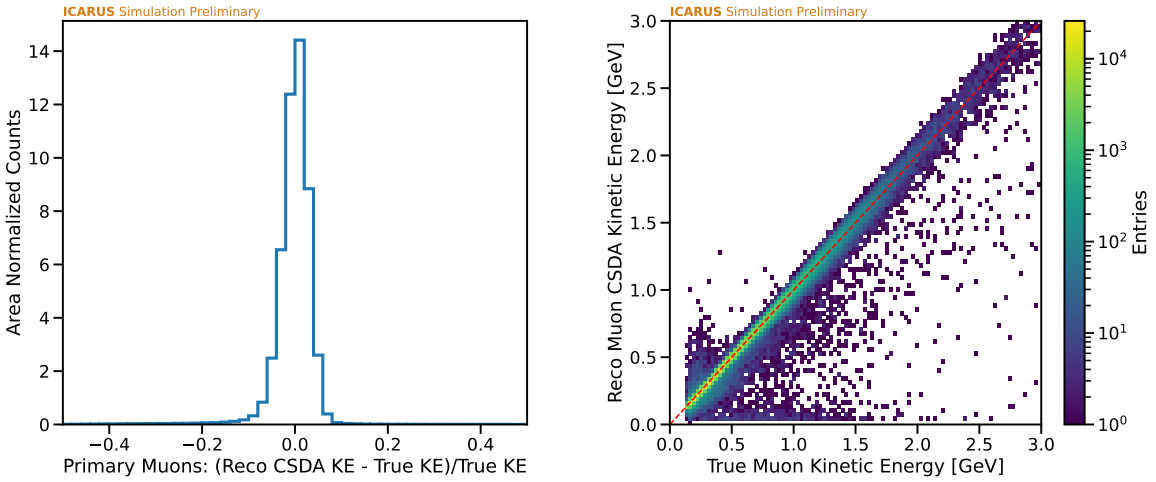

Figure 6.7: Comparison of range-based kinetic energy reconstruction to true energy for contained muons in a simulation of BNB neutrinos and cosmics at ICARUS.

square of the scattering angle distribution σ_{HL} to the particle's momentum p as follows:

$$\sigma_{\text{HL}} = \frac{13.6\ \text{MeV}}{p\beta c} z \sqrt{\frac{l}{X_0}} \left[1 + 0.038 \ln\left(\frac{l}{X_0} \right) \right], \tag{6.4}$$

where β is the ratio of the particle's velocity to the speed of light c, z is the electric charge magnitude of the particle, l is the distance the particle travels through the detector medium, and X_0 is the radiation length of the target material. Equation 6.4 allows for observed scattering angles to be compared to various momentum hypotheses in a log-likelihood scan. The particle's kinetic energy can then be calculated from the relativistic energy-momentum relation. Figure 6.8 shows how this method of energy reconstruction compares to the true muon kinetic energy for a sample of contained muons in a simulation of BNB neutrinos and cosmics at ICARUS.

The energy of electrons and photons is inferred from the electromagnetic showers these particles instigate in the detector medium. Shower energy is estimated calorimetrically by summing charge depositions belonging to the shower and accounting for detector effects that arise from TPC electronics gain, recombination, and electronegative impurities in argon. The exact form of

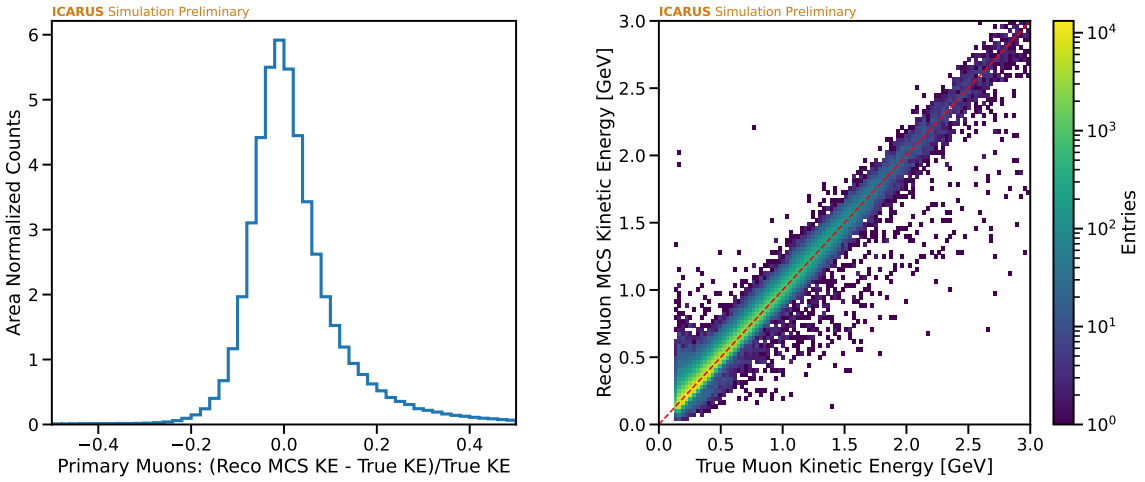

Figure 6.8: Comparison of MCS-based kinetic energy reconstruction to true energy for contained muons in a simulation of BNB neutrinos and cosmics at ICARUS.

the shower energy expression used in most SPINE-based analyses is presented in Equation 6.5:

$$E_{\text{shower}} = W_{\text{ion}} \left[\frac{\text{MeV}}{\text{e}^-}\right] \cdot C_{\text{cal}} \left[\frac{\text{e}^-}{\text{ADC}}\right] \cdot C_{\text{adj}} \cdot \frac{1}{R} \cdot \sum_i e^{\frac{t_{\text{drift}}}{\tau}} \cdot Q_i \,[\text{ADC}]\,. \tag{6.5}$$

Here, W_{ion} is the work function for ionizing an argon atom and corresponds to approximately 23.6 eV. The calibration constant C_{cal} is used to convert measured collection plane charge Q_i from detector units (ADC) to physical units (electrons) and is found to be approximately 75 e^-/ADC from studies involving stopping muons at ICARUS [51]. More information on the derivation of this constant can be found in Section 7.1. The fraction of drift electrons that survive electron-ion recombination is given by the term R, which is taken as approximately 0.68 at ICARUS. This flat correction factor comes from the Modified Box model for minimum-ionizing particles at the nominal ICARUS electric field. The exponential term inside the sum accounts for charge attenuation due to electronegative impurities in argon, which is roughly a 10% effect at ICARUS. In this term, the electron drift velocity is given by t_{drift} and τ is the electron lifetime, which is further discussed in Section 7.1.

Equation 6.5 also includes a multiplicative factor to account for missing energy due to sub-threshold charge and clustering inefficiencies. Named C_{adj}, this factor is derived heuristically from

a study of contained electromagnetic showers in a simulation of BNB neutrinos and cosmics. Reconstructed shower energies (calculated without C_{adj}) are compared against the true initial energies of the instigating particle in Figure 6.9, with their ratio being studied as a function of the true intitial energy of the particle. Double-sided Crystal Ball fits [60] are performed in each true energy bin, with the fit function being characterized by a Gaussian core with power-law tails:

$$f(x;\mu,\sigma,\alpha_L,n_L,\alpha_R,n_R) = \begin{cases} A_L \cdot \left(B_L - \frac{x-\mu}{\sigma}\right)^{-n_L} & \text{for } \frac{x-\mu}{\sigma} < -\alpha_L \\ \exp\left(-\frac{(x-\mu)^2}{2\sigma^2}\right) & \text{for } -\alpha_L \leq \frac{x-\mu}{\sigma} \leq \alpha_R \\ A_R \cdot \left(B_R + \frac{x-\mu}{\sigma}\right)^{-n_R} & \text{for } \frac{x-\mu}{\sigma} > \alpha_R, \end{cases} \tag{6.6}$$

where x is the fit variable, μ and σ are the mean and standard deviation of the Gaussian core, α_L (α_R) specifies the transition point from Gaussian to power-law for the left (right) tail, and n_L (n_R) is the power of the left (right) tail. The constants A_i and B_i, where $i = L$ for the left tail and $i = R$ for the right tail, ensure the function is continuous and are given by

$$A_i = \left(\frac{n_i}{|\alpha_i|}\right)^{n_i} \cdot \exp\left(-\frac{|\alpha_i|^2}{2}\right), \quad B_i = \frac{n_i}{|\alpha_i|} - |\alpha_i|. \tag{6.7}$$

Fits are performed in each true energy bin and the Gaussian component means are averaged across all true energy bins to yield the reciprocal of C_{adj}. After applying this correction, reconstructed shower energies show good agreement with true energies, as seen in Figure 6.10.

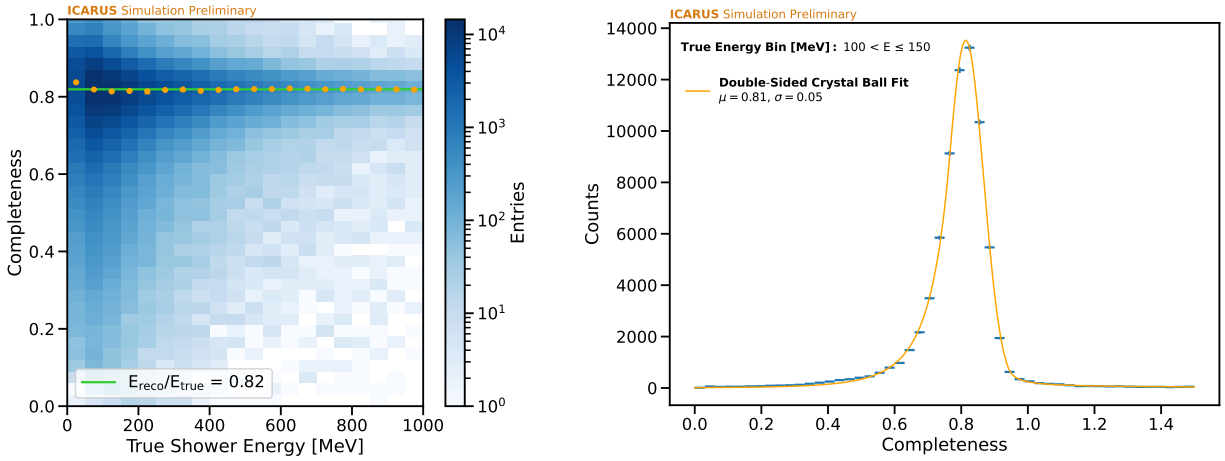

Figure 6.9: Shower energy completeness as a function of true shower energy, where completeness is defined as the ratio of reconstructed energy to true energy (left plot). The reported completeness in each true bin (orange markers in left plot) is found using a double-sided Crystal Ball fit as described in the text (right plot).

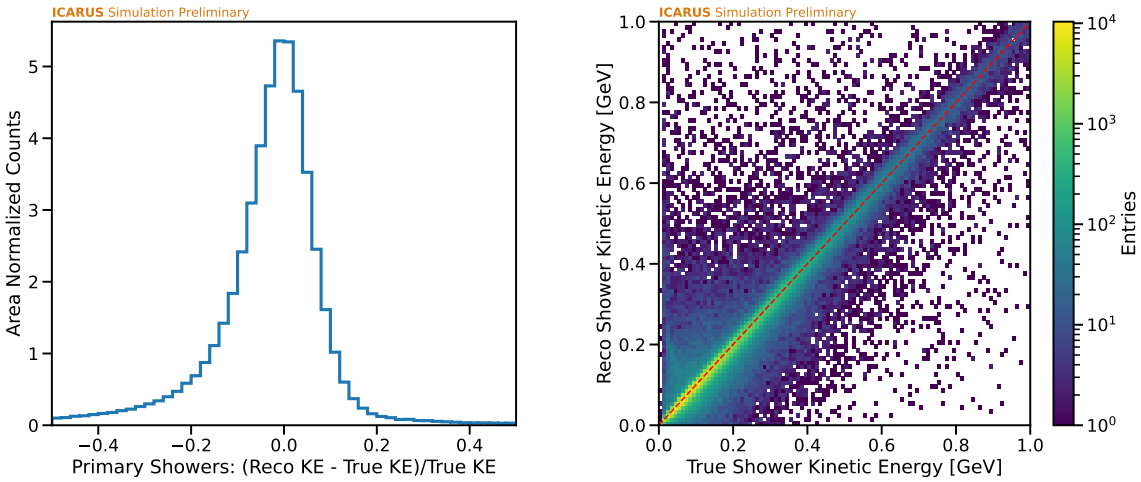

Figure 6.10: Comparison of reconstructed shower energy to true shower energy for contained primary showers in a simulation of BNB neutrinos and cosmics at ICARUS.

Chapter 7

Detector Calibration

To ensure that particle position and energy are reconstructed with as much precision as possible, ICARUS maintains an extensive detector calibration program. Calibrations at ICARUS serve to pin down detector effects that can lead to biased measurements, as well as improve agreement between data and simulation. Broadly speaking, these calibrations fall into one of two categories: "low-level" calibrations that characterize detector response nonuniformities and temporal variations, and "high-level" calibrations that probe the reconstructed particle energy scale using well-understood particle energy spectra. This chapter highlights the former class of calibrations, beginning with those relevant to charge and energy scale equalization in Section 7.1. Electric field distortions are examined in Section 7.2, followed by a discussion on cathode nonplanarity in Section 7.3.

7.1 Charge and Energy Scale Equalization

Charge scale equalization refers to the procedures implemented in order to ensure each TPC's response to ionization charge is uniform in space and time. In practice, charge scale equalization centers on the quantity dQ/dx, defined as the detected ionization charge per unit length associated with particles traversing the detector. Various detector effects can alter the TPC charge response, including electron diffusion, charge attenuation due to electronegative impurities in the liquid argon, and wire plane intransparency. These effects and their corrections are discussed in this section.

7.1.1 Electron Diffusion

Clouds of free electrons produced by ionizing particles in liquid argon have a tendency to spread, or diffuse, as they drift in an electric field. As a non-isotropic effect, characterization of electron diffusion requires measurements of separate components relative to the applied electric field: longitudinal diffusion (parallel to the applied electric field) and transverse diffusion (per-

pendicular to the applied electric field). Diffusion constants D_L and D_T quantify the extent of ionization cloud spread, which is given as σ_L and σ_T in Equations 7.1 and 7.2 for the longitudinal and transverse components, respectively.

$$\sigma_L = \sqrt{2 \cdot D_L \cdot t_{\text{drift}}} \tag{7.1}$$

$$\sigma_T = \sqrt{2 \cdot D_T \cdot t_{\text{drift}}} \tag{7.2}$$

In the above expressions, t_{drift} is the electron drift time. The longitudinal spreading of charge amounts to a broadening of collected signal waveforms and therefore impacts the detector spatial resolution in the drift direction. On the other hand, transverse diffusion results in smearing in the plane transverse to the ionization drift direction, broadening the length of particle trajectories observed by the wires. Measurements of D_L and D_T have been made at ICARUS, with the latter being the first of its kind for an electric field below 1 kV/cm. By comparing the charge scale of near-anode and near-cathode cosmic-ray muon data, diffusion constant values of $D_L = 4.01 \pm 0.18$ cm^2/s and $D_T = 7.57 \pm 0.11$ cm^2/s were found [61].

7.1.2 Wire Plane Intransparency

While the ICARUS TPCs are designed to maximize ionization charge collection efficiency, intransparencies of the induction planes have been observed to limit the amount of charge that would otherwise reach the collection plane. This absorption of charge on induction wires is likely due to failures in wire bias application or inter-wire spacing variations, ultimately leading to a $\sim$20% variation in charge response. To account for this, measurements of the charge response using cosmic-ray muons have been carried out, yielding correction maps in the plane transverse to the ionization drift direction in each TPC. By summing charge across neighboring wires to limit effects from diffusion in the measurement, an effective dQ/dx is calculated, and after averaging across many different cosmic tracks at a given location in the detector, can be used to obtain a local scale factor in the aforementioned correction map.

7.1.3 Electron Lifetime

Electronegative impurities in liquid argon, namely O_2 and H_2O, absorb ionization electrons as they drift, exponentially attenuating the detected ionization charge signal. The degree of attenuation is commonly parameterized with a quantity known as the "electron lifetime," or τ as it is referenced in the following equation:

$$Q = Q_0 e^{-t_{\text{drift}}/\tau} \tag{7.3}$$

where Q is the detected ionization charge, Q_0 is the initial ionization charge, and t_{drift} is the electron drift time. At ICARUS, the electron lifetime has been assessed in each cryostat using cosmic muons that have been tagged as crossing both the cathode and an anode. By applying an exponential fit to most-probable dQ/dx values as a function of drift time, the electron lifetime is extracted for each DAQ run and used for equalization of charge response in the TPC drift direction. Depending on the cryostat and run period, the ICARUS electron lifetime has ranged from roughly 4 ms to roughly 8 ms, corresponding to a maximum signal attenuation of approximately 20%.

7.1.4 Calibrated Response

Figure 7.1a shows the effects of charge scale equalization on ICARUS Run 1 and Run 2 data. In assessing coarse-grained collection plane dQ/dx measurements of throughgoing cosmic-ray muon tracks, clear changes in scale and improvements in resolution are seen with the application of calibrations in the drift direction (electron lifetime correction) and the plane transverse to the drift direction (wire intransparency correction).

With the TPC charge response equalized, it is then possible to calibrate the energy scale with a selection of stopping tracks. From Landau-Vavilov theory, the energy loss per unit length of these tracks, or dE/dx, is well known. By fitting measured dQ/dx values to expected dE/dx values using an electron-ion recombination model, the reconstructed energy scale is obtained. At ICARUS, the Ellipsoidal Modified Box model of electron-ion recombination is employed [51], taking into account the angles of particle trajectories relative to the electric field direction. Figure 7.1b shows

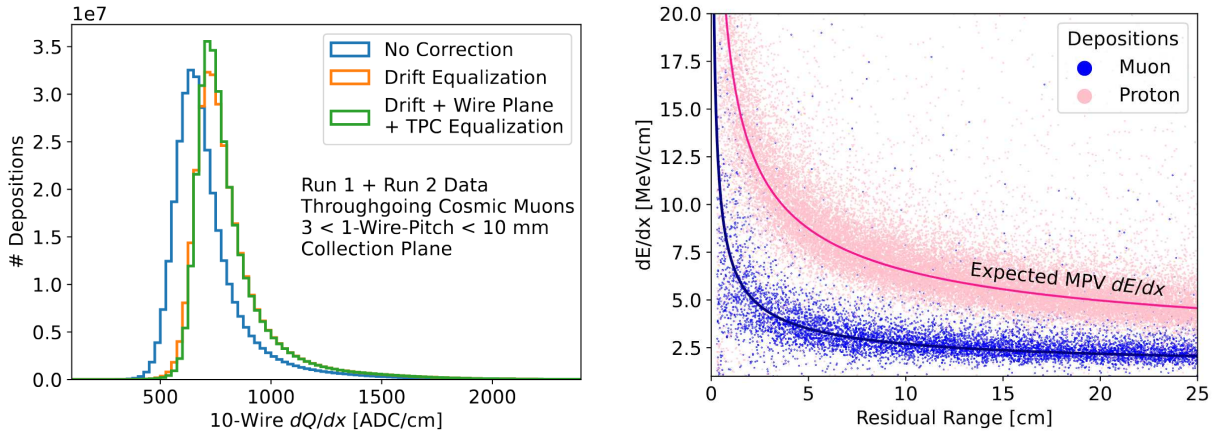

(a) **(b)**

Figure 7.1: (a) Effects of charge scale equalization on throughgoing cosmic-ray muon dQ/dx measurements [54] and (b) results of energy scale calibration as seen with stopping muon and proton dE/dx measurements as a function of residual range [51].

calibrated dE/dx values from ICARUS Run 1 data as a function of the distance to the end of the particle trajectory, referred to as the "residual range" of the reconstructed particle track. For both muons and protons, excellent agreement is observed with respect to expectations from Bethe-Bloch theory.

7.2 Electric Field Distortions

LArTPC-based experiments rely on a uniform electric field to drift ionization electrons toward the readout anode(s) of the detector. It is important to understand any nonuniformities, or distortions, of the electric field due to the effects these have on observables in reconstructed events. For one, the position and time of arrival for ionization electrons at the anode is affected by electric field distortions, therefore limiting the ability to accurately reconstruct the positions of charge depositions. In addition, the amount of reconstructed charge is affected by electric field distortions, as the fraction of ionization electrons that recombine with argon atoms is dependent on the electric field strength.

7.2.1 Overview of Space Charge Effects

While electric field distortions can arise for a number of reasons, a leading cause at surface-level detectors like ICARUS is ionization from cosmic-ray muons. As the ionization electrons from cosmic-ray muons drift toward the anode with a speed of $v_{\text{drift}} \sim 1.55\,\text{mm/}\mu\text{s}$, the larger Ar^+ ions drift toward the cathode roughly five orders of magnitude more slowly at $v_{\text{drift}}^{\text{Ar}^+}$. The slow-moving Ar^+ ions accumulate in the detector, and the build-up of positive charge leads to distortions of the electric field and associated distortions in reconstructed positions of energy depositions in the detector. Collectively known as space charge effects (SCE), these distortions can bias crucial particle identification quantities like dE/dx, which is dependent on both the electric field and spatial position associated with energy deposition.

The solution for space charge density can be derived analytically in the approximation of a TPC as a parallel-plate capacitor. Assuming only drift-coordinate dependence (a valid assumption for the bulk of the ICARUS active volume given its large transverse extent), the equation for charge continuity states

$$\frac{\partial \rho^+}{\partial t} + \frac{\partial (\rho^+ v_{\text{drift}}^{\text{Ar}^+})}{\partial x} = J, \tag{7.4}$$

where ρ^+ is the positive ion density and J is the charge density injection rate. Drift dependence is given by x, with $x = 0$ corresponding to the position of the anode. In the stationary state, ρ^+ does not vary with time and Equation 7.4 is solved as

$$\begin{aligned} \rho^+(x) &= \frac{Jx}{v_{\text{drift}}^{\text{Ar}^+}} \\ &= \frac{Jx}{\mu_{\text{Ar}^+}\mathcal{E}_x} \end{aligned} \tag{7.5}$$

where μ_{Ar^+} is the mobility of the argon ions in liquid argon and $\mathcal{E}_x$ is the component of the electric field in the drift direction. From Equation 7.5, it is seen that the density of positive ions increases approximately linearly with distance from the anode. The estimated positive ion density under the previously described assumptions is shown for ICARUS in Figure 7.2. The charge injection rate J is calculated from the estimated ICARUS cosmic-ray muon flux and taken to be

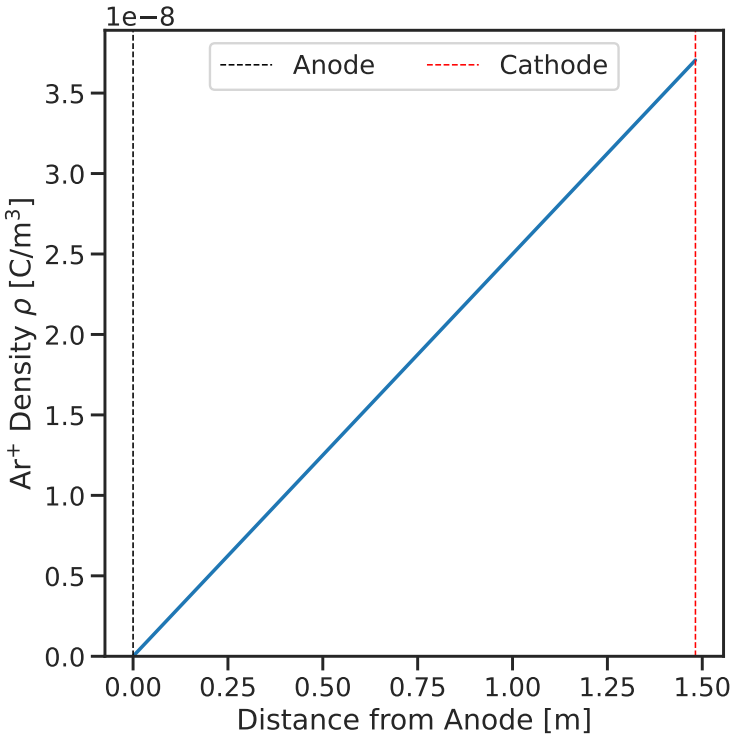

Figure 7.2: Estimated positive Ar^+ density at ICARUS. Ion concentration is minimal at the anode and maximal at the cathode.

$2 \times 10^{-10}\,\mathrm{C\,m^{-3}\,s^{-1}}$, while $v_{\mathrm{drift}}^{\mathrm{Ar}^+}$ is estimated to be 8 mm/s from previous studies of ion mobilities in cryogenic liquids [62].

The local electric field in the presence of space charge can be solved from Gauss's law, which states that the divergence of the electric field is proportional to the local charge density:

$$\frac{\partial \mathcal{E}_x}{\partial x} = \frac{\rho^+}{\epsilon_r \epsilon_0}, \tag{7.6}$$

where ϵ_r is the permittivity of liquid argon and ϵ_0 is vacuum permittivity. Substitution of Equation 7.5 into Equation 7.6 yields the electric field solution as a function of drift coordinate:

$$\mathcal{E}_x(x) = \mathcal{E}_0 \sqrt{\left(\frac{\mathcal{E}_a}{\mathcal{E}_0}\right)^2 + \alpha^2 \left(\frac{x}{D}\right)^2}, \tag{7.7}$$

where $\mathcal{E}_0$ is the electric field in the absence of space charge, $\mathcal{E}_a$ is the electric field at the anode, D is distance between the anode and cathode. A dimensionless constant α is also introduced as

$$\alpha = \frac{D}{\mathcal{E}_0}\sqrt{\frac{J}{\epsilon_r \epsilon_0 \mu_{\mathrm{Ar}^+}}}. \tag{7.8}$$

From Equation 7.7, it is seen that space charge effects decrease the nominal electric field strength near the anode and increase the nominal electric field strength near the cathode.

7.2.2 Measuring Spatial Offsets

In order to unfold the electric field distortions that result from space charge in the detector, the reconstructed positions of energy depositions associated with cosmic-ray muons are studied. Comparison of the reconstructed position of an energy deposition to its expected position (in the absence of space charge) yields the displacement, or spatial offset, due to SCE. Two different approaches for measuring spatial offsets are presented here, one of which focuses on spatial offsets in the plane transverse to the ionization drift direction ("transverse" spatial offsets) and the other on spatial offsets in the direction parallel to the ionization drift direction ("longitudinal" spatial offsets).

Transverse Component

Characterization of transverse spatial offsets relies on throughgoing muons that enter the detector through one TPC face and exit the detector through another. By definition, each end point of a throughgoing track is located at one of the unique faces of the TPC (i.e. top, bottom, upstream, downstream). However, in the presence of space charge, the reconstructed positions for the track end points can be shifted away from these faces due to the inward pull of drifting ionization electrons toward positive ions. The measured spatial offset between reconstructed track end points and TPC faces is a proxy for the component of SCE transverse to the ionization drift direction.

Figure 7.3 shows the distribution of throughgoing track end points from ICARUS Run 2 data, clearly showing the signature of SCE. Near the anodes, the density of space charge is minimal

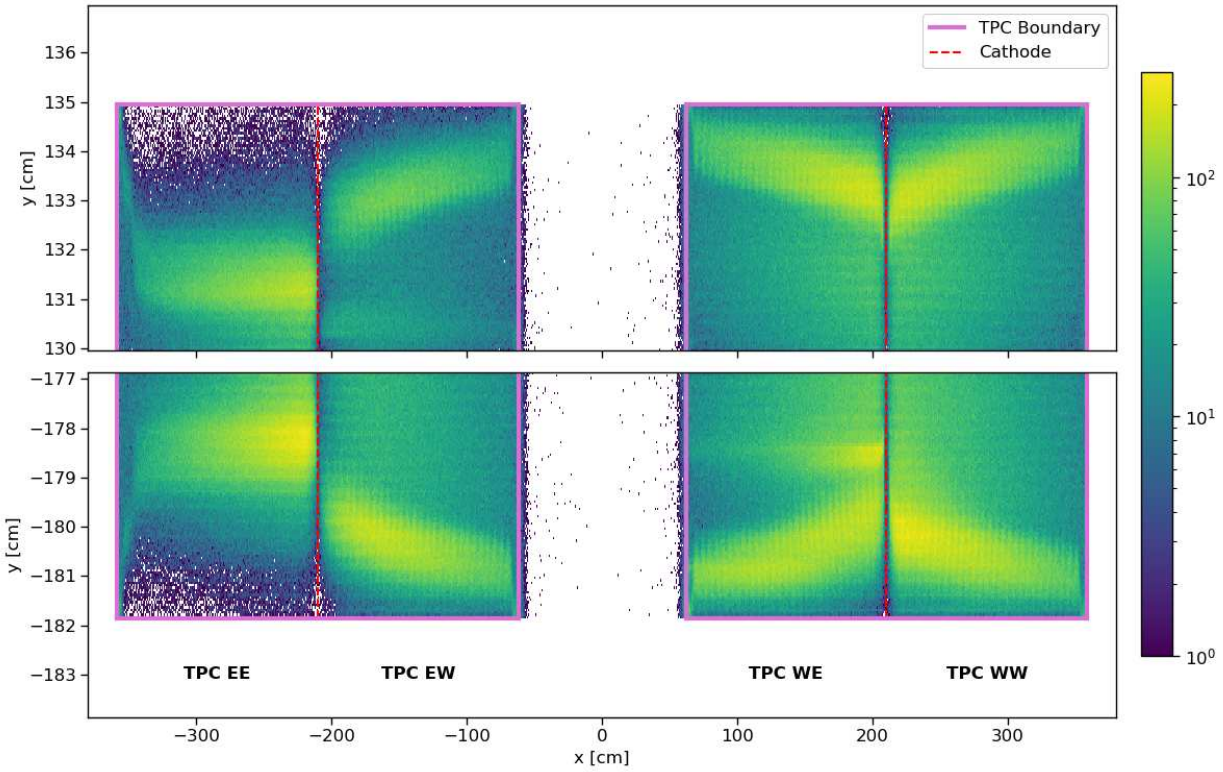

Figure 7.3: Throughgoing track end points associated with cosmic-ray muons from ICARUS Run 2 BNB data. In the absence of electric field distortions, end points are expected to be distributed along the TPC boundaries.

and track end points are positioned near the TPC faces. Space charge density is largest near the cathode, as evidenced by the maximal displacement of track end points from the TPC faces in this region ($\sim$3 cm). In TPC EE, electric field distortions beyond those from SCE can be seen, evidenced by the near-constant transverse spatial offset across the drift region. This distribution, when combined with monitoring data from the TPC high-voltage system, is consistent with a field cage short involving at least one electrode near the anode. The ability to see features like this show the utility of the throughgoing track sample, which has also been used to identify drift volume obstructions and dead readout wires in the detector.

Longitudinal Component

Given the dependence of ionization electron drift velocity on the electric field, Equation 7.7 implies that ionization electrons will experience a longer drift time in the presence of space charge as compared with a uniform electric field. This delay is given by

$$\begin{aligned}\delta t &= t_{\text{drift}}^{\text{SCE}} - t_{\text{drift}}^{\text{uniform}} \\ &= \int_0^x \left(\frac{1}{v_{\text{drift}}^{\text{SCE}}} - \frac{1}{v_{\text{drift}}^{\text{uniform}}} \right) dx' \\ &= \int_0^x \left(\frac{1}{\mu_{e^-} \mathcal{E}_x(x')} - \frac{1}{v_{\text{drift}}^{\text{uniform}}} \right) dx'\end{aligned} \tag{7.9}$$

where μ_{e^-} is the electron mobility in liquid argon. Upon substitution of Equation 7.7 into Equation 7.9, the ionization electron drift delay due to SCE can be written as

$$\delta t \simeq \alpha^2 \frac{\gamma \, t_{\text{D}}^{\text{uniform}}}{6} \frac{x}{D} \left(1 - \frac{x^2}{D^2} \right) \tag{7.10}$$

in the case of small α. The ionization electron drift time across the entire drift distance under a uniform electric field is given by $t_{\text{D}}^{\text{uniform}}$, while γ is introduced by Palestini in Ref. [63] to describe the nonlinearity of the ionization electron drift velocity:

$$\gamma \equiv \frac{\mathcal{E}_0}{v_{\text{drift}}^{\text{uniform}}} \frac{\delta v_{\text{drift}}}{\delta \mathcal{E}_x}. \tag{7.11}$$

Complementary to the previously-discussed throughgoing track studies that probe the transverse component of SCE, Equation 7.10 motivates the use of a different selection of cosmic-ray muons to assess the longitudinal component of SCE: anode-cathode-crossing tracks. The utility of this sample lies in the fact that reconstructed track space point positions near the anode and cathode are largely unaltered from SCE, which can be seen by substituting $x = 0$ or $x = D$ into Equation 7.10. Then, a straight line connecting the near-anode and near-cathode sides of the track gives an approximation of the particle trajectory in the absence of space charge. Comparison of the

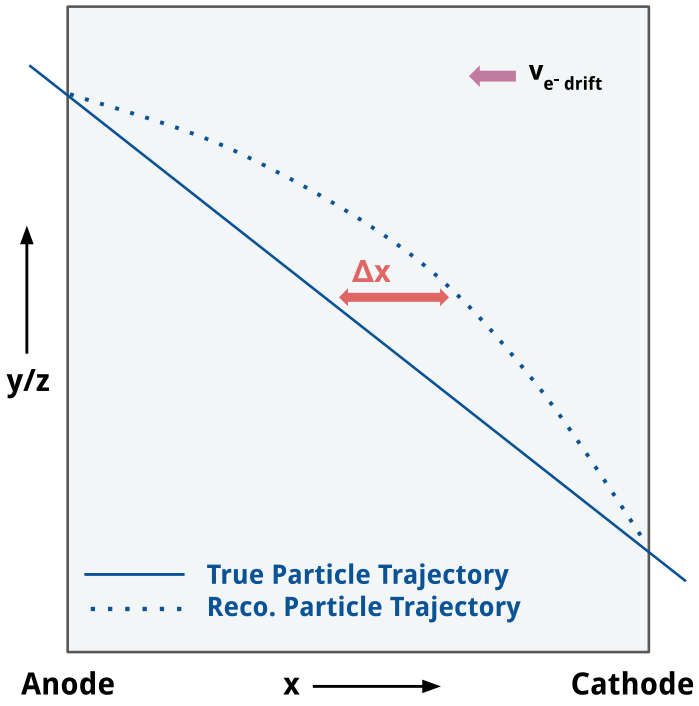

Figure 7.4: Illustration of longitudinal spatial offsets with an anode-cathode-crossing track. The dotted line shows reconstructed positions of energy depositions, which are offset from the true track trajectory (solid line) given the presence of electric field distortions associated with space charge effects in the detector.

reconstructed track space points to points that lie on the idealized trajectory reveals longitudinal spatial offsets and is illustrated for the two-dimensional case in Figure 7.4.

Longitudinal spatial offsets are shown in Figure 7.5 for ICARUS Run 2 data, with the median spatial offset highlighted in each TPC. For any given track, deflections from multiple Coulomb scattering contribute to smearing of the observed spatial offsets, but ultimately average to zero and do not introduce a bias to the measurement. A closer look at median spatial offsets for ICARUS Run2 and Run 3 data is shown in Figure 7.6, where the drift length of each TPC has been divided into ten-centimeter bins for the calculation. Good agreement is seen in three of the four TPCs (excluding TPC EE) when comparing ICARUS Run 2 data with a simulation including the modeling of space charge effects in the detector. This SCE simulation will be discussed in more detail in the next section.

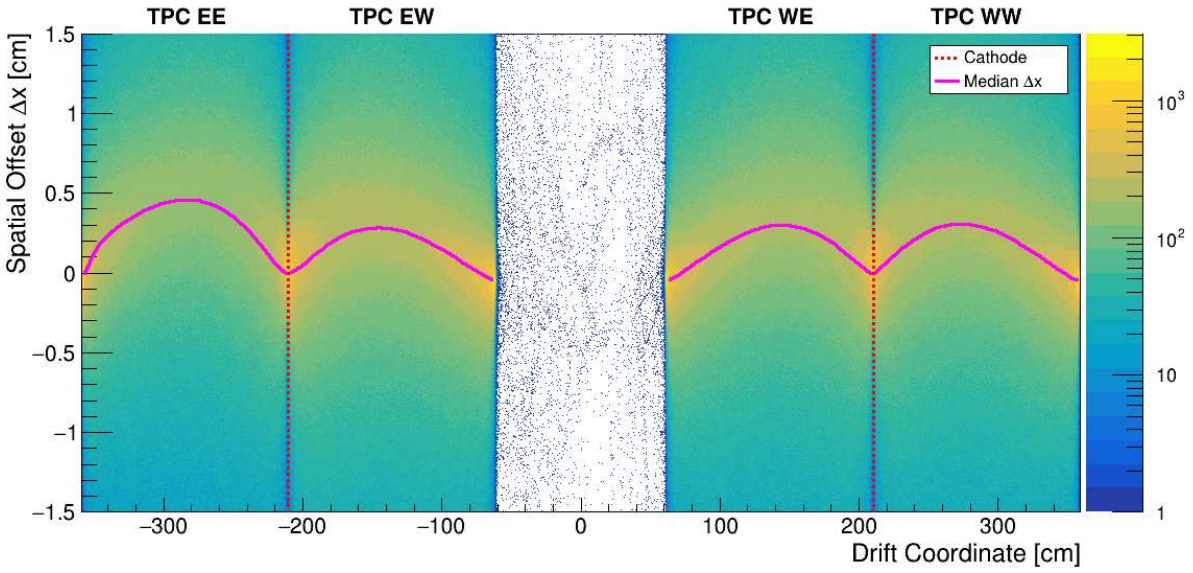

Figure 7.5: Longitudinal spatial offsets as a function of drift coordinate for all tracks in the anode-cathode-crossing sample. This study makes use of ICARUS Run 2 data.

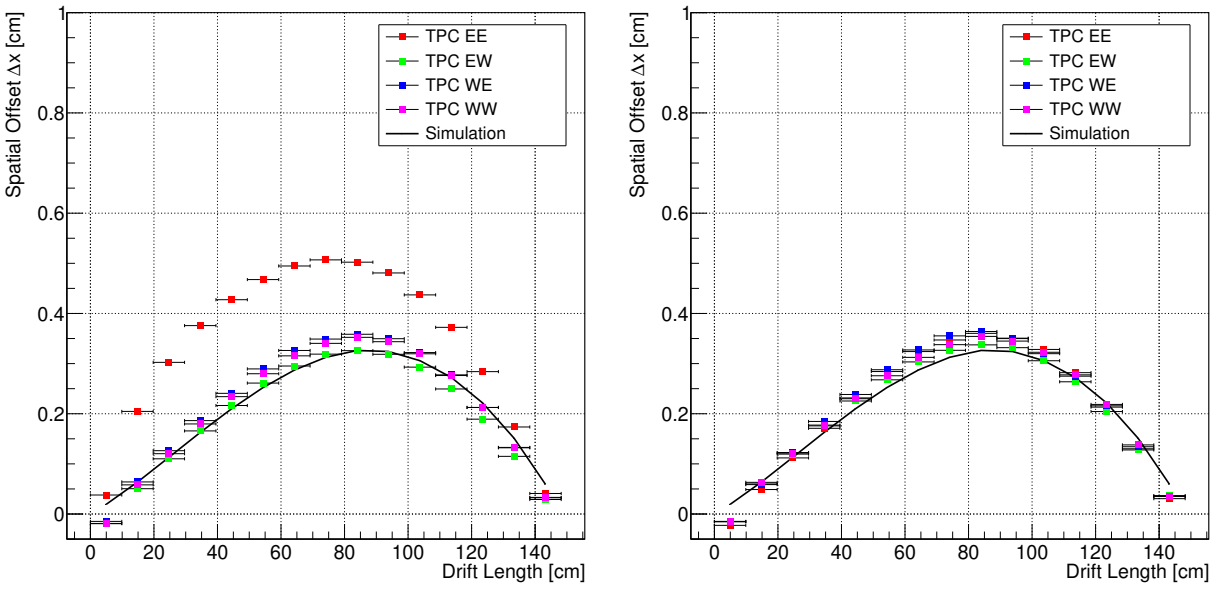

(a) ICARUS Run 2 data

(b) ICARUS Run 3 data

Figure 7.6: Longitudinal spatial offsets from ICARUS Runs 2 (a) and Run 3 (b). Colored markers indicate the median spatial offset in each drift bin across all tracks in the anode-cathode-crossing sample, while the black curve shows expected spatial offsets from simulation.

Comparisons between Run 2 and Run 3 in Figure 7.6 offers a glimpse at the time dependence of electric field distortions at ICARUS, with the most notable difference being the spatial offsets observed in TPC EE. The apparent reduction of spatial offset magnitude in this TPC from Run 2 to Run 3 is explained by the resolution of the previously-mentioned field cage short. During a period of neutrino beam downtime following Run 2, the cryogenic pump in the east cryostat was powered off to prepare for LAr filter regeneration. Upon resuming pump operation, measurements from the TPC high voltage monitoring system returned to pre-short values, hinting that vibrations from the pump may have eliminated the unintended electrical connection between field cage elements.

The time dependence of SCE is examined in more detail for ICARUS Run 2, which is the run period relevant to the ν_μ CC π^0 analysis presented in this thesis. For all DAQ runs with at least 500 anode-cathode-crossing tracks, the median of all longitudinal spatial offsets at least 5 cm away from the anode and cathode is calculated and presented in Figure 7.7. No systematic shift in the magnitude of spatial offsets is observed over time, thus highlighting the stability of SCE over Run 2. Figure 7.8 shows the overall variation of spatial offsets across Run 2, which is inferred from the distribution of all median values reported in the time dependence study and is estimated to be 8-11%, depending on TPC.

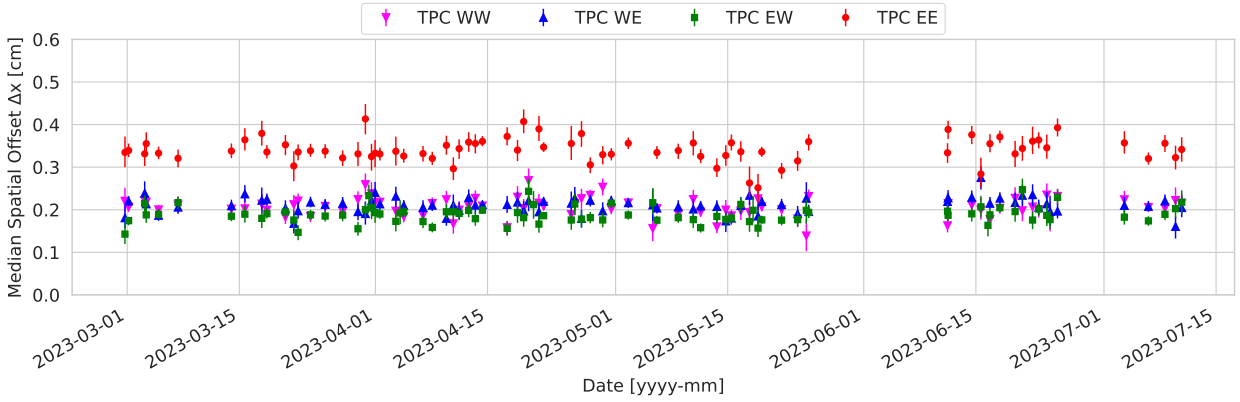

Figure 7.7: Median longitudinal spatial offsets as a function of time for ICARUS Run 2 data. Spatial offsets are not observed to vary significantly over the course of the run.

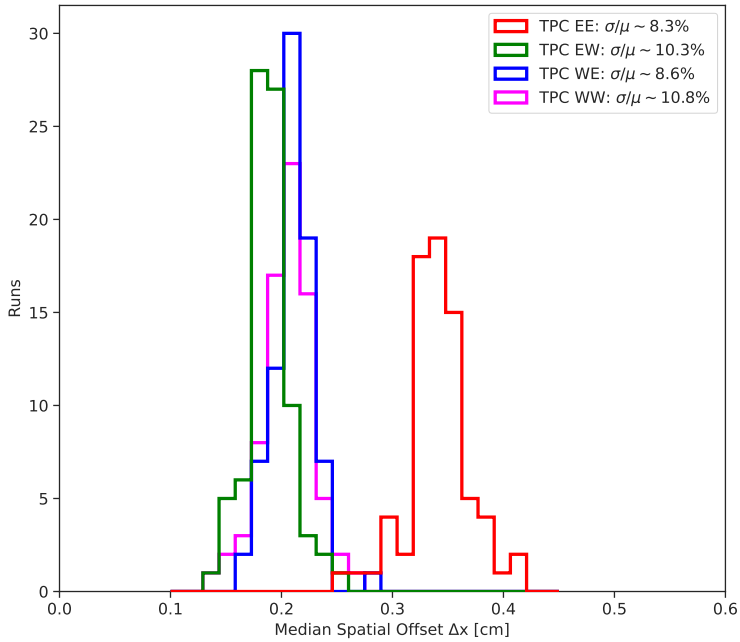

Figure 7.8: Median longitudinal spatial offset values from each DAQ run in ICARUS Run 2. The relative spatial offset variation in each TPC is taken as the quotient of the standard deviation and the mean of the distribution.

Calibration Deliverables

The aim of electric field calibration at ICARUS is twofold, seeking to inform the simulation of spatial and electric field offsets with data-driven measurements and providing a means of correcting for these offsets when performing a physics measurement with ICARUS data. Simulation of SCE at ICARUS, such as the predicted spatial offsets shown in Figure 7.6, begins with the boundary volume problem involving an assumed space charge density, taken as the function shown in Figure 7.2, and the uniformly varying voltage of the field cage dictated by the set cathode voltage. The Poisson equation is solved using a Fourier series solution, taking these inputs and yielding a map of the electric field distortions associated with SCE throughout the detector volume. Associated spatial offsets are calculated in a second step through use of a ray-tracing algorithm that determines impact to the reconstructed ionization electron position based upon the location of the original energy deposition in the detector.

Both the electric field distortions and spatial offsets are stored in 3D maps such that they are directly accessible in the ICARUS simulation chain. Slices of these maps along the beam direction

for Δy, Δx, and electric field offsets are shown in Figures 7.9, 7.10, and 7.11, respectively. It is through inversion of the spatial offset maps that corrections for reconstructed space point positions are obtained, while the simulated electric field map can be used directly to account for spatial variations in energy corrections due to the dependence of electron-ion recombination on electric field magnitude.

Given the relatively small scale of SCE at ICARUS and the fact that reconstructed spatial offsets show reasonable agreement with simulated spatial offsets, the nominal ICARUS SCE simulation is deemed sufficient at describing electric field distortions for first physics analyses at the experiment. One exception is TPC EE, which was subject to a field cage short during early ICARUS run periods and shows comparatively larger reconstructed spatial offsets. Still, this effect can be largely fiducialized away until a more detailed model of the field cage short is formed.

For a more precise treatment of electric field distortions in the next generation of ICARUS physics analyses, work is ongoing to tune existing SCE maps to better match observations from

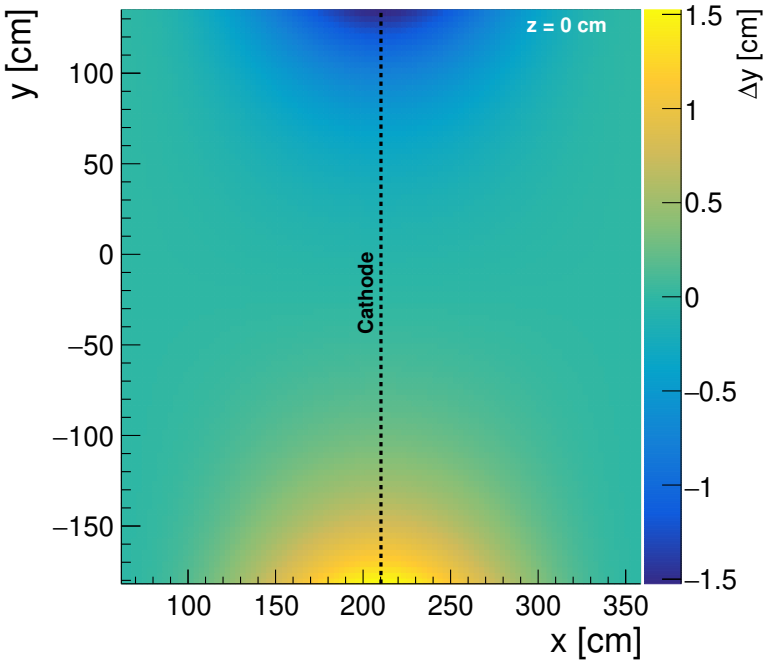

Figure 7.9: Vertical component Δy of simulated transverse spatial offsets at ICARUS for a central slice of the detector along the BNB direction ($z = 0$).

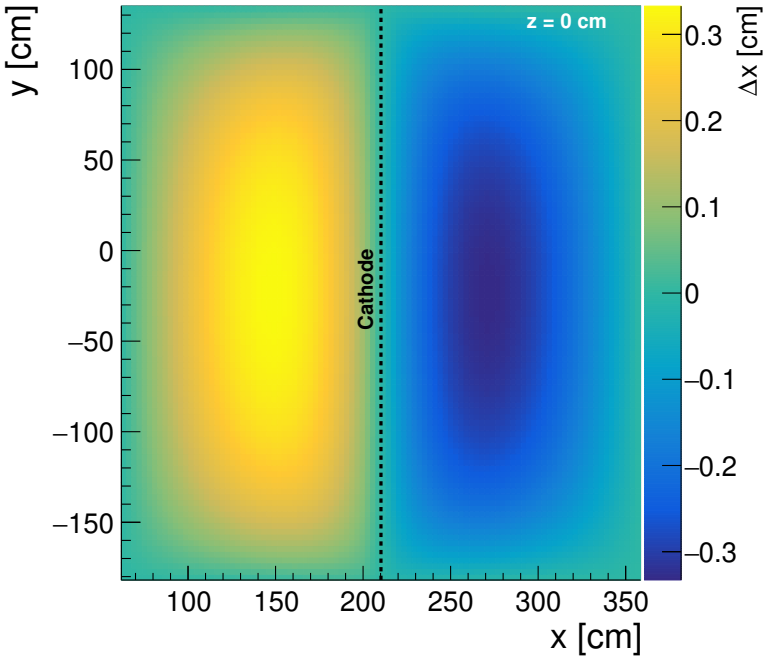

Figure 7.10: Simulated longitudinal spatial offsets Δx at ICARUS for a central slice of the detector along the BNB direction ($z = 0$).

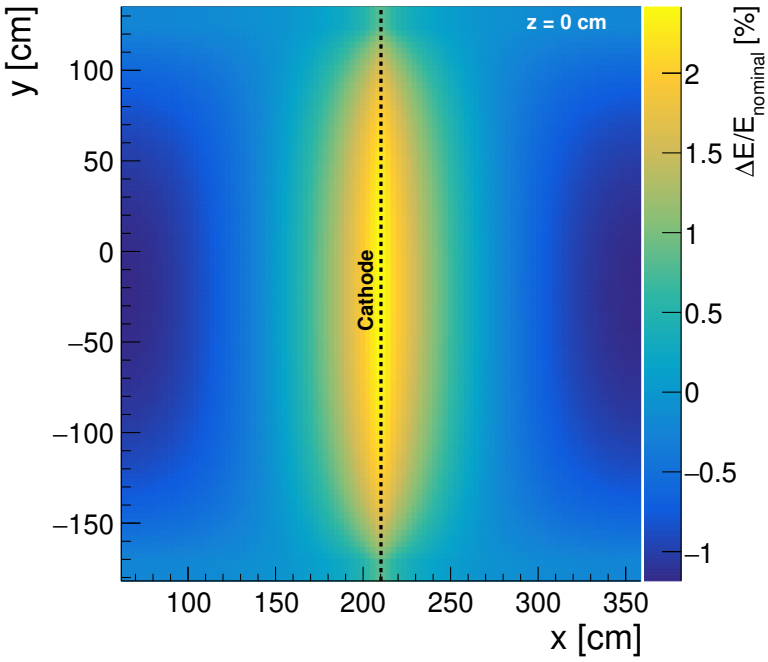

Figure 7.11: Simulated longitudinal electric field offsets ΔE relative to the nominal electric field at ICARUS for a central slice of the detector along the BNB direction ($z = 0$).

data. This procedure typically involves the calculation of scale factors, which are formed from data/MC ratios of spatial offsets in 3D bins of the detector active volume. Scale factors can be calculated using either longitudinal or transverse spatial offsets, and infrastructure has been developed at ICARUS to handle either case. In the case of longitudinal SCE, it is straightforward to repeat the same spatial offset measurements highlighted previously, but in 3D bins instead of 1D bins. The difficulty lies in gathering enough statistics for a fine-grained detector characterization in both simulation and data, though this is not expected to be an issue at this stage of ICARUS operation.

To characterize transverse spatial offsets in three dimensions, 2D spatial offset maps are first formed at each TPC face in data and Monte Carlo simulation. Dividing the data map by the simulation map produces a 2D scale factor map at each face, and linear interpolation between opposing faces yields 3D scale factors. Using the top face of the east cryostat as an example, Figure 7.12 shows the transverse spatial offset map that would be used as input to this procedure. Notably, it can be seen from this figure and Figure 7.3 that reconstructed spatial offsets do not completely vanish near the anode, contrary to expectations given the space charge density described previously. This effect likely arises from the field cage geometry at ICARUS as well as the wire plane configuration in the region near the field cage. Precise modeling of these features will be key in the assessment of SCE using the method of transverse offsets and is a priority for future studies.

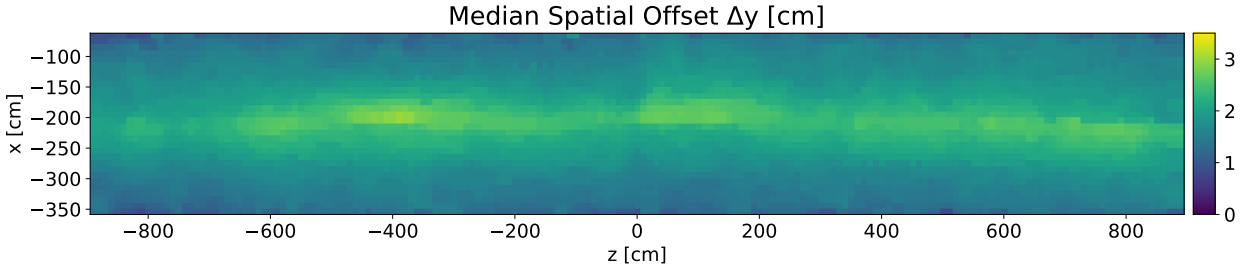

Figure 7.12: Transverse spatial offset map from Run 3 data for the top face of TPCs in the east cryostat of ICARUS. Spatial offsets are observed to be largest near the cathode, positioned at $x = -210.215$ cm on the vertical axis, as expected.

7.3 Cathode Nonplanarity

In each ICARUS TPC module, the high-voltage cathode spans the transverse dimensions of the drift volumes and is built from hole-punched stainless steel. Each cathode is comprised of nine individual panels in total, all having 1.5 mm thickness and held in place by reinforcement beams that ensure firm connection to the primary mechanical structure of the TPC module, as seen in Figure 7.13. Ideally, each panel is planar in nature as to enable a uniform electric field and efficient reconstruction of tracks crossing the cathode. In reality, the panels are not perfectly planar and deformities lead to sections of the cathode being "bent."

Figure 7.13: Inner mechanical structure of an ICARUS TPC module. Nine stainless steel panels make up the high-voltage cathode and can be seen on the right side of the image [64].

Visualization of cathode nonplanarity is straightforward and makes use of the exact same anode-cathode-crossing cosmic-ray muon selection from the longitudinal SCE study presented in Section 7.2. By identifying the space point corresponding to the maximum drift time for each of these tracks, the reconstructed position of the cathode can be mapped in all three spatial dimensions. Given anode-cathode-crossing tracks can be identified in all four TPCs, reconstructed cathode position maps can be cross-checked across the two drift volumes in a given TPC module. These maps are shown in Figure 7.14 for the case of ICARUS Run 3 data. Each map is represented by a 2D histogram where color depicts the median drift coordinate position of the cathode in the detector geometry, noting that the expected cathode position is at ± 210.215 cm.

While the maps in Figure 7.14 clearly show the extent of cathode bending at ICARUS, the ICARUS simulation chain has historically assumed the cathode to be flat. This means possible failures in track reconstruction due to the effect have not been reproducible in simulation, resulting in a bias with respect to observations from data. For this reason, the data-driven maps from Figure 7.14 have been implemented in recent versions of ICARUS simulation, effectively treating the cathode's drift-coordinate position as a function of the detector transverse coordinates. Validation of the simulated maps can be found by repeating the study used to derive the maps in data, only now using simulated anode-cathode-crossing tracks. The results of this study are shown in Figure 7.15, showing good agreement with observations from data. While this update was not made in time to be included in the Monte Carlo simulation used for predictions in the ν_μ CC π^0 analysis, work is underway to include the effect in a dedicated simulation sample for treatment as a systematic uncertainty.

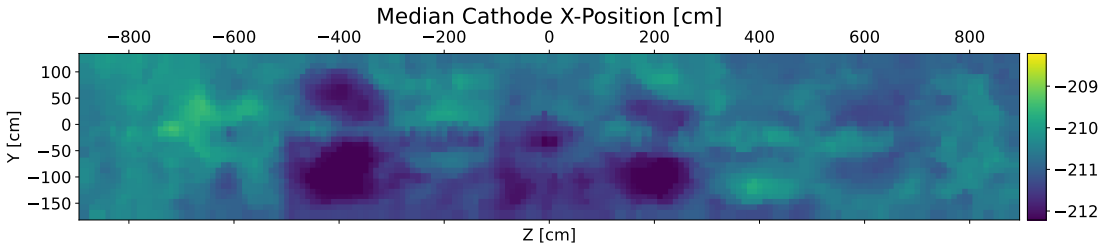

(a) TPC EE

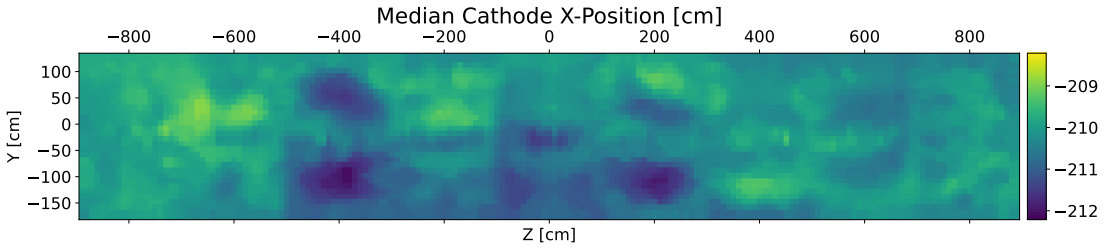

(b) TPC EW

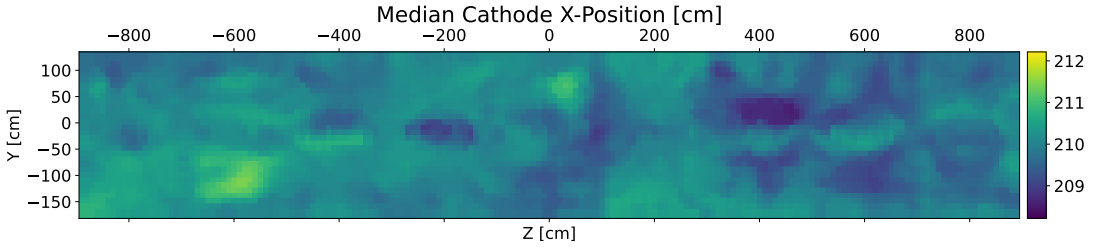

(c) TPC WE

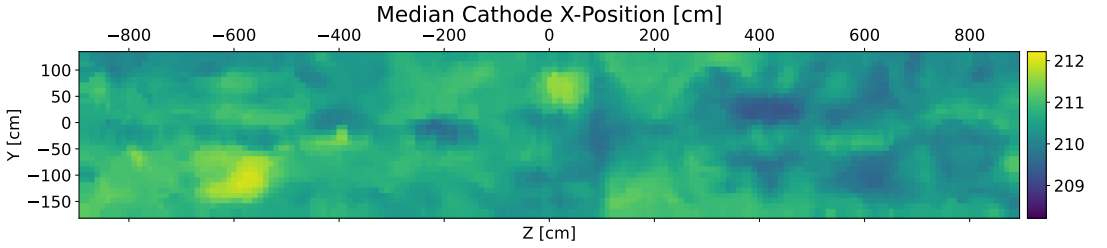

(d) TPC WW

Figure 7.14: Reconstructed cathode position maps for each ICARUS TPC, as measured with an anode-cathode-crossing cosmic-ray muon sample from ICARUS Run 3 data.

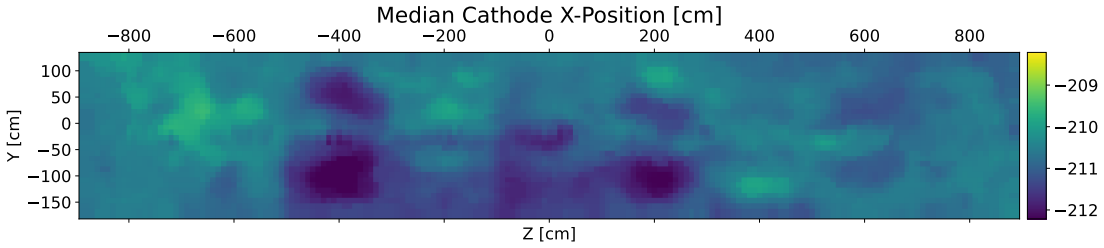

(a) TPC EE

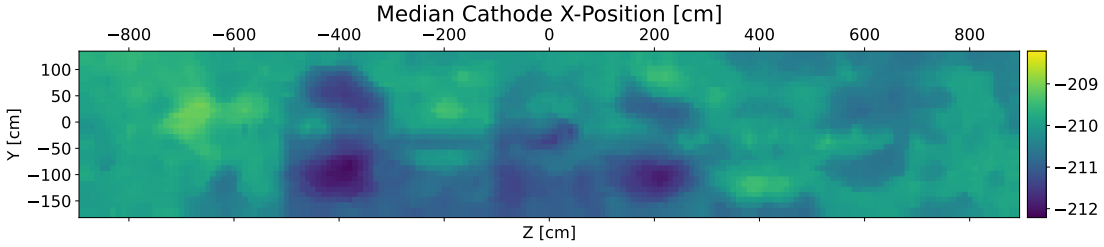

(b) TPC EW

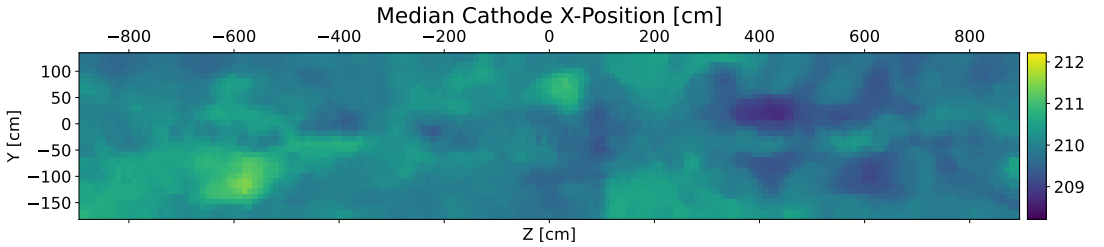

(c) TPC WE

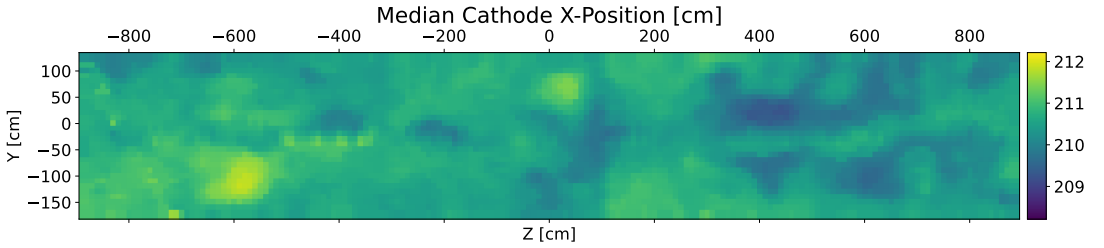

(d) TPC WW

Figure 7.15: Reconstructed cathode position maps for each ICARUS TPC, as measured with an anode-cathode-crossing cosmic-ray muon sample from a Monte Carlo simulation including BNB neutrinos and cosmic muons.

Chapter 8

ν_μ CC π^0 Selection

This chapter describes the signal definition employed in the ν_μ CC π^0 analysis and the subsequent selection of candidate signal interactions with the Booster Neutrino Beam at ICARUS. Section 8.1 provides the specifics of the signal definition, while Section 8.2 details how signal events are selected in practice. Selection performance is then analyzed in Section 8.3, followed by an introduction to numerous variables of interest in Section 8.4. To finish the chapter, Section 8.5 discusses the binning choices for cross section analysis variables.

This analysis utilizes ICARUS data collected from the BNB between Winter 2022 and Spring 2023 (Run 2). While the full run period corresponds to approximately 2×10^{20} POT, studies presented in this thesis are limited to accessing one-tenth of this dataset in accordance to the official blinding policy of the ICARUS collaboration. At the time of this writing, the ν_μ CC π^0 analysis is undergoing internal review in preparation for unblinding the full Run 2 dataset.

Monte Carlo simulation consisting of BNB neutrinos (produced with GENIE) and cosmics (produced with CORSIKA) is used to assess selection performance and evaluate systematic uncertainties. In addition to the primary Monte Carlo simulation sample used in the analysis, this includes dedicated detector variation samples used to quantify detector systematics, which are discussed in Section 9.3. To evaluate the impact from cosmic activity that occurs within the $\sim$1.6 µs BNB beam gate, off-beam data is used. All samples are processed through the complete ICARUS reconstruction chain, including both low-level hit reconstruction and the full SPINE machine learning framework. A summary of production streams used in this analysis is shown in Table 8.1.

Table 8.1: Data/simulation streams used for the ν_μ CC π^0 analysis.

Sample	Type	POT	Beam Gates
BNB Run 2 On-Beam Majority Trigger[1]	Data (on-beam)	1.97×10^{19}	5.26×10^{6}
BNB Run 2 Off-Beam Majority Trigger	Data (off-beam)	N/A	4.86×10^{7}
BNB ν + Cosmic	Simulation	1.68×10^{21}	N/A

8.1 Signal Definition

As discussed in Chapter 1, ν_μ CC π^0 interactions with argon are muon-neutrino-induced events resulting in the production of a single muon and a single neutral pion in the final state. Besides charged pions, which are excluded to limit the selection of coherent pion production events, the signal definition is inclusive to all other particles. Expanding on Equation 1.1, the precise signal definition used in this analysis involves neutrino interactions within the ICARUS fiducial volume that result in the following final-state particles:

- Exactly one primary muon (length ≥ 50 cm).
- Zero primary charged pions.
- Exactly one primary neutral pion.
- Any number of particles that are not muons or pions.

The fiducial volume requirement applies to the neutrino interaction vertex, which must be 25 cm from detector boundaries in the drift and vertical directions, 30 cm from the upstream detector face, and 50 cm from the downstream face. This requirement helps separate neutrino interactions from cosmic-ray muon events, as well as ensure photon daughters from neutral pion decays deposit most of their energy inside the TPC. Additionally, the interaction vertex is required to lie outside of the region defining the central 200 cm of the detector in the beam direction. This requirement is made in an effort to avoid potential discrepancies between data and simulation related to the geometry of each TPC's first induction plane. Two sets of horizontal wires make up this plane, with each set attached to a vertical support structure in a configuration that has been seen to introduce event reconstruction inefficiencies. The 50 cm muon length requirement corresponds to a kinetic energy of approximately 143 MeV and is in place to minimize contamination from neutral current events containing charged pions.

[1] 10% of the full BNB Run 2 dataset is currently accessed in this analysis.

8.2 Selection Criteria

The procedure for identifying candidate ν_μ CC π^0 interactions involves four distinct stages:

1. Requirements are placed on the quality of neutrino beam spills and data collected.

2. An initial selection is made to reduce contamination from cosmic-ray muons and identify interactions that are topologically similar to the signal definition.

3. The invariant diphoton mass distribution of reconstructed signal candidates is used to inform the electromagnetic shower energy scale in an otherwise identical second selection stage.

4. After the shower energy scale has been adjusted, the resultant invariant diphoton mass distribution is again examined and used as a means to apply selection cuts to further reduce backgrounds.

Data and Beam Quality Requirements

To ensure physics quality data, DAQ runs used in this analysis have been pre-filtered based on a number of conditions. These include basic DAQ functionality, the presence of all detector readout components (TPC, PMT, and CRT) in the recorded data stream, and a run duration of at least one hour. Checks were also placed on wire bias and cathode voltages to ensure values were within nominal ranges. Additionally, reconstruction metrics such as the average number of hits on a given wire plane in the event and the total number of photoelectrons per optical flash were calculated for each run and compared to the global mean of all runs, with runs rejected if they showed more than a 3σ difference with respect to the average value across the entire data-taking period.

For identification of physics quality beam spills within a data collection run, requirements are placed on BNB intensity, focusing horn current, and overlap with the nuclear target. Beam intensity requirements aim to ensure ICARUS receives a non-zero POT and are enforced conservatively on toroid devices and loss monitors in the beamline. Requirements on the focusing horn current remove spills in which the horn current differs beyond 2 kA from its nominal Run 2 setting of 174 kA. Beam overlap with the nuclear target is assessed through information associated with the

beam position and width at the target location on a spill-by-spill basis, with requirements on these quantities placed to ensure sufficient overlap.

The data and beam quality requirements described here are identical to those used in other BNB analyses at ICARUS [65], and their impact is seen as a reduction in the nominal exposure values (POT and number of beam gates) for Run 2. After these requirements are enforced, the unblinded 10% of BNB Run 2 data used in this analysis corresponds to 1.62×10^{19} POT and 4.07×10^{6} beam gates.

Initial Selection

To narrow the list of signal candidates, the following selection cuts are initially applied:

- Fiducial volume: The reconstructed neutrino interaction vertex is required to be inside the fiducial volume (matching the signal definition). The neutrino interaction vertex is reconstructed downstream of the SPINE machine-learning chain as part of a post-processor, as discussed in Section 6.3.2.
- Flash time: The reconstructed interaction is required to be associated with an optical flash that is in-time with the 1.6 µs BNB beam gate. Matching between interactions and optical flashes occurs downstream of the SPINE machine-learning chain as part of a post-processor.
- Topology: The reconstructed interaction includes the following:
  - Exactly one primary muon (length $\geq$ 50 cm).
  - Zero additional primary muons (kinetic energy $\geq$ 25 MeV).
  - Zero primary charged pions (kinetic energy $\geq$ 25 MeV).
  - Exactly two primary photons (kinetic energy $\geq$ 25 MeV).

Graph neural networks described in Section 6.3.2 are responsible for the grouping of particles by interaction, the primary classification of particles, and particle identification. The length requirement of the muon follows the signal definition, while the energy requirements associated with photons and charged pions are thresholds placed to ensure efficient reconstruction.

With these cuts applied, the reconstructed neutral pion mass is then examined. Conservation of energy and momentum in the neutral pion's decay to two photons gives the invariant mass $m_{\gamma\gamma}$ as

$$m_{\gamma\gamma} = \sqrt{2E_1E_2(1-\cos\theta)}, \tag{8.1}$$

where E_1 and E_2 are reconstructed energies of the selected photon candidates and θ is the reconstructed diphoton opening angle. Photon energies are estimated according to Equation 6.5, while the diphoton opening angle calculation leverages reconstructed quantities for the neutrino interaction vertex and shower start points.

The distribution yielded by Equation 8.1 for all selected candidate interactions is shown in Figure 8.1. As systematic uncertainties are not introduced until Chapter 9, selected counts in data and simulation are normalized to unity. Stacked histograms show the true topology of the selected interactions, with the green "$1\mu^-0\pi^\pm1\pi^0$" category representing fiducial ν_μ CC π^0 events with final-state particles meeting the energy threshold requirements of the signal definition. True ν_μ CC π^0 events where the neutrino interaction vertex falls outside of the fiducial volume, or any final-state particles do not meet the energy threshold requirements of the signal definition, are

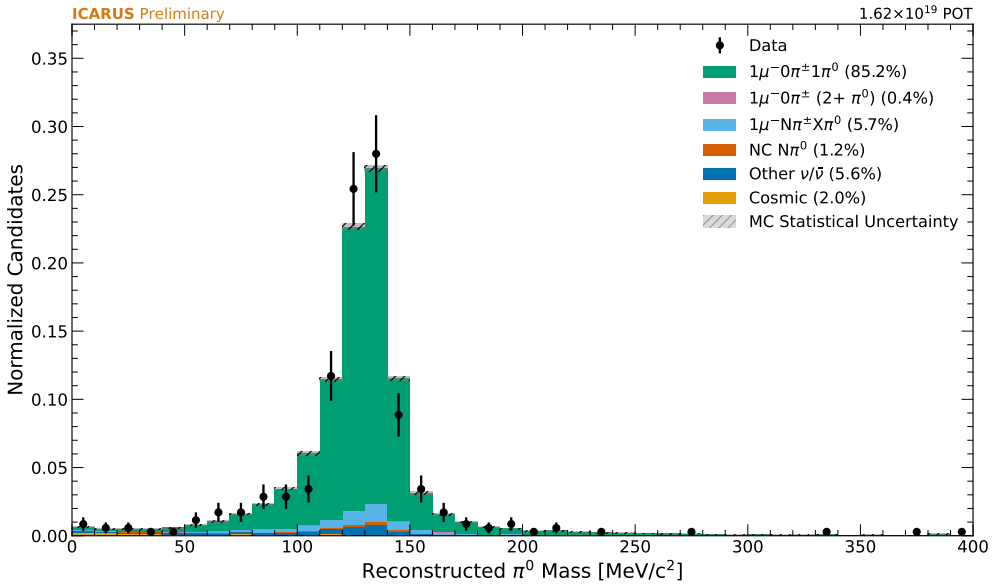

Figure 8.1: Reconstructed neutral pion invariant mass after initial selection criteria are applied. Black scatter points correspond to the unblinded 10% of ICARUS BNB Run 2 data.

categorized as "Other ν" (dark blue). This category also includes interactions where a secondary neutral pion is produced.

Electromagnetic Shower Energy Scale Adjustment

As bias between the location of the reconstructed neutral pion mass peak and true neutral pion mass ($\sim$135 MeV/c^2) is driven by reconstructed shower energy, the reconstructed distribution can be used to inform the shower energy scale in the next selection stage. For this, double-sided Crystal Ball fits (as described in Section 6.3.3) are applied to the reconstructed neutral pion mass distributions in both data and simulation. The ratio of the Gaussian mean from each fit and true neutral pion mass forms a multiplicative correction factor that can be used to adjust reconstructed shower energies. Figure 8.2 shows the reconstructed neutral pion mass before and after this adjustment is made, with the latter showing better agreement with the true neutral pion mass.

Cuts on Reconstructed Invariant Diphoton Mass

Further highlighting the utility of the reconstructed neutral pion mass distribution, the impacts of applying cuts based on this distribution are shown in Figure 8.3. Compared to previous figures, the horizontal axis range is extended to show an uptick in selected events at approximately 550 MeV/c^2 due to the presence of η mesons. This region is easily avoided with a cut on invariant diphoton mass at 300 MeV/c^2. Additionally, interactions with reconstructed invariant mass below 60 MeV/c^2 are excluded due to a relatively high fraction of these originating from cosmic-ray muons.

8.3 Selection Performance

Selection performance is assessed using the BNB ν + Cosmic Monte Carlo simulation sample and off-beam BNB Run 2 data. The metrics that have been evaluated are efficiency — the fraction of true signal interactions that are matched to selected interactions, and purity — the fraction of selected interactions that are matched to true signal interactions. Cumulative values for efficiency

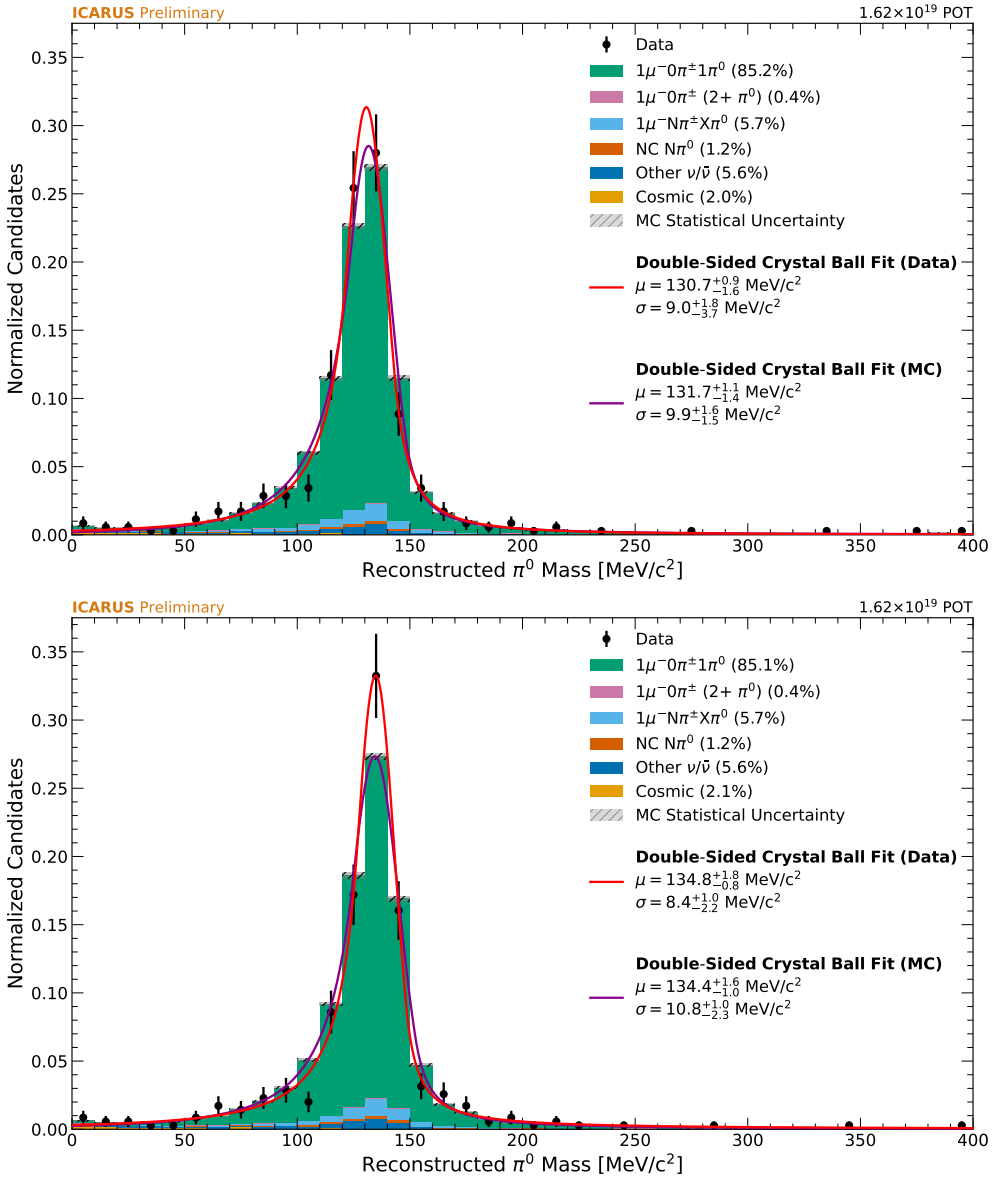

Figure 8.2: Crystal Ball fits to reconstructed neutral pion mass before (top) and after (bottom) fit parameters are used to adjust the shower energy scale. The mean and standard deviation of the fit's Gaussian component is included in the plot legend.

and purity for each selection cut are shown in Table 8.2, with the final values for each metric reported in bold at the bottom of the table.

For fiducial interactions that are in-time with the BNB, selection inefficiencies and impurities are driven by particle identification failures. In the confusion matrix shown in Figure 8.4a, true signal ν_μ CC π^0 interactions are isolated and the true particles they contain are compared against

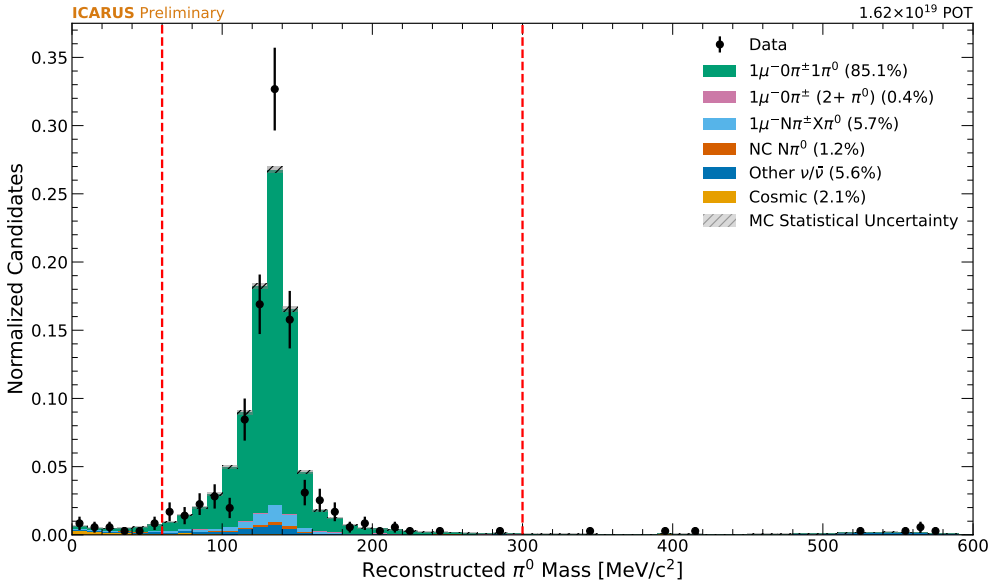

Figure 8.3: Reconstructed neutral pion invariant mass after initial selection and adjustment to electromagnetic shower energy scale. Only the part of the distribution between the two red dashed lines is kept in the final selection.

their matched reconstructed counterparts. Inefficiencies are highlighted by off-diagonal elements of the matrix, led by the misidentification of true protons as muons or charged pions. Conversely, Figure 8.4b shows matched truth information for reconstructed particles from candidate ν_μ CC π^0 interactions remaining after selection cuts are applied. The leading source of residual impurities is the misidentification of true charged pions as protons.

Table 8.2: Cumulative efficiency and purity values on a cut-by-cut basis for the ν_μ CC π^0 selection. For cuts involving the interaction topology, "KE" refers to the kinetic energy of the involved particles.

Selection Cut	Efficiency [%]	Purity [%]
No Cut	100.0	0.0
In-Time Flash	97.1	0.5
Fiducial Volume	96.5	2.9
Single Muon (length $\geq$ 50 cm)	90.6	3.8
Two Photons (KE $\geq$ 25 MeV)	74.2	68.3
No Charged Pions (KE $\geq$ 25 MeV)	69.2	84.3
No Second Muon (KE $\geq$ 25 MeV)	67.6	85.1
$m_{\gamma\gamma} \in [60, 300]$ MeV/c^2	**66.1**	**88.8**

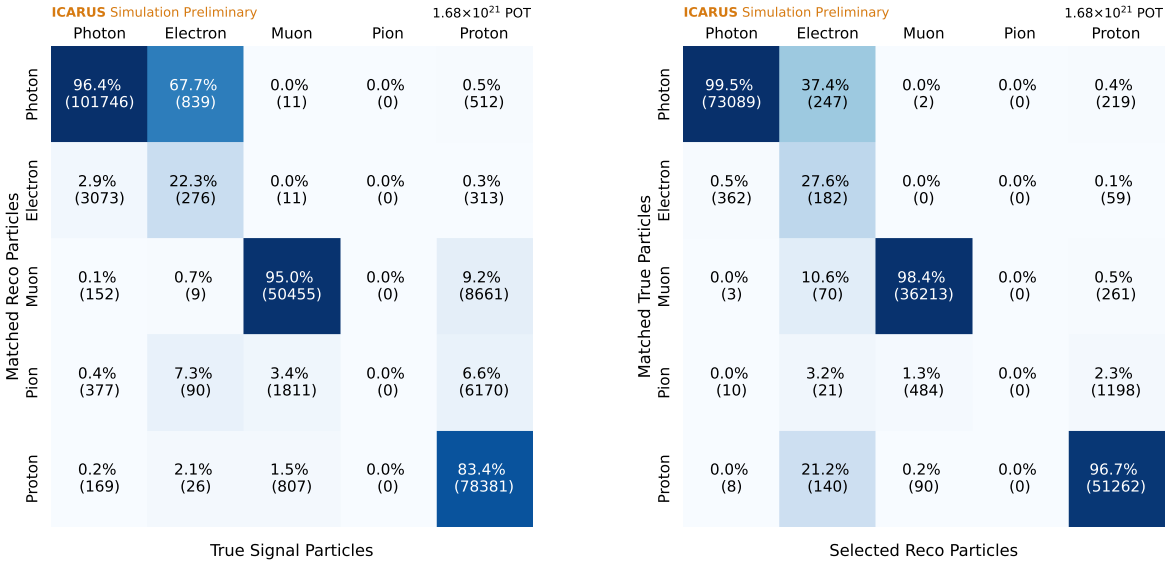

(a) Signal ν_μ CC π^0 Interactions

(b) Selected ν_μ CC π^0 Interactions

Figure 8.4: Confusion matrices for ν_μ CC π^0 selection. Truth-to-reco matching is shown on the left for true signal interactions, while reco-to-truth matching is shown on the right for interactions remaining after the application of selection cuts.

8.4 Reconstructed Observables

In this section, reconstructed observables relevant to the analysis are highlighted. Only the BNB ν + Cosmic Monte Carlo simulation and BNB Run 2 off-beam data samples are utilized here, while comparisons with on-beam data are reserved for Section 9.5 after systematic uncertainties are introduced. All distributions are normalized to unity and are formed after all selection cuts are applied, unless otherwise specified. For organizational purposes, observables have been separated into the following cateogories:

- Low-level observables used to assess basic reconstuction performance and data/simulation agreement.
- Transverse kinematic imbalance (TKI) observables that are sensitive to nuclear effects like final-state interactions (FSI).
- Observables related to the energy transfer from the neutrino to the target argon nucleon.

- Neutral pion mass observables relevant to the calibration of electromagnetic showers.
- Physics observables used to parameterize the final extracted cross section.

Low-Level Observables

One-dimensional distributions for the individual components of the reconstructed neutrino interaction vertex are shown in Figures 8.6-8.8 and employ the same signal and background categorization scheme as described in Section 8.2. As these quantities are sensitive to detector features such as electric field nonuniformities and dead wire readout regions, their visual inspection provides confirmation that the spatial distribution of selected events is within expectation.

Other low-level variables examined include the length of the selected muon, shown in Figure 8.9, and the conversion distance of each candidate π^0 daughter photon, shown in Figure 8.10. The latter quantity is is calculated as the distance between the reconstructed interaction vertex and reconstructed photon start point. Together, these distributions provide basic checks of track and shower reconstruction performance before variables with more complexity are examined.

Transverse Kinematic Imbalance Observables

TKI variables are commonly studied in cross section analyses given their sensitivity to nuclear effects like FSI. The following TKI observables are examined:

δp_T: Transverse momentum imbalance, or the magnitude of the vector difference between the transverse momentum of the muon and the hadronic system.

$\delta \alpha_T$: Transverse boosting angle, or the angle between the transverse momentum imbalance vector and the negative transverse momentum of the muon.

Figure 8.11 shows reconstructed distributions for δp_T and $\delta \alpha_T$. These quantities are depicted schematically in Figure 8.5, where z is the BNB direction and $x - y$ coordinates define the plane transverse to the BNB direction. The transverse component of the momentum transfer to the nucleus is denoted by $\vec{q}_{\mathrm{T}}$, which is equal and opposite to the muon transverse momentum. The transverse momentum of the combined hadronic system is denoted by $\vec{p}_{\mathrm{T}}^{\,\mathrm{h}}$.

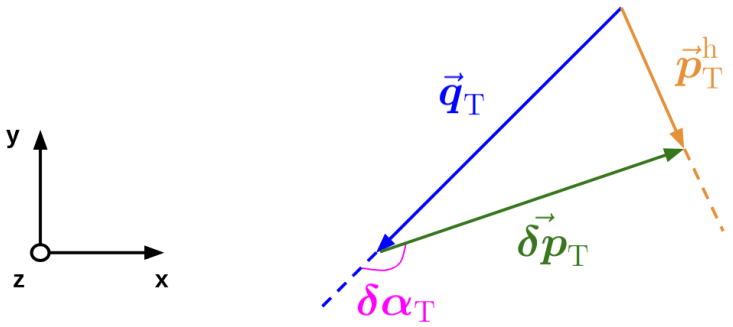

Figure 8.5: Schematic depiction of TKI observables chosen for the ν_μ CC π^0 analysis. Figure style and variable definitions follow from Ref. [66].

Visible Energy, Four-Momentum Transfer, and Hadronic Invariant Mass

Regimes of neutrino-nucleon scattering are distinguished by the energy of the incident neutrino, the four-momentum transferred from the neutrino to the target nucleon and the invariant mass of the resultant hadronic system of the interaction. For this reason, the following observables are examined:

E_{vis}: Visible energy of all primary particles produced in the ν-Ar interaction. This variable is calculated with the sum $E_{\mathrm{vis}} = E_\mu + \sum E_{\mathrm{shower}} + \sum T_p$, where E_μ is the total muon energy, E_{shower} is the energy of a primary shower, and T_p is the kinetic energy of any given proton present in the interaction after subtracting the nucleon binding energy (taken from GENIE simulation as 30.9 MeV).

Q^2: Squared four-momentum transfer to the target nucleon. This variable is calculated using reconstructed quantities for the visible energy of the interaction E_{vis} (described above), the total muon energy E_μ, the muon momentum p_μ, and the muon angle relative to the BNB direction θ_μ as $Q^2 = 2E_{\mathrm{vis}}(E_\mu - p_\mu \cos\theta_\mu) - m_\mu^2$.

W: Hadronic invariant mass of the final state. This variable is calculated using reconstructed quantities for E_{vis}, E_μ, and Q^2 (all described above) as $W = \sqrt{m_N^2 + 2m_N(E_{\mathrm{vis}} - E_\mu) - Q^2}$, where m_N is the mass of the struck nucleon.

Figure 8.12 shows the reconstructed visible energy distribution, while Figure 8.13 shows reconstructed distributions for Q^2 and W.

Neutral Pion Mass Observables

Variables that inform the invariant mass expression in Equation 8.1 are shown in Figure 8.14 and Figure 8.15, followed by the mass distribution itself in Figure 8.16.

Cross Section Analysis Observables

In this analysis, differential cross sections are extracted as a function of particle momentum and angle relative to the neutrino beam for both the muon and neutral pion present in the interaction. Regarding the muon observables, cross section measurements involving these variables are common given the precision with which they can be measured as well as their relevance in neutrino oscillation physics measurements. With use of reconstructed photon kinematics, the same variables are straightforward to measure for the neutral pion. Together, these measurements offer a probe of regions that have been historically difficult to model with generators, such as at forward scattering angles.

The momentum of the candidate muon in the interaction is reconstructed from the particle's kinetic energy, which is estimated with a range-based approach if the particle is contained within the active liquid argon volume and through measured deflection angles associated with multiple Coulomb scattering if the particle exits the active liquid argon volume without ranging out. The cosine of the muon angle relative to the BNB direction is then calculated as the scalar product between the muon momentum and beam direction vectors. Reconstructed distributions for the muon momentum and angle relative to the BNB direction are shown in Figure 8.17.

Both the neutral pion momentum and angle relative to the neutrino beam are inferred from reconstructed photon kinematics. The neutral pion momentum is calculated as the vector sum of photon momenta, with each photon momentum being calculated using the photon's calorimetric kinetic energy measurement and the direction vector formed using the interaction vertex and shower start point. As was the case with the candidate muon, the cosine of the neutral pion angle

relative to the BNB direction is calculated as the scalar product between the neutral pion momentum and beam direction vectors. Reconstructed distributions for the neutral pion momentum and angle relative to the BNB direction are shown in Figure 8.18.

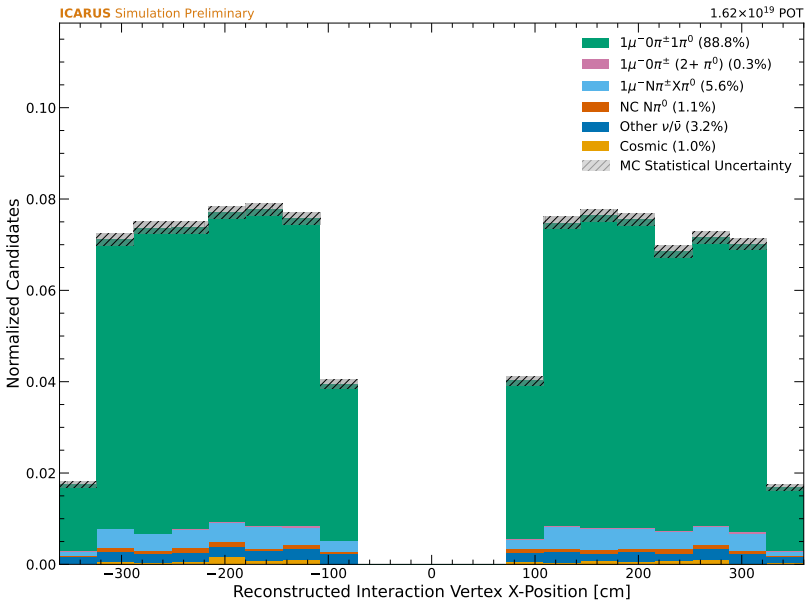

Figure 8.6: Reconstructed neutrino vertex x component for selected ν_μ CC π^0 interactions in simulation.

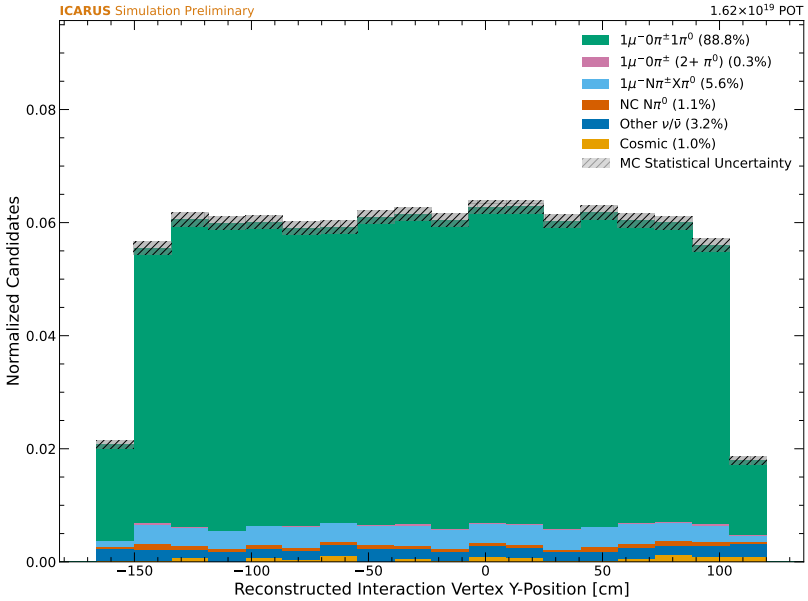

Figure 8.7: Reconstructed neutrino vertex y component for selected ν_μ CC π^0 interactions in simulation.

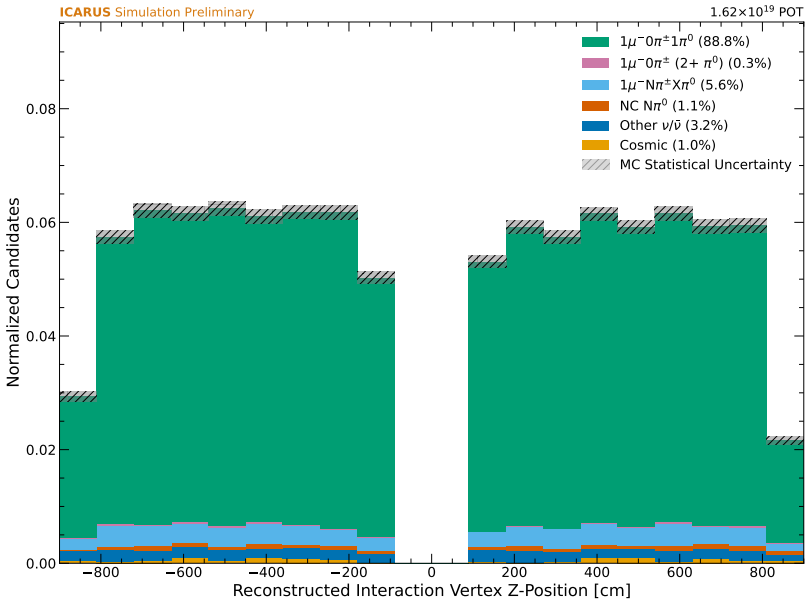

Figure 8.8: Reconstructed neutrino vertex z component for selected ν_μ CC π^0 interactions in simulation.

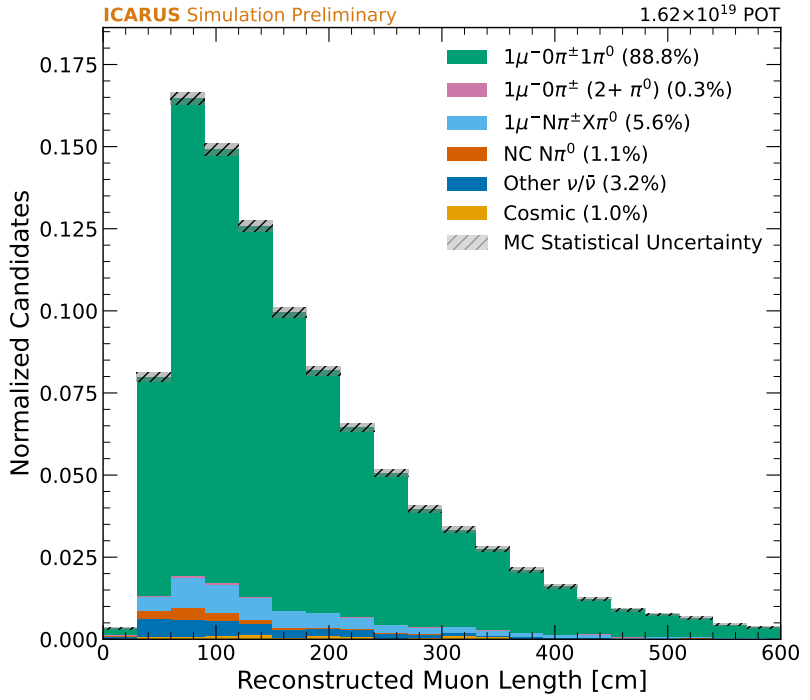

Figure 8.9: Reconstructed muon length for selected ν_μ CC π^0 interactions in simulation.

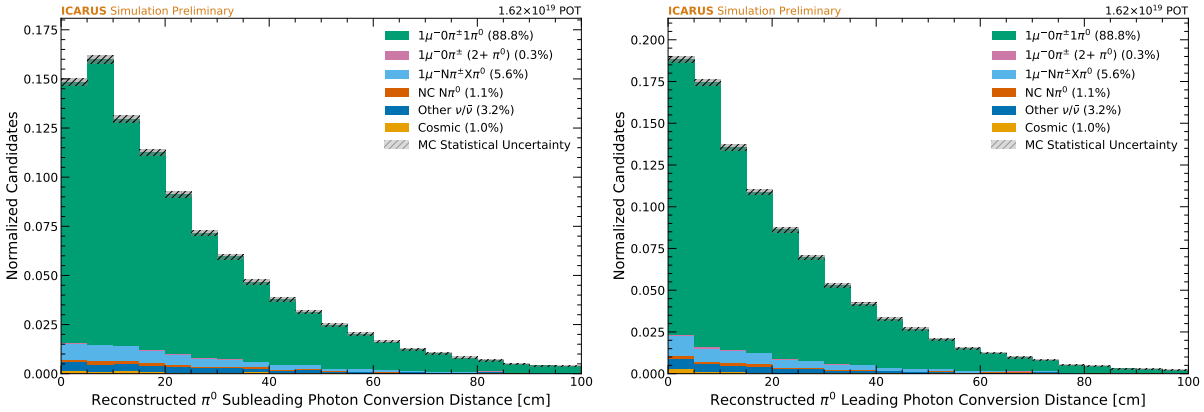

Figure 8.10: Reconstructed subleading (left) and leading (right) photon conversion distances for selected ν_μ CC π^0 interactions in simulation.

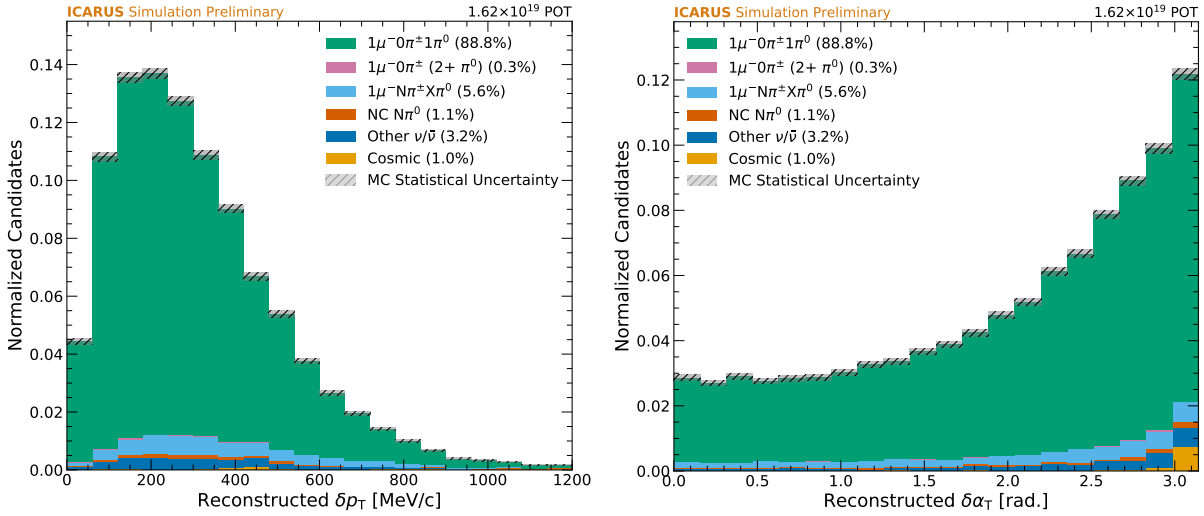

Figure 8.11: Reconstructed transverse momentum imbalance (left) and boosting angle (right) for selected ν_μ CC π^0 interactions in simulation.

8.5 Binning for Cross Section Measurement

A suitable binning scheme is important to any binned cross section analysis, and the binning chosen for the muon and neutral pion kinematic observables is driven by a combination of factors. In the distributions from Section 8.4, binning occurs in *reconstructed* space, where the priority is to display key features of the distribution while maintaining high statistical precision in each bin. Reconstructed bins were chosen such that selected event counts in simulation and data total to at least ten per bin, with the comparatively smaller size of the unblinded Run 2 on-beam dataset being the limiting factor.

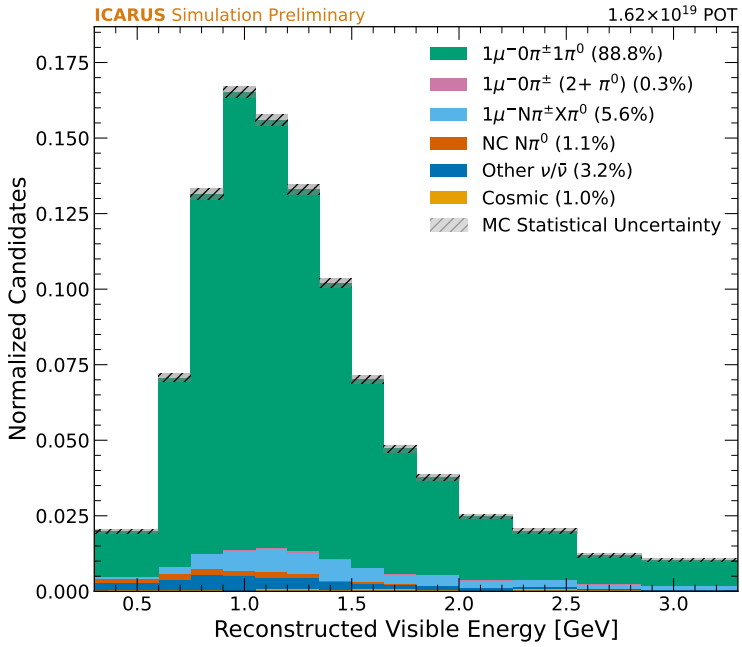

Figure 8.12: Reconstructed visible energy for selected ν_μ CC π^0 interactions in simulation.

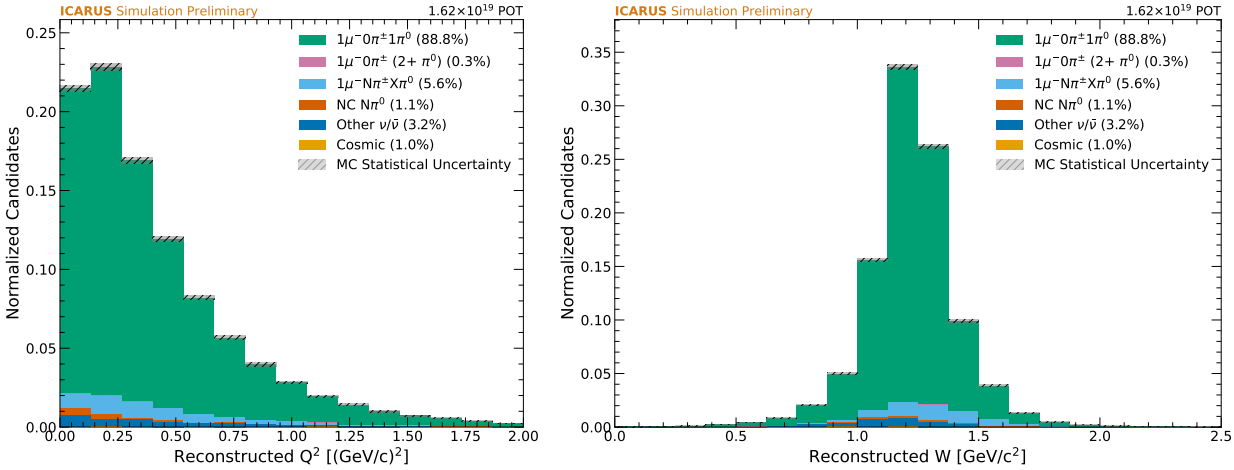

Figure 8.13: Reconstructed squared four-momentum transfer (left) and hadronic invariant mass (right) for selected ν_μ CC π^0 interactions in simulation.

The reconstructed binning is not required to be equivalent to that used for reporting the differential cross section, which will now be referred to as the *true* binning. In fact, it is common practice in binned-likelihood analyses to use finer binning in reconstructed space, as this provides cross section fitting algorithms more detailed information about smearing caused by the limited energy resolution of the detector. Two reconstructed bins are used for every one true bin in this

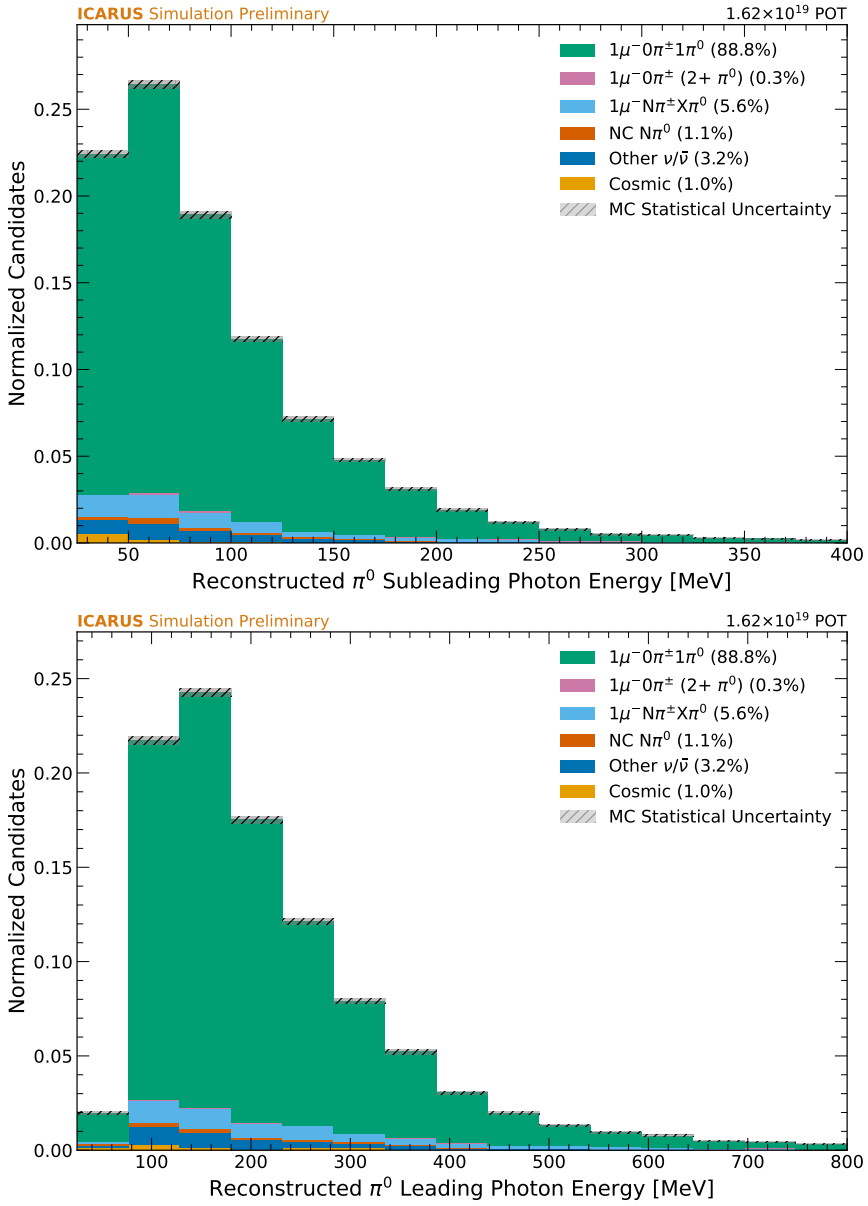

Figure 8.14: Reconstructed subleading (top) and leading (bottom) photon energies for selected ν_μ CC π^0 interactions in simulation.

analysis, which can be seen in the true-to-reconstructed bin mappings for muon (neutral pion) observables in Figure 8.19 (Figure 8.20). These mappings are sometimes referred to as "smearing matrices", as they highlight the migration of events in a given true bin (represented by a matrix column) to reconstructed bins (represented by matrix rows). It is desirable for the majority of events in a true bin to lie in its corresponding reconstructed bin(s), as this minimizes dependence on the underlying neutrino event generator to predict which true bin a reconstructed event belongs to (See

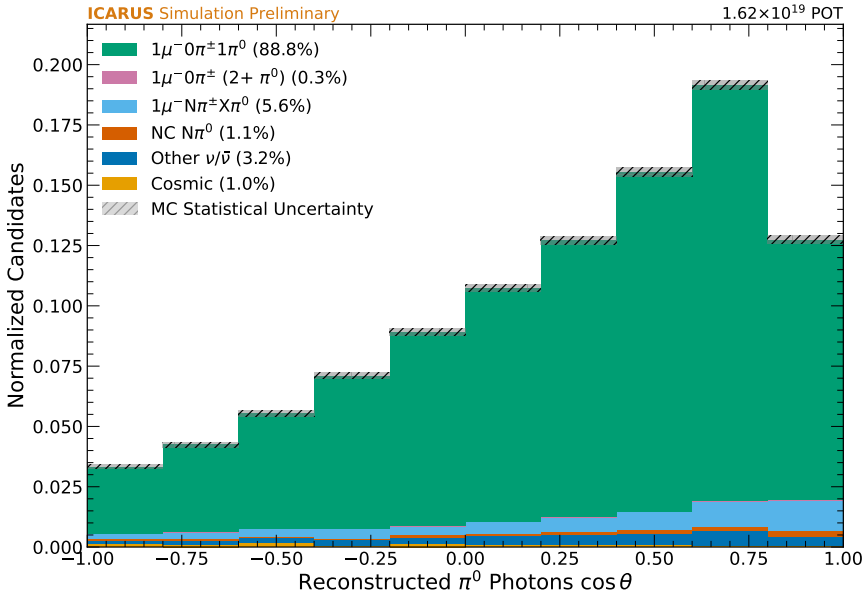

Figure 8.15: Reconstructed π^0 $\cos\theta_{\gamma\gamma}$ for selected ν_μ CC π^0 interactions in simulation.

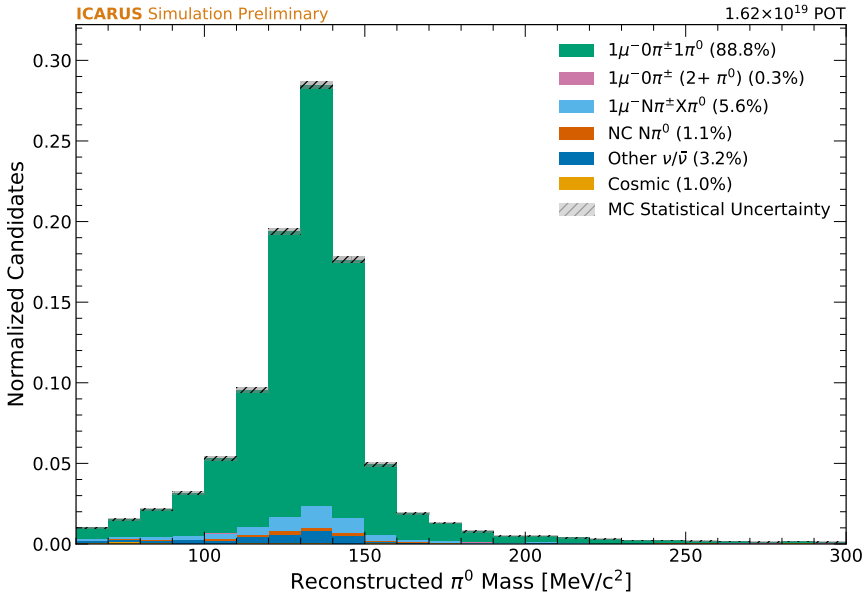

Figure 8.16: Reconstructed neutral pion mass for selected ν_μ CC π^0 interactions in simulation. The horizontal axis is restricted to the the region that satisfies the final set of selection cuts in the analysis.

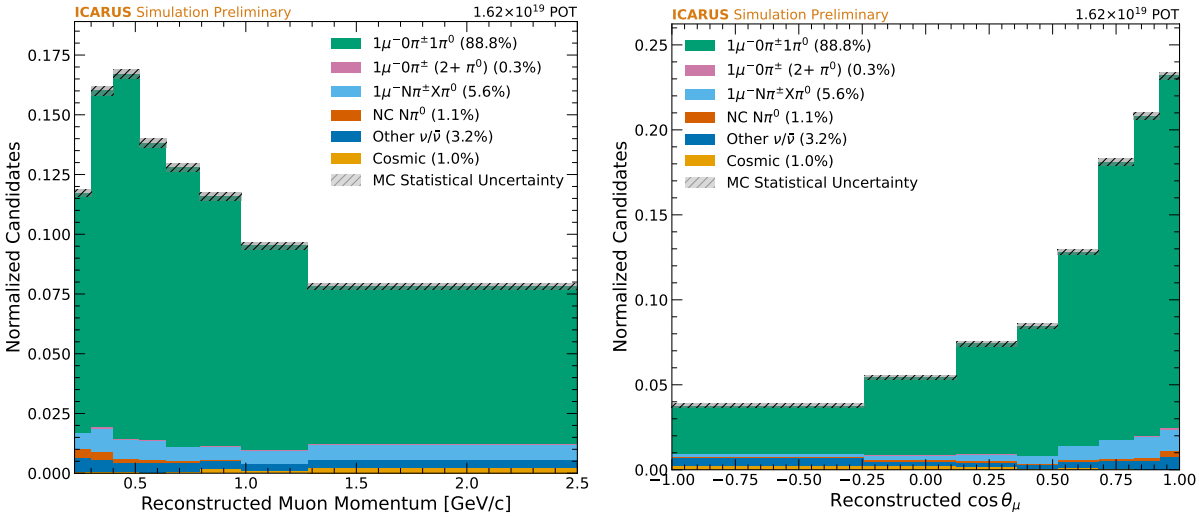

Figure 8.17: Reconstructed muon momentum (left) and angle with respect to the BNB direction (right) for selected ν_μ CC π^0 interactions in simulation.

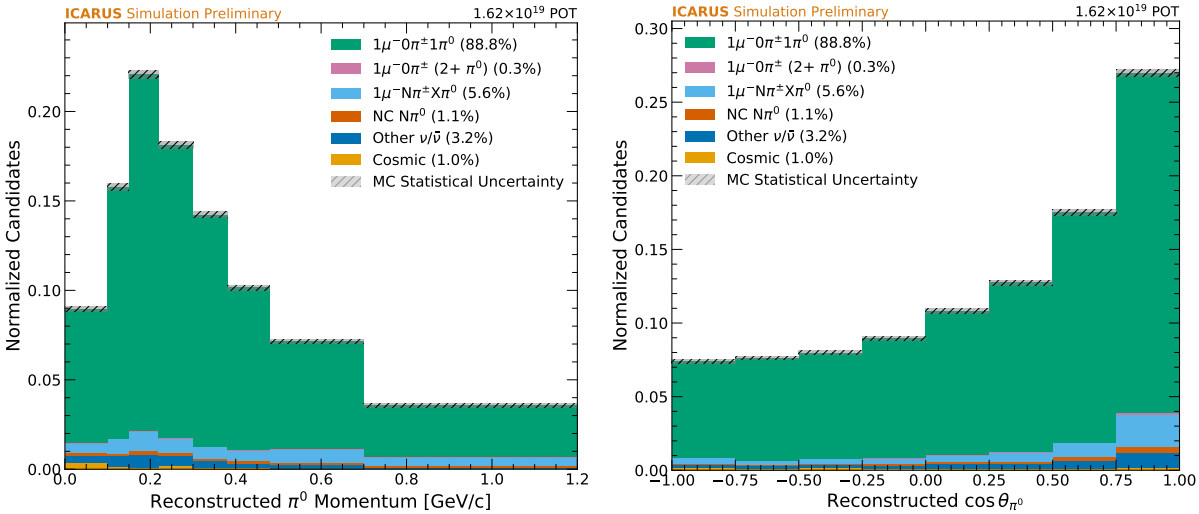

Figure 8.18: Reconstructed neutral pion momentum (left) and angle with respect to the BNB direction (right) for selected ν_μ CC π^0 interactions in simulation.

Section 10.1 for the cross section extraction procedure employed in this analysis). This is the case for each cross section analysis variable examined in this thesis, as can be seen by the vast majority of events being found along the block-diagonal structure of the smearing matrices ($>$75% of true bin events are found in corresponding pairs of reconstructed bins).

A final consideration in the choice of true binning is related to the selection efficiency of signal events. Cross section measurements rely on bin-dependent efficiency corrections to account for the loss of signal events, so it is important to understand how selection efficiency varies as a function of the involved kinematic observables. Selection efficiency is shown for muon (neutral pion) analysis variables in Figure 8.21 (8.22), along with the underlying true signal distribution. In each case, the efficiency curves show no sharp jumps and a relatively flat efficiency is observed across the majority of analysis bins. The largest variations across any bin width, such as the one seen at low muon momentum, are expected to be alleviated upon application of a finer binning scheme when a larger amount of on-beam data is processed.

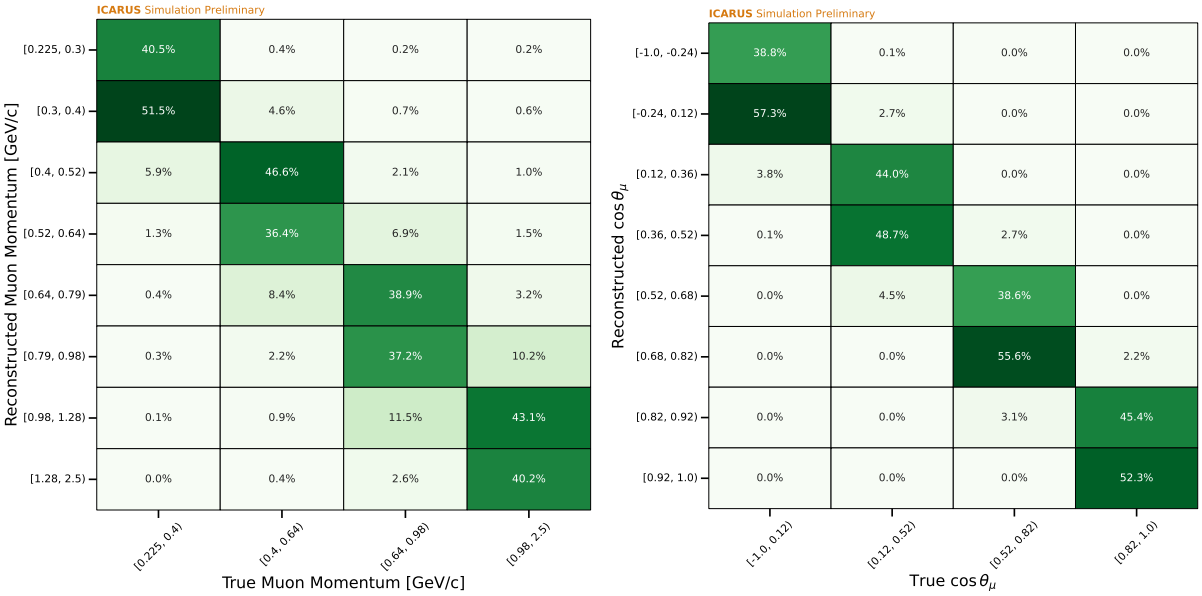

Figure 8.19: Column-normalized smearing matrices for muon momentum (left) and angle with respect to the BNB direction (right). True bins form the horizontal axis while reconstructed bins form the vertical axis.

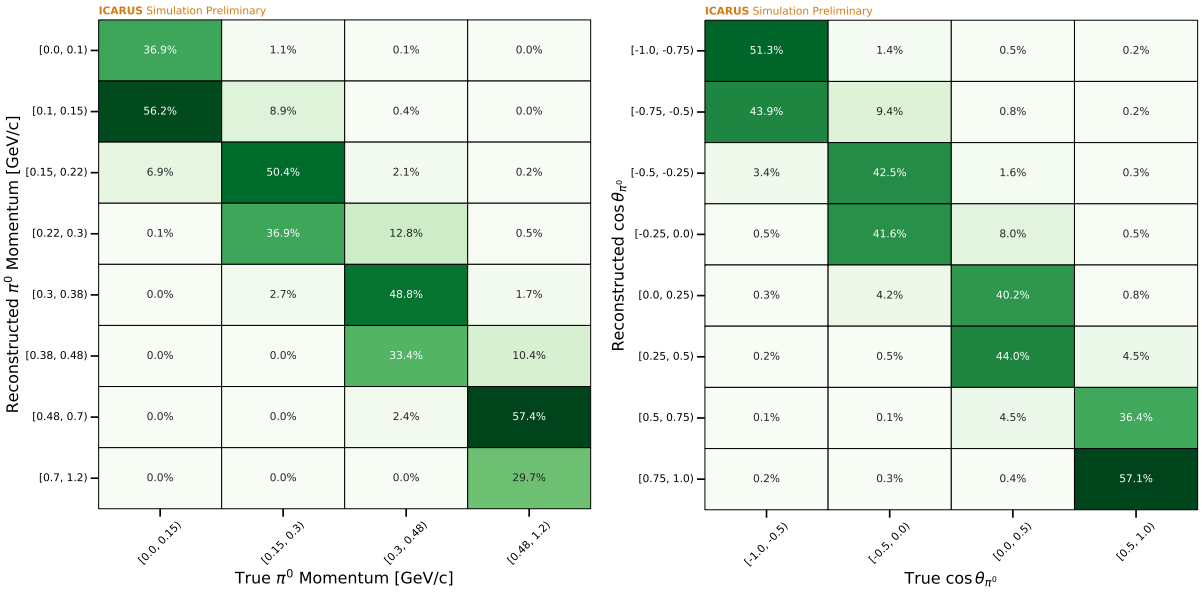

Figure 8.20: Column-normalized smearing matrices for neutral pion momentum (left) and angle with respect to the BNB direction (right). True bins form the horizontal axis while reconstructed bins form the vertical axis.

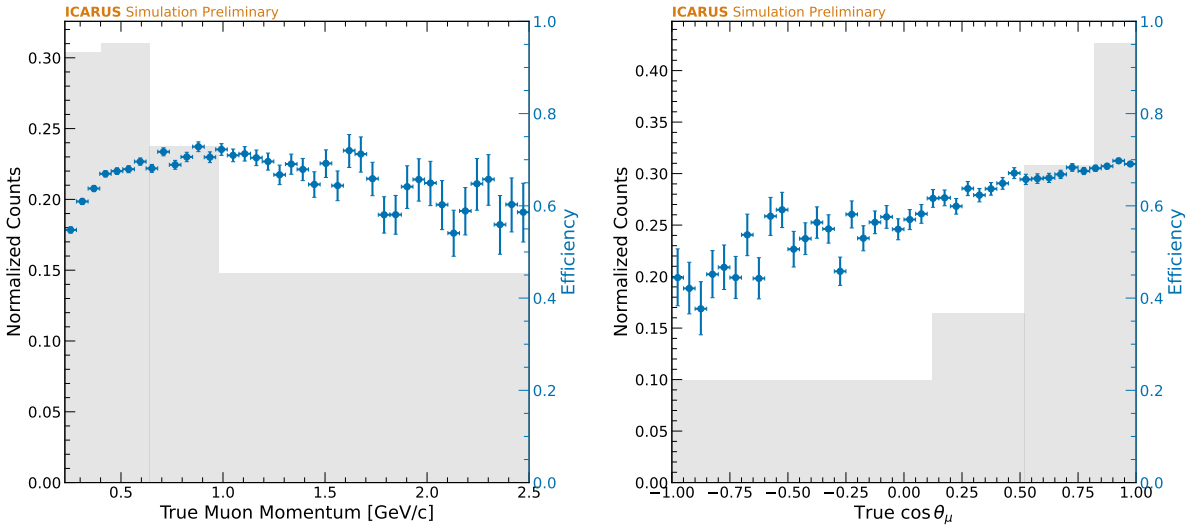

Figure 8.21: Selection efficiency as a function of muon momentum (left) and angle relative to the neutrino beam (right).

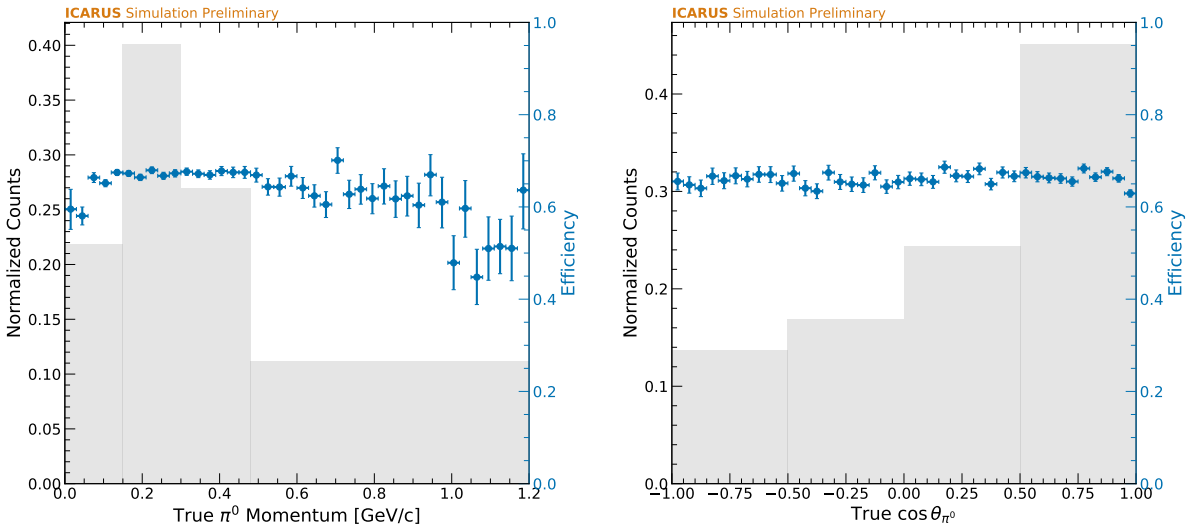

Figure 8.22: Selection efficiency as a function neutral pion momentum (left) and angle relative to the neutrino beam (right).

Chapter 9

Systematic Uncertainties and Data/Simulation Comparisons

Before comparisons of reconstructed distributions can be made between data and simulation, it is first necessary to assess systematic uncertainties that impact predictions in simulation. Within the SBN Program, these uncertainties primarily arise due to imperfect modeling of the neutrino beam, neutrino interactions with argon nuclei, and the detector response. In this chapter, each source is discussed in detail, along with the methods employed to determine their impact. The chapter concludes with comparisons of BNB Run 2 data to the nominal ICARUS simulation, folding in systematic uncertainties on the simulation and highlighting the same reconstructed distributions shown in the previous chapter.

9.1 Flux Uncertainties

The simulated BNB flux at ICARUS is based on predictions from the MiniBooNE collaboration, which used the GEANT4 tool kit to model the propagation of particles produced in proton collisions with the beam target. Uncertainties in the flux model include those related to:

- The primary production of pions and kaons at the beam target.
- The distribution and calibration of electric current in the focusing horn system.
- Secondary interactions of hadrons with beamline materials.

These sources of systematic error are defined by numerous parameters, each having their own uncertainties that have been determined previously by the MiniBooNE and MicroBooNE collaborations. The uncertainty of charged pion production at the beam target, for example, has been determined through comparisons of spline fits to externally-collected data from the HARP ex-

periment and the nominal Sanford-Wang model parameterizing the underling differential cross sections. A complete description of uncertainties on BNB flux parameters is provided in Ref. [37].

The impact of flux uncertainties on event counts in the ν_μ CC π^0 selection is evaluated through event reweighting, where parameters affecting the probability of an interaction occurring are varied within their predefined uncertainties in a number of "universes." One thousand universes are employed in this analysis, each of which is used to assign weights to neutrino interactions in order to assess the impact of the parameter variations. A covariance matrix then captures the uncertainty on binned observables by comparing event counts across different universes and the nominal or "central value" simulation.

$$V_{ij} = \frac{1}{N}\sum_{k}^{N}(M_i^k - M_i^{CV})(M_j^k - M_j^{CV}) \tag{9.1}$$

where N is the number of universes, M_i^k (M_j^k) is the measured event count for bin i (j) in the k^{th} universe, and M_i^{CV} (M_j^{CV}) is the measured event count for bin i (j) in the central value universe. The systematic uncertainty on the counts of each bin is then given by the square root of the diagonal elements of the covariance matrix.

Table 9.1 reports total fractional uncertainties for BNB flux parameters considered in the analysis. The leading source of uncertainty is attributed to modeling of the "skin depth," or the depth with which the horn current penetrates the horn conductor. The combined uncertainty of all BNB flux parameters is approximately 9% and is subdominant to interaction model uncertainties, which are discussed in the following section.

9.2 Interaction Model Uncertainties

Neutrino interactions with argon nuclei are modeled according to GENIE, where dozens of cross section parameters influence the type and probability of interactions occurring. Similar to the flux model, each parameter may be varied within its prior uncertainty in a number of universes to build a covariance matrix describing the associated uncertainty on selected event counts. Alterna-

Table 9.1: Fractional systematic uncertainties on the number of selected ν_μ CC π^0 interactions for parameters associated with the BNB flux.

Parameter	Description	Uncertainty [%]
piminus	π^- production in beam target	0.1
piplus	π^+ production in beam target	5.3
kminus	K^- production in beam target	0.0
kplus	K^+ production in beam target	0.6
kzero	K^0 production in beam target	0.0
expskin	Current induced on surface of focusing horn	6.1
horncurrent	Current pulsed through focusing horn	0.8
nucleoninexsec	Nucleon inelastic re-scattering in beamline	0.8
nucleonqexsec	Nucleon QE re-scattering in beamline	2.4
nucleontotxsec	Nucleon total re-scattering in beamline	0.7
pioninexsec	π inelastic re-scattring in beamline	1.3
pionqexsec	π QE re-scattering in beamline	0.9
piontotxsec	π total re-scattering in beamline	1.0
Total		8.7

tively, event-by-event weights corresponding to specific parameter variations (e.g. $\pm1\sigma, \pm2\sigma, \pm3\sigma$) can be computed. The latter approach is chosen for this analysis, as the event weights can be used to construct splines that are applicable to defining parameter response functions in later cross section extraction procedures.

From event splines, a covariance matrix in the form of Equation 9.1 can still be constructed through sampling of a Gaussian distribution, where values reflecting the number of standard deviations away from the mean are chosen at random. Each randomly-selected value corresponds to a universe, and the event splines are evaluated at the selected value of each universe in order to calculate event weights. Table 9.2 reports total fractional uncertainties for neutrino interaction model parameters considered in this analysis, calculated by applying the above method using one thousand universes. At nearly 30%, neutrino interaction model uncertainties are by far the leading source of variation on selected event counts. Leading contributions come from parameters related to charged-current resonance production in the Berger-Sehgal model (i.e. MaCCRES and MvCCRES), as well as those related to final-state interactions governing charge exchange and absorption within the nucleus.

Table 9.2: Fractional systematic uncertainties on the number of selected ν_μ CC π^0 interactions for parameters associated with the neutrino interaction model.

Parameter	Description	Uncertainty [%]
ZExpB1CCQE	B1 parameter of Z-expansion description of the axial-vector form factor on CCQE	0.1
ZExpB2CCQE	B2 parameter of Z-expansion description of the axial-vector form factor on CCQE	0.6
ZExpB3CCQE	B3 parameter of Z-expansion description of the axial-vector form factor on CCQE	0.2
ZExpB4CCQE	B4 parameter of Z-expansion description of the axial-vector form factor on CCQE	0.2
RPA_CCQE	RPA supression for CCQE	1.2
CoulombCCQE	Strength of electromagnetic potential for Coulomb corrections on CCQE	0.0
VecFFCCQEshape	Alternate vector form factor shape for CCQE	0.2
NormCCMEC	Normalization of CCMEC	0.4
NormNCMEC	Normalization of NCMEC	0.0
DecayAngMec	Alternative angular distribution for outgoing nucleons in 2p2h interactions	0.4
MaCCRES	Axial-vector mass of CCRES dipole form factor	15.0
MvCCRES	Vector mass of CCRES dipole form factor	12.3
MaNCRES	Axial-vector mass of NCRES dipole form factor	0.2
MvNCRES	Vector mass of NCRES dipole form factor	0.1
RDecBR1gamma	Scale factor for the branching ratio of $X + \gamma$	0.1
RDecBR1eta	Scale factor for the branching ratio of $X + \eta$	1.5
ThetaDelta2Npi	Reweight π angular distribution in $\Delta \to N + \pi$ decay	0.3
ThetaDelta2NRad	Reweight γ angular distribution in $\Delta \to N + \gamma$ decay	0.0
NonRESBGvpCC1pi	Scale factor for non-resonant ν-p CC 1π background	0.1
NonRESBGvpCC2pi	Scale factor for non-resonant ν-p CC 2π background	1.4

Table 9.2 (continued)

Parameter	Description	Uncertainty [%]
NonRESBGvpNC1pi	Scale factor for non-resonant ν-p NC 1π background	0.0
NonRESBGvpNC2pi	Scale factor for non-resonant ν-p NC 2π background	0.1
NonRESBGvnCC1pi	Scale factor for non-resonant ν-n CC 1π background	1.4
NonRESBGvnCC2pi	Scale factor for non-resonant ν-n CC 2π background	1.9
NonRESBGvnNC1pi	Scale factor for non-resonant ν-n NC 1π background	0.0
NonRESBGvnNC2pi	Scale factor for non-resonant ν-n NC 2π background	0.1
NonRESBGvbarpCC1pi	Scale factor for non-resonant $\bar{\nu}$-p CC 1π background	0.0
NonRESBGvbarpCC2pi	Scale factor for non-resonant $\bar{\nu}$-p CC 2π background	0.0
NonRESBGvbarpNC1pi	Scale factor for non-resonant $\bar{\nu}$-p NC 1π background	0.0
NonRESBGvbarpNC2pi	Scale factor for non-resonant $\bar{\nu}$-p NC 2π background	0.0
NonRESBGvbarnCC1pi	Scale factor for non-resonant $\bar{\nu}$-n CC 1π background	0.0
NonRESBGvbarnCC2pi	Scale factor for non-resonant $\bar{\nu}$-n CC 2π background	0.0
NonRESBGvbarnNC1pi	Scale factor for non-resonant $\bar{\nu}$-n NC 1π background	0.0
NonRESBGvbarnNC2pi	Scale factor for non-resonant $\bar{\nu}$-n NC 2π background	0.0
AhtBY	A_{HT} higher-twist parameter in Bodek-Yang model scaling ξ_W	0.0
BhtBY	B_{HT} higher-twist parameter in Bodek-Yang model scaling ξ_W	0.0
CV1uBY	CV1u valence GRV98 PDF correction parameter in the Bodek-Yang model	0.0
CV2uBY	CV2u valence GRV98 PDF correction parameter in the Bodek-Yang model	0.0
NormCCCOH	Normalization of CC COH interactions	0.0

Table 9.2 (continued)

Parameter	Description	Uncertainty [%]
NormNCCOH	Normalization of NC COH interactions	0.0
MFP_pi	Scale factor for the mean free path in the FSI of π	0.4
FrCEx_pi	Scale factor for the fraction of charge-exchange fate in the FSI of π	18.0
FrInel_pi	Scale factor for the fraction of inelastic scattered fate in the FSI of π	4.7
FrAbs_pi	Scale factor for the fraction of absorption fate in the FSI of π	11.9
FrPiProd_pi	Scale factor for the fraction of π production fate in the FSI of π	0.5
MFP_N	Scale factor for the mean free path in the FSI of nucleon	0.2
FrCEx_N	Scale factor for the fraction of charge-exchange fate in the FSI of nucleon	0.6
FrInel_N	Scale factor for the fraction of inelastic scattered fate in the FSI of nucleon	0.2
FrAbs_N	Scale factor for the fraction of absorption fate in the FSI of nucleon	0.3
FrPiProd_N	Scale factor for the fraction of π production fate in the FSI of nucleon	0.8
MaNCEL	Axial-vector mass of NCEL dipole form factor	0.0
EtaNCEL	Strange axial-vector mass of NCEL dipole form factor	0.0
Total		29.6

9.3 Detector Model Uncertainties

Unlike the neutrino flux and interaction models, uncertainties in the detector model do not directly impact the probability of a neutrino interaction occurring or the kinematics of the resultant final-state particles. Rather, they impact measurables such as the number of ionization electrons and scintillation photons reaching readout elements, as well as the response of each readout element to these signals. For this reason, event reweighting is not a valid approach for quantifying

detector model uncertainties. Instead, dedicated simulation samples have been produced in which some element of the detector response simulation is modified from its nominal value. The intent of this approach is to characterize effects that are not fully understood or modeled correctly in the current ICARUS simulation. Elements of the detector response model that have been varied in dedicated samples include:

- **Electron Lifetime**: The nominal electron lifetime in the ICARUS simulation is 3 ms. However, analysis of cosmic-ray muon data shows cryostat dependence, with an east cryostat electron lifetime of $\sim$4 ms and a west cryostat electron lifetime of $\sim$8 ms. For this reason, a variation sample with 8 ms electron lifetime was produced and offers a conservative estimate of the uncertainty related to the discrepancy.

- **Induction 1 Wire Gap**: The first induction wire plane of ICARUS consists of two sections of horizontally-oriented wires held together by a 37 mm support structure at the center of the ICARUS detector (in the beam direction). The structure creates a "wire gap" and is seen to cause track reconstruction failures in data, but was not simulated in the nominal ICARUS simulation. Therefore, a variation sample was produced in which the gap is included.

- **Recombination**: Electron-ion recombination is nominally simulated with the modified Box Model, but studies have shown the amount of recombination to depend on the angle of particle trajectories relative to the drift electric field direction. This is encapsulated with an ellipsoidal modified Box model of recombination [51], which has been simulated in a variation sample.

- **PMT QE**: A discrepancy exists between the amount of scintillation light collected by ICARUS PMTs and that simulated by the ICARUS optical model. A variation meant to cover this discrepancy has been produced in which the nominal PMT quantum efficiency (QE) is lowered from 7.3% to 4%.

- **YZ-Nonuniformity**: Analysis of cosmic muon data has shown charge scale variations in the plane transverse to the drift electric field (YZ-plane) due to wire plane intransparency. This YZ-dependence of the charge scale has been implemented in a variation sample.

- **TPC Noise**: Channel-by-channel variations of intrinsic and coherent noise were seen during Run 2 data collection, but are not simulated nominally at ICARUS. To account for this, variation samples in which intrinsic noise is varied by $\pm 10\%$ and coherent noise is varied by $\pm 5\%$ have been produced.

- **Induction 2 Shaping Time**: A known bias exists between the second induction wire plane's shaping time in the nominal ICARUS simulation (1.3 μs) and observations from data (1.45 μs). A variation sample has been produced to reflect the more realistic shaping time.

- **Signal Shape Variation**: The simulated field response shape of each TPC wire plane has been tuned to match measurements in data. However, the nominal ICARUS simulation does not include any tuning for the first induction plane, and imperfections exist in the tunings of the other wire planes. Therefore, variation samples in which the signal shape is stretched/squeezed by 15% have been produced.

Each variation sample listed above, as well as a central value sample representing the nominal ICARUS detector simulation configuration, begins with the generation of 200,000 neutrino events distributed throughout the beam spill gate and out-of-time cosmic-ray muons. The central value sample is then subject to the standard implementation of the particle propagation and detector response simulation stages, while modifications are made to these stages to achieve the desired effect of each detector variation. Simulated events from the central value and variation samples are then passed through low-level reconstruction and the SPINE framework, after which event selections can be carried out.

To assess the systematic uncertainty associated with a particular detector variation, the ratio between selected event counts in the variation sample and the central value sample is formed in bins of a representative variable. Given the presence of both tracks and showers in the ν_μ CC π^0

analysis, the reconstructed visible energy of each interaction is used to calculate the binned ratios. As an example, this distribution is shown for both the central value sample and ellipsoidal recombination variation sample in Figure 9.1. The ratio is representative of the $\pm 1\sigma$ variation of a particular element of the detector response and can be scaled to form splines at arbitrary standard deviations. As was the case for neutrino interaction model uncertainties, the splines can then be used to form response dials for downstream use in cross section extraction procedures or in computing a covariance matrix through which uncertainties on event counts can be calculated directly.

Fractional uncertainties on the selected number of ν_μ CC π^0 interactions that are associated with each detector variation are shown in Table 9.3. The largest uncertainty ($\sim$4%) is due to the recombination model employed in event simulation, which has a direct impact on the TPC charge scale. Still, the scale of this and other uncertainties related to the detector model are small in comparison to those associated with the flux and neutrino interaction models.

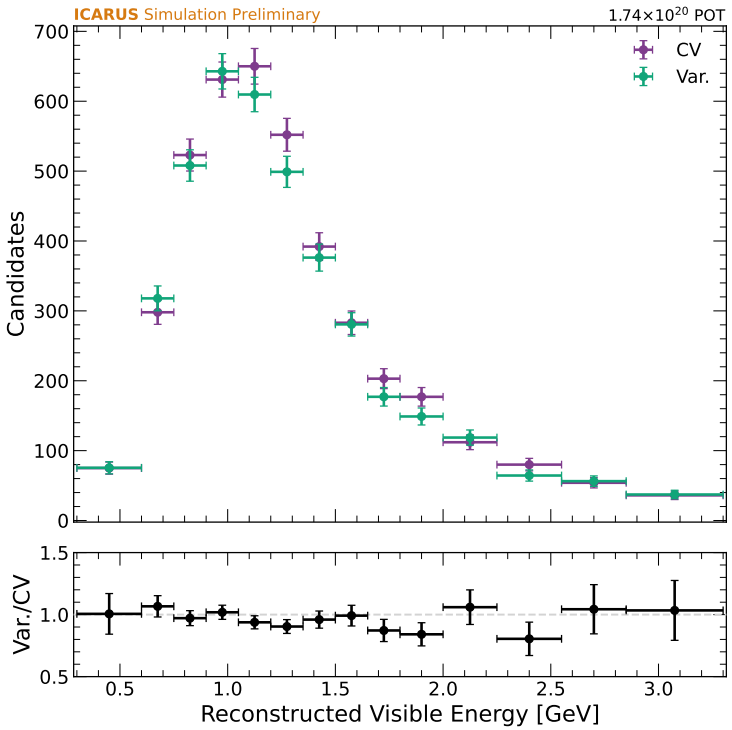

Figure 9.1: Selected ν_μ CC π^0 event counts in bins of reconstructed visible energy for the simulated central value and recombination detector variation samples. The ratio of these distributions is used to assess the impact of the detector variation sample.

Table 9.3: Fractional systematic uncertainties on the selected number of ν_μ CC π^0 interactions for detector model variations.

Variation	Description	Uncertainty [%]
High Electron Lifetime	Simulate electron lifetime of 8 ms	0.2
TPC Induction 1 Gap	Simulate first induction wire plane gap	1.4
Recombination	Simulate EMB model of recombination	3.6
PMT QE	Decrease PMT quantum efficiency to 4%	0.5
TPC YZ-Nonuniformity	Simulate YZ-nonuniformity	0.3
TPC Intrinsic Noise	Vary intrinsic noise component by $\pm 10\%$	0.7
TPC Coherent Noise	Vary coherent noise component by $\pm 5\%$	0.2
TPC Induction 2 Shaping Time	Simulate 1.45 µs electronics shaping time	0.2
TPC Signal Shape	Vary signal shape width by $\pm 15\%$	0.8
Total		4.0

9.4 Summary of Systematic Uncertainties

In summary, systematic uncertainties on the number of selected event counts are large in the ν_μ CC π^0 analysis, mostly being driven by large prior uncertainties on neutrino interaction model parameters governing charged-current resonance production and final-state interactions. The total contribution from each source of systematic uncertainty considered in this analysis is summarized in Table 9.4, along with the statistical uncertainty of the central value Monte Carlo simulation sample. Fractional uncertainties on the selected number of ν_μ CC π^0 interactions for each systematic uncertainty category are then shown in Figure 9.2 as a function of reconstructed visible energy.

In future updates to the analysis, some components of the systematic uncertainty model may no longer be necessary. This is especially true for the detector model, as improvements to the nominal ICARUS Monte Carlo simulation will make specific variation samples obsolete. On the other hand, there are certain features missing from the current systematic uncertainty model that are expected to be included in the next iteration of the analysis. One such example is the assessment of uncertainties on secondary interactions within argon that happen outside of the nucleus where the initial neutrino interaction occurred. While expected to be smaller in magnitude than those associated with the primary neutrino interaction, these uncertainties will ultimately cover events

Table 9.4: Fractional uncertainties on the number of selected ν_μ CC π^0 interactions broken down by systematic uncertainty category.

Category	Uncertainty [%]
Flux Model	8.7
Interaction Model	29.6
Detector Model	4.0
MC Statistics	0.5
Total	31.1

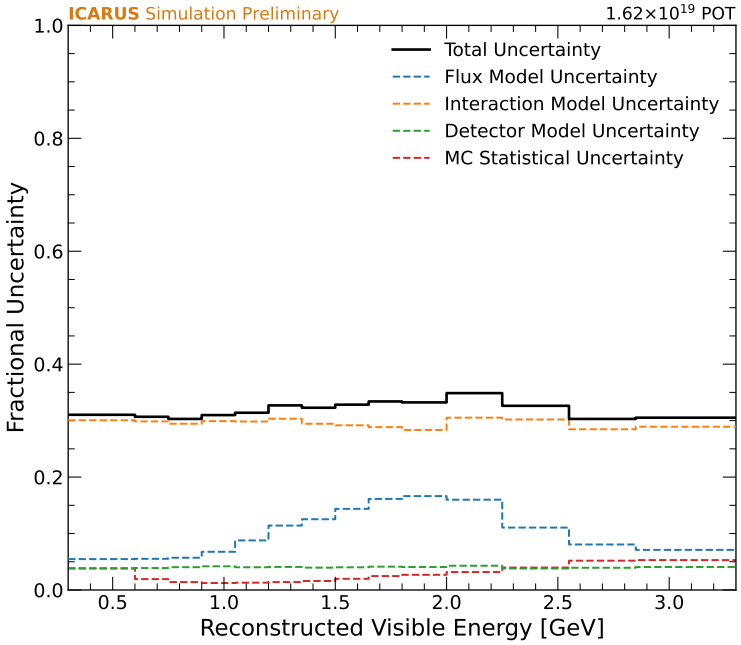

Figure 9.2: Fractional uncertainties on the number of selected ν_μ CC π^0 interactions as a function of reconstructed visible energy.

where a final-state neutral pion is absorbed before decaying or where a final-state charged pion undergoes charge conversion, resulting in an observable neutral pion.

9.5 Data/Simulation Comparisons

In this section, comparisons between data and simulation are made for previously introduced reconstructed variables of interest. 10% of the BNB Run 2 on-beam dataset is used, in line with the ICARUS blinding policy that states any analysis that accesses the full Run 2 dataset must be

completely finalized. The central value BNB ν + Cosmic Monte Carlo simulation sample gives the simulated prediction, with BNB off-beam data used to estimate in-time cosmic contributions.

For reference, all reconstructed observables presented in this section are listed here:

- **Low-Level Observables:**
  - Neutrino vertex x (y) (z) component is shown in Figure 9.3 (9.4) (9.5).
  - Muon length is shown in Figure 9.6.
  - Subleading and leading photon conversion distances are shown in Figure 9.7.
- **TKI Variables:** δp_{T} and $\delta \alpha_{\mathrm{T}}$ are shown in Figure 9.8.
- **Neutrino Energy Transfer Variables:** Q^2 and W are shown in Figure 9.9
- **Neutral Pion Mass Observables:**
  - Subleading and leading photon energies are shown in Figure 9.10.
  - The opening angle between photons is shown in Figure 9.11.
  - Neutral pion mass is shown in Figure 9.12.
- **Cross Section Analysis Variables:** Momentum and angle relative to the neutrino beam direction are shown for the muon and neutral pion in Figure 9.13.

For all variables considered, each contributing sample is scaled to the amount of on-beam data used in the cross section measurement. In the case of the central value Monte Carlo simulation sample, this scaling is based on POT, while the off-beam contribution is scaled according to the number of beam spills. In general, good shape agreement is seen between data and simulation, and normalization differences are largely covered by systematic uncertainties related to the simulation.

9.6 Charged Pion Background Study

Section 8.3 reported that the largest background in the ν_μ CC π^0 selection involves neutrino interactions with charged pions that are misidentified as muons or protons. In cross section analyses,

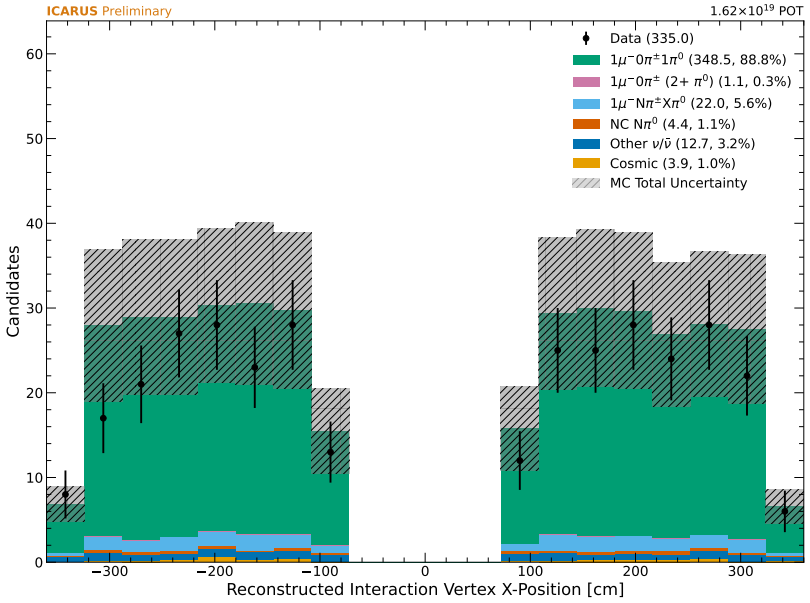

Figure 9.3: Reconstructed neutrino vertex x component for selected ν_μ CC π^0 interactions in simulation and the unblinded 10% of ICARUS BNB Run 2 data.

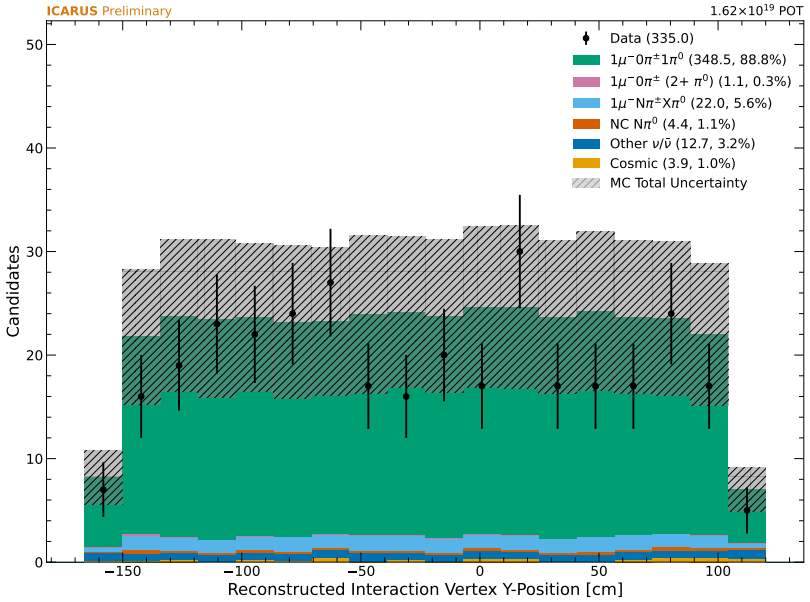

Figure 9.4: Reconstructed neutrino vertex y component for selected ν_μ CC π^0 interactions in simulation and the unblinded 10% of ICARUS BNB Run 2 data.

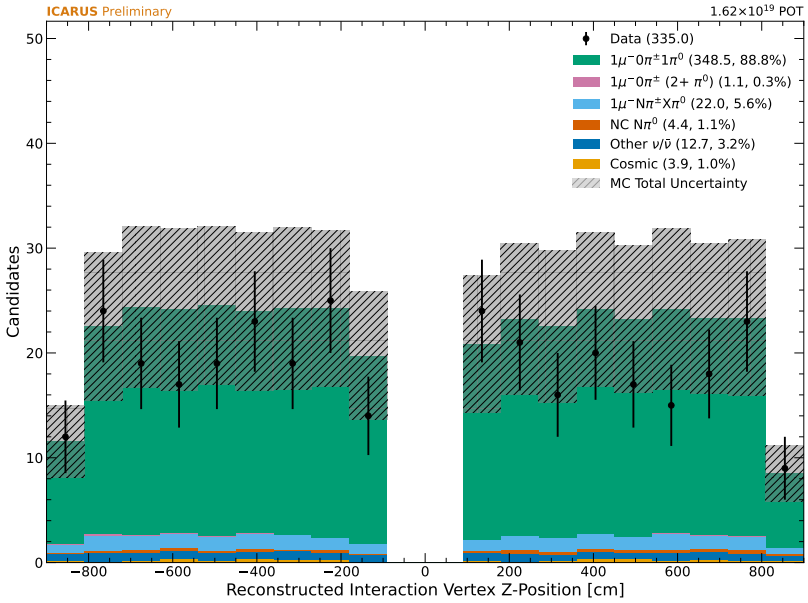

Figure 9.5: Reconstructed neutrino vertex z component for selected ν_μ CC π^0 interactions in simulation and the unblinded 10% of ICARUS BNB Run 2 data.

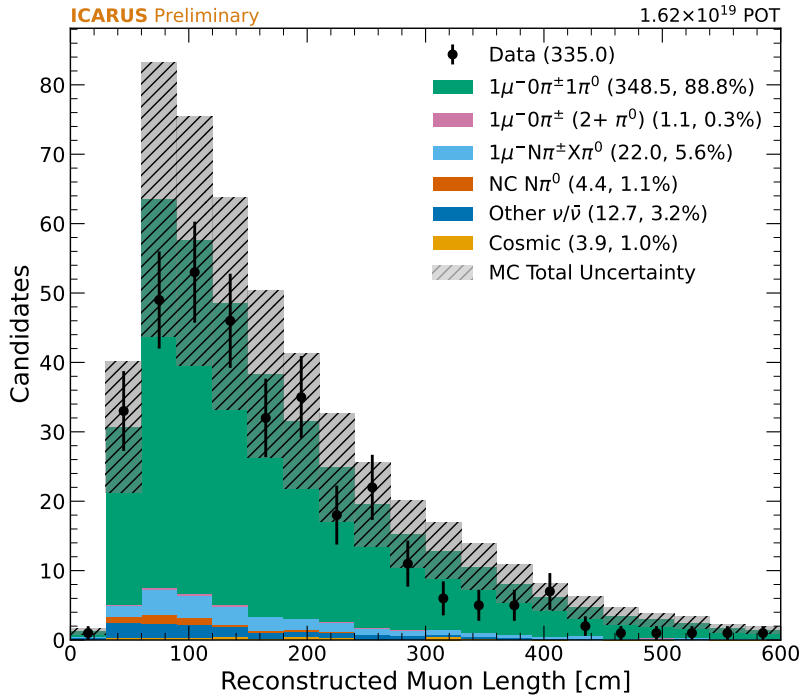

Figure 9.6: Reconstructed muon length for selected ν_μ CC π^0 interactions in simulation and the unblinded 10% of ICARUS BNB Run 2 data.

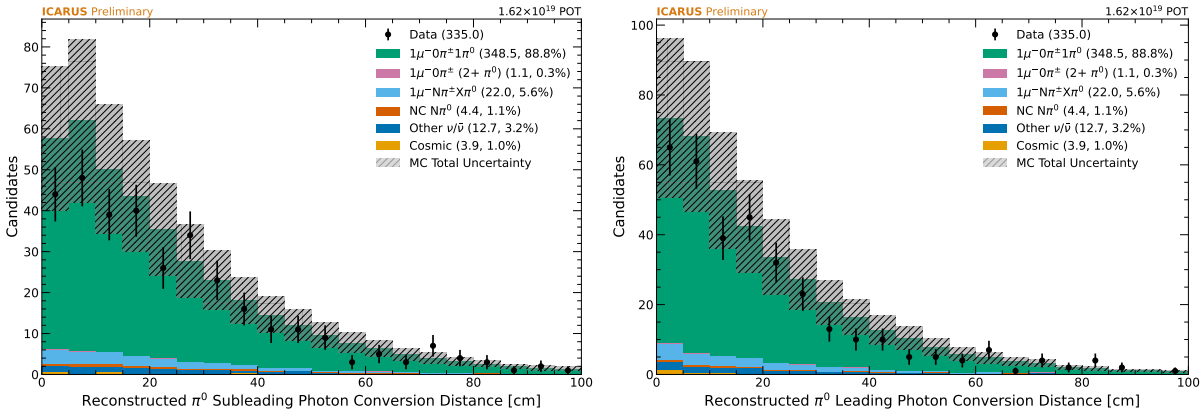

Figure 9.7: Reconstructed subleading (left) and leading (right) photon conversion distances for selected ν_μ CC π^0 interactions in simulation and the unblinded 10% of ICARUS BNB Run 2 data.

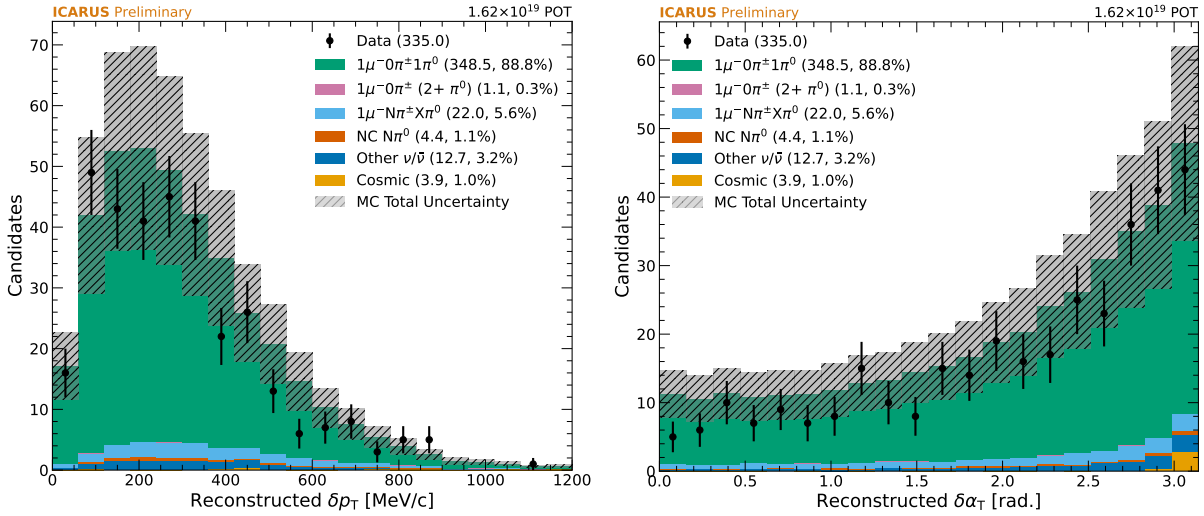

Figure 9.8: Reconstructed transverse momentum imbalance (left) and boosting angle (right) for selected ν_μ CC π^0 interactions in simulation and the unblinded 10% of ICARUS BNB Run 2 data.

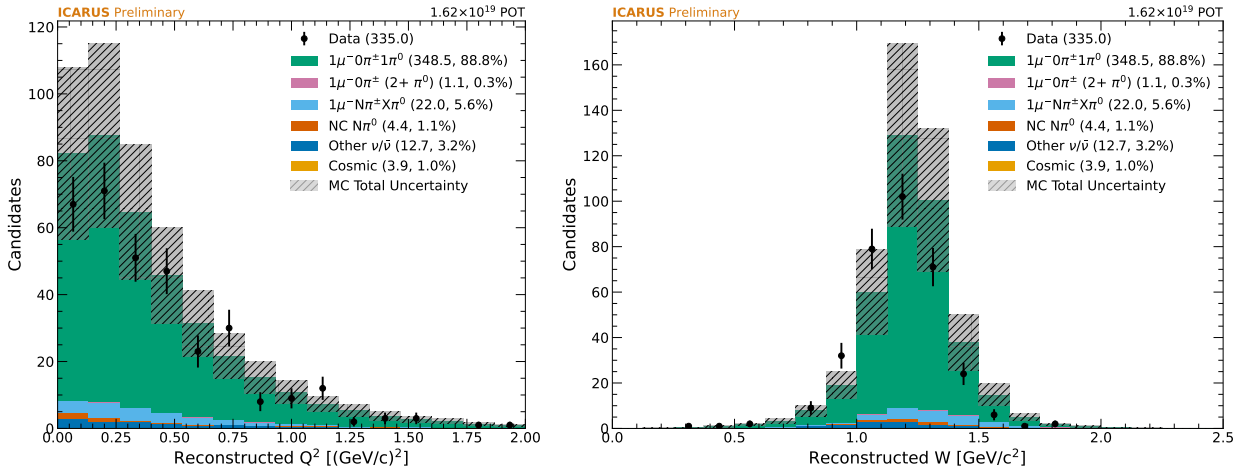

Figure 9.9: Reconstructed squared four-momentum transfer (left) and hadronic invariant mass (right) for selected ν_μ CC π^0 interactions in simulation and the unblinded 10% of ICARUS BNB Run 2 data.

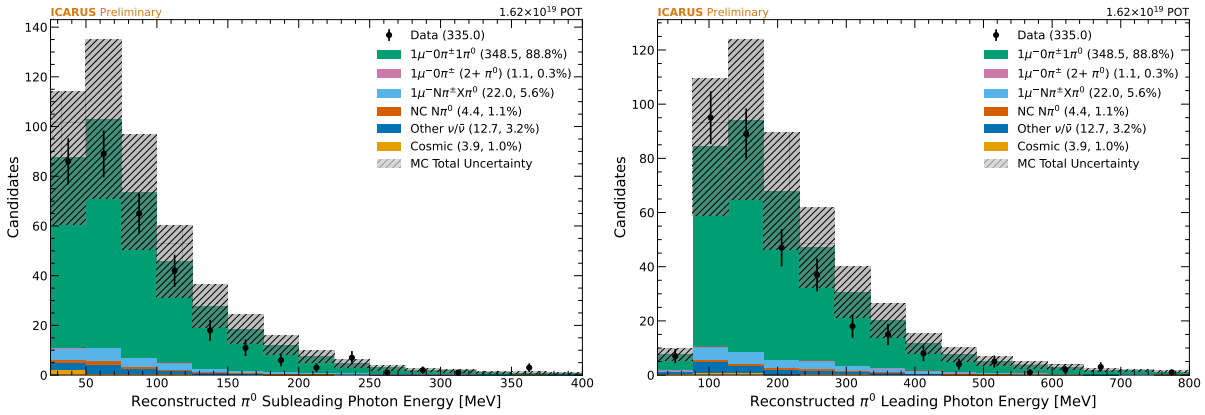

Figure 9.10: Reconstructed subleading (left) and leading (right) photon energies for selected ν_μ CC π^0 interactions in simulation and the unblinded 10% of ICARUS BNB Run 2 data.

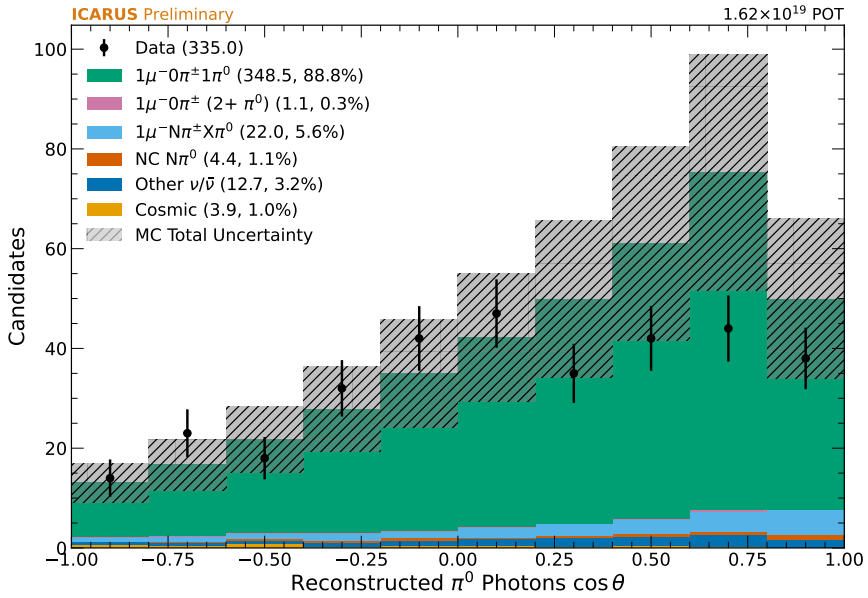

Figure 9.11: Reconstructed π^0 $\cos\theta_{\gamma\gamma}$ for selected ν_μ CC π^0 interactions in simulation and the unblinded 10% of ICARUS BNB Run 2 data.

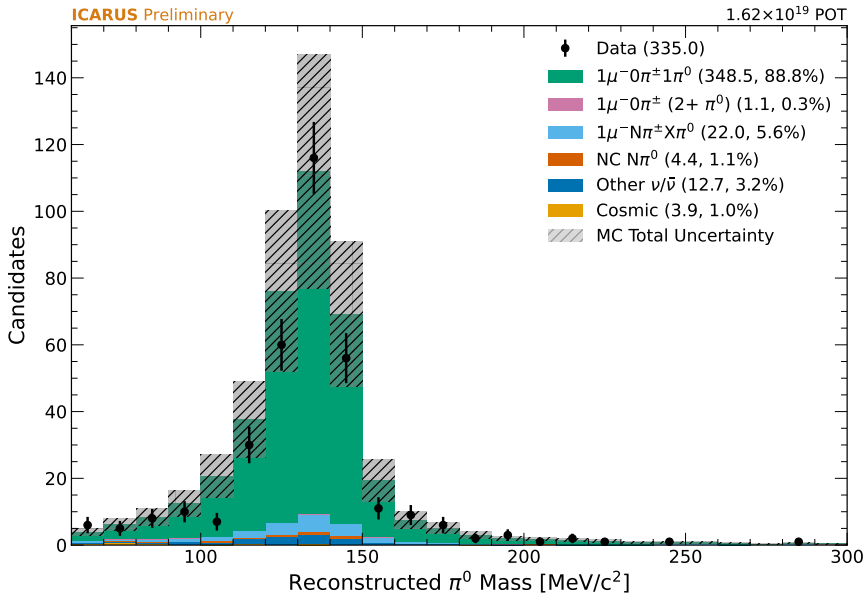

Figure 9.12: Reconstructed neutral pion mass for selected ν_μ CC π^0 interactions in simulation and the unblinded 10% of ICARUS BNB Run 2 data.

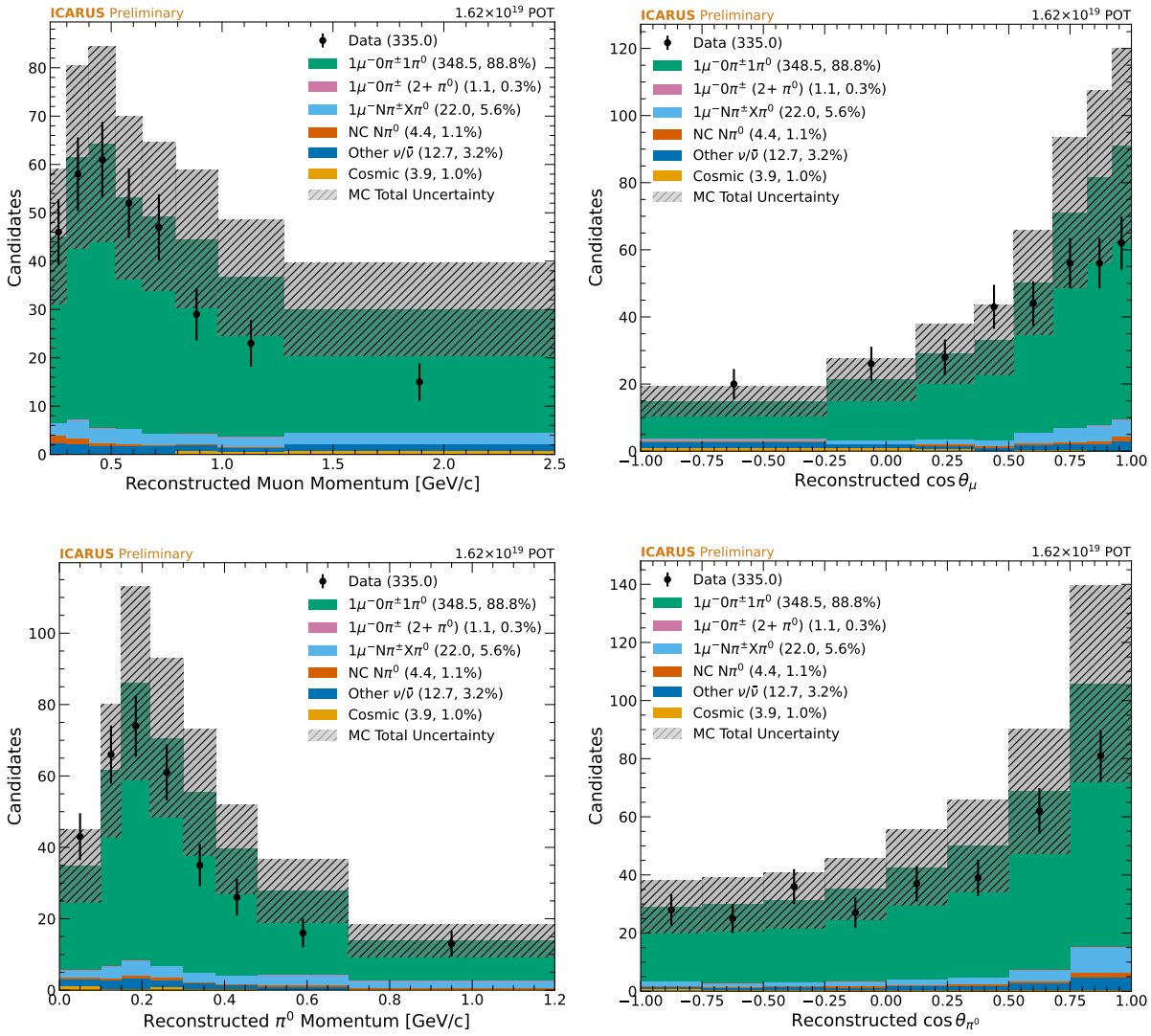

Figure 9.13: Reconstructed cross section observables for selected ν_μ CC π^0 interactions in simulation and the unblinded 10% of ICARUS BNB Run 2 data. Muon momentum and angle with respect to the BNB direction are shown in the top row, while the same quantities are shown for the neutral pion in the bottom row.

it is important to check that no significant mismodeling exists for prominent backgrounds in order to avoid bias in extracted measurements. For this reason, a sideband selection rich in charged pions has been developed by inverting the ν_μ CC π^0 "zero primary charged pions" cut. The reconstructed neutral pion mass distribution is shown for this selection in Figure 9.14, showing that over 70% of selected interactions contain charged pions.

In cross section extraction procedures, the charged pion sideband can provide a data-driven constraint on the charged pion background and reduce reliance on model predictions. While the

sideband may formally be included in future iterations of the ν_μ CC π^0 analysis, it is omitted from the initial cross section analysis presented in Chapter 10, given the small size of the background ($<$6%) and limited statistics at the current level of exposure. Nevertheless, the comparison between data and Monte Carlo simulation in Figure 9.14 shows that GENIE does not dramatically mismodel the charged pion background in the signal region beyond the measurement's limitations from systematic uncertainties.

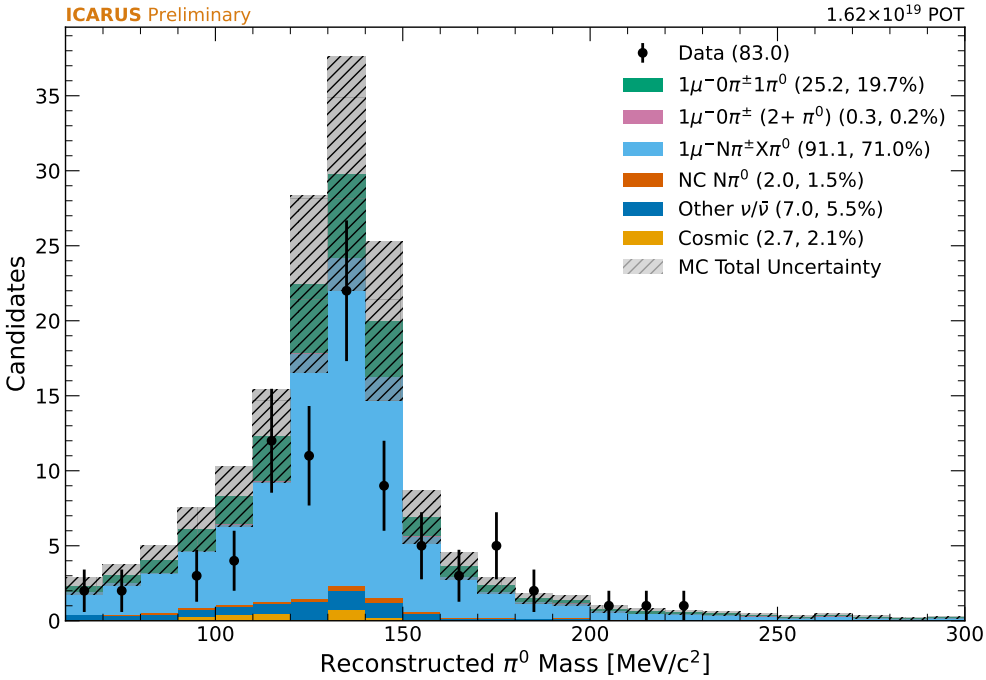

Figure 9.14: Reconstructed neutral pion mass for interactions belonging to the charged pion sideband region of the ν_μ CC π^0 selection in simulation and the unblinded 10% of ICARUS BNB Run 2 data.

Chapter 10

Cross Section Measurement

The culmination of this thesis is a measurement of ν_μ CC π^0 production on argon. Specifically, single-differential cross sections as a function of momentum and angle with respect to the BNB direction for the muon and neutral pion of the interaction are measured. Section 10.1 explains the cross section extraction procedure, including a summary of all measurement inputs and an overview of the fitting method employed. Section 10.2 then explores a number of mock data studies that demonstrate aforementioned procedure, followed by the presentation of the cross section measurement results with BNB data in Section 10.3.

10.1 Cross Section Extraction Procedure

In a single-differential cross section analysis, the dependence of the cross section on a specific variable is assessed. The measured cross section in true bin i of variable X is given by

$$\left.\frac{\mathrm{d}\sigma}{\mathrm{d}X}\right|_i = \frac{N^{\text{sig}}_{i,\text{unfolded}}}{\Phi\ N_{\text{targets}}}\frac{1}{\Delta X_i}. \tag{10.1}$$

Here, $N^{\text{sig}}_{i,\text{unfolded}}$ is referred to as the "unfolded" number of signal events in bin i because it corresponds to the number of background-subtracted signal events that have been corrected for detector smearing and acceptance. The true bin width is given by ΔX_i, while Φ and N_{targets} give the integrated neutrino flux and number of nucleon targets in the volume of interest, respectively.

A wide range of methods exist within the neutrino cross section community to compute the numerator of Equation 10.1, which is seen as the crux of most measurements. D'Agostini unfolding [67], for example, has historically been used most frequently and involves an iterative Bayesian approach to estimate true signal event counts from observed data. More recently, experiments like MicroBooNE and SBND have used the Wiener-SVD method [68], which relies on signal processing techniques to invert a response matrix that encapsulates detector smearing. First cross section

measurements at ICARUS, including those in the ν_μ CC π^0 analysis, have utilized a maximum likelihood fitting approach first developed by T2K collaborators. This method is implemented in the open-source GUNDAM statistical analysis suite [69], allowing ICARUS analyzers to perform highly configurable fits en route to cross section extractions, as well as providing tools to validate results with mock data studies and goodness-of-fit diagnostics.

When performing a fit with GUNDAM, the core strategy in computing the number of true signal events is to minimize a negative log-likelihood of the following form:

$$\begin{aligned} -2\ln\mathcal{L} &= -2\ln\mathcal{L}_{\text{stat}} - 2\ln\mathcal{L}_{\text{syst}} \\ &= \sum_j 2(N_j^{\text{sim}} - N_j^{\text{data}} + N_j^{\text{data}}\ln\frac{N_j^{\text{data}}}{N_j^{\text{sim}}}) + (\vec{a}^{\,\text{syst}} - \vec{a}^{\,\text{syst}}_{\text{prior}})(V^{\text{syst}}_{\text{cov}})^{-1}(\vec{a}^{\,\text{syst}} - \vec{a}^{\,\text{syst}}_{\text{prior}}), \end{aligned} \tag{10.2}$$

where N_j^{sim} and N_j^{data} are the selected event counts for reconstructed bin j in simulation and data, respectively. The second term includes nuisance parameters $\vec{a}^{\,\text{syst}}$ that correspond to systematic uncertainties in the flux, neutrino interaction, and detector models. Pre-fit values of these parameters are given by $\vec{a}^{\,\text{syst}}_{\text{prior}}$ and their prior uncertainties are described by the covariance matrix $V^{\text{syst}}_{\text{cov}}$.

In Equation 10.2, N_j^{sim} is parameterized by template parameters c_i for each true bin i and the previously-mentioned nuisance parameters $\vec{a}^{\,\text{syst}}$:

$$N_j^{\text{sim}} = \sum_i [c_i N_{ij}^{\text{sim sig}}(\vec{a}^{\,\text{syst}}) + N_{ij}^{\text{sim bkg}}(\vec{a}^{\,\text{syst}})], \tag{10.3}$$

where $N_{ij}^{\text{sim sig}}$ ($N_{ij}^{\text{sim bkg}}$) is the number of simulated signal (background) events simultaneously in true bin i and reconstructed bin j. Unlike nuisance parameters that are constrained by the systematic penalty term in Equation 10.2, template parameters are allowed to float freely in the fit and act as weights on the signal events in each true bin.

Upon minimization, the results of the fit include a vector of post-fit parameters and a covariance matrix representing their correlated uncertainties. The vector of post-fit parameters is propagated

to all simulated signal events, yielding the unfolded number of signal events in true bin i as:

$$N^{\text{sig}}_{i,\text{ unfolded}} = \frac{1}{\epsilon_i} \sum_j c_{i,\text{ post-fit}} N^{\text{sim sig}}_{ij}(\vec{a}^{\text{ syst}}_{\text{post-fit}}), \tag{10.4}$$

where ϵ_i corresponds to the selection efficiency in true bin i. As mentioned previously, efficiency corresponds to the fraction of true signal interactions that are matched to selected interactions. Technically, the efficiencies reported in Section 8.5 could be used in the calculation of Equation 10.4, though this would introduce a dependence on the particular neutrino event generator employed in the nominal ICARUS simulation (GENIE). To avoid this, the efficiency correction is calculated as a function of post-fit parameters as follows:

$$\epsilon_i = \frac{\sum_j N^{\text{sim sig}}_{ij}(\vec{a}^{\text{ syst}}_{\text{post-fit}})}{N^{\text{sim sig}}_{i}(\vec{a}^{\text{ syst}}_{\text{post-fit}})}. \tag{10.5}$$

Following the fit, the cross section extraction proceeds with the normalization of signal events by the integrated neutrino flux and number of nucleon targets. Using the BNB flux simulation introduced in Section 6.1.1, the muon neutrino flux through the front face of the ICARUS fiducial volume is determined. This is visualized as a histogram in Figure 10.1, the integral of which yields Φ in Equation 10.1. The number of fiducial nuclear argon targets is determined from the density of liquid argon ρ, the fiducial volume V_{fiducial}, the atomic weight of argon M_{Ar}, and the number of nucleons per argon atom N_{nucleons}:

$$\begin{aligned} N_{\text{targets}} &= \frac{\rho \cdot V_{\text{fiducial}} \cdot N_{\text{nucleons}}}{M_{\text{Ar}}} \\ &= \frac{1.39[\frac{\text{g}}{\text{cm}^3}] \cdot 1.98 \times 10^8[\text{cm}^3] \cdot 40}{6.63 \times 10^{-23}[\text{g}]} \\ &= 1.66 \times 10^{32} \text{ nucleons}. \end{aligned} \tag{10.6}$$

The final step in the cross section procedure is to propagate uncertainties from the binned likelihood fit to the final cross section result. For this, best-fit parameters are varied within the uncertainties allowed by the post-fit covariance matrix in a number of universes. The cross section

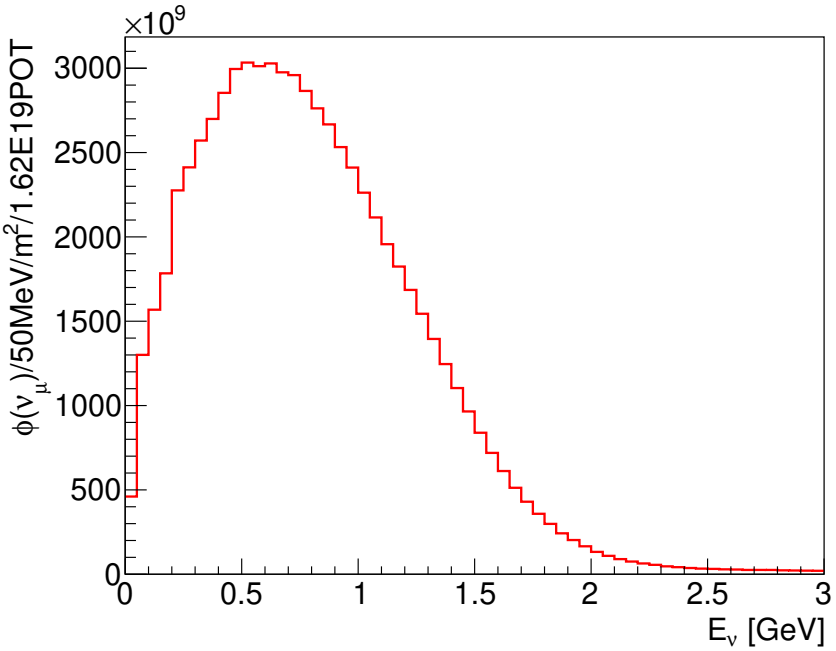

Figure 10.1: Muon neutrino flux through the front face of the ICARUS fiducial volume. Exposure corresponds to the unblinded 10% of BNB Run 2 data.

is recalculated for each universe, and the total uncertainty on the measurement is taken as the standard deviation across all universes.

10.2 Mock Data Studies

Before measuring cross sections with ICARUS neutrino data, the fitting procedures are first demonstrated through a series of mock data studies in which real data is replaced with some form of simulation. The simplest of these studies makes use of an Asimov dataset, where reconstructed event counts in data are assumed to be equal to predicted counts from the nominal ICARUS simulation. Given the role of template parameters as weights in each true analysis bin, it is expected that post-fit values for template parameters should be equal to one in this study. As seen in Figure 10.2, this result is obtained in the case of this analysis, serving as a validation for the fitting procedure.

Nuisance parameters can similarly be evaluated in the Asimov fit, and should again not deviate from their pre-fit values. As an example, neutrino interaction model parameters are shown in Figure 10.3 along with their uncertainties before and after the fit in bins of neutral pion momentum. As

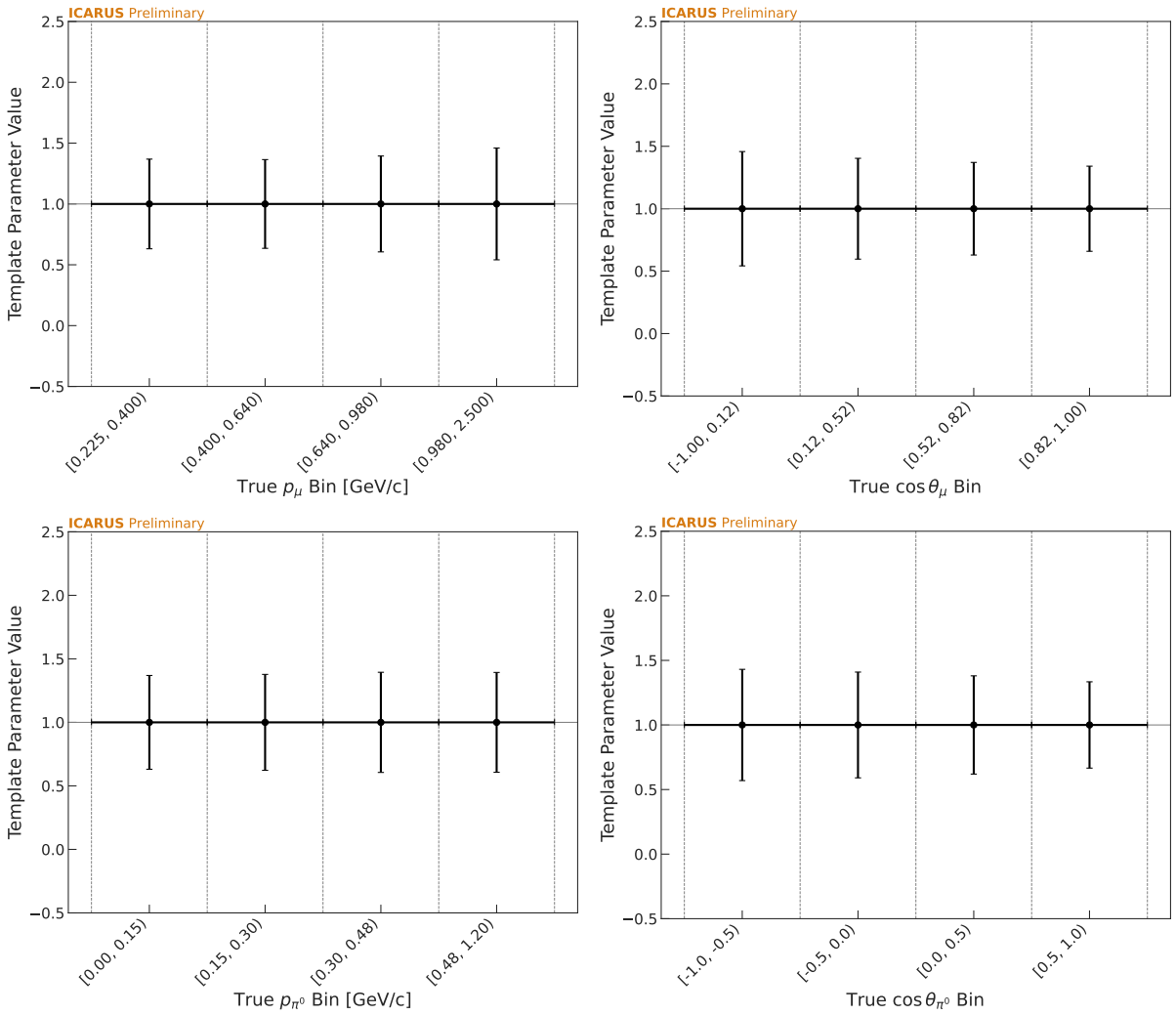

Figure 10.2: Post-fit template parameters for ν_μ CC π^0 analysis variables as obtained by carrying out the fit procedure using an Asimov dataset instead of collected ICARUS data. A value of one indicates the underlying simulation perfectly predicts the observed cross section in data.

was the case for template parameters, the fitter determined it was favorable to leave each neutrino interaction model parameter at its nominal value. Unlike template parameters, post-fit uncertainties on neutrino interaction model parameters can be reduced from their prior levels, though this is not largely seen in the ν_μ CC π^0 analysis. For prior uncertainties to be constrained, the adjustment of a particular neutrino interaction model parameter must affect predicted bin counts independently of other parameter adjustments, including those from template parameters controlling the true signal. In analyses involving neutral pions, neutrino interaction models parameters affecting event rates (e.g those relevant to resonance production or FSI) can often impact predicted event rates in the

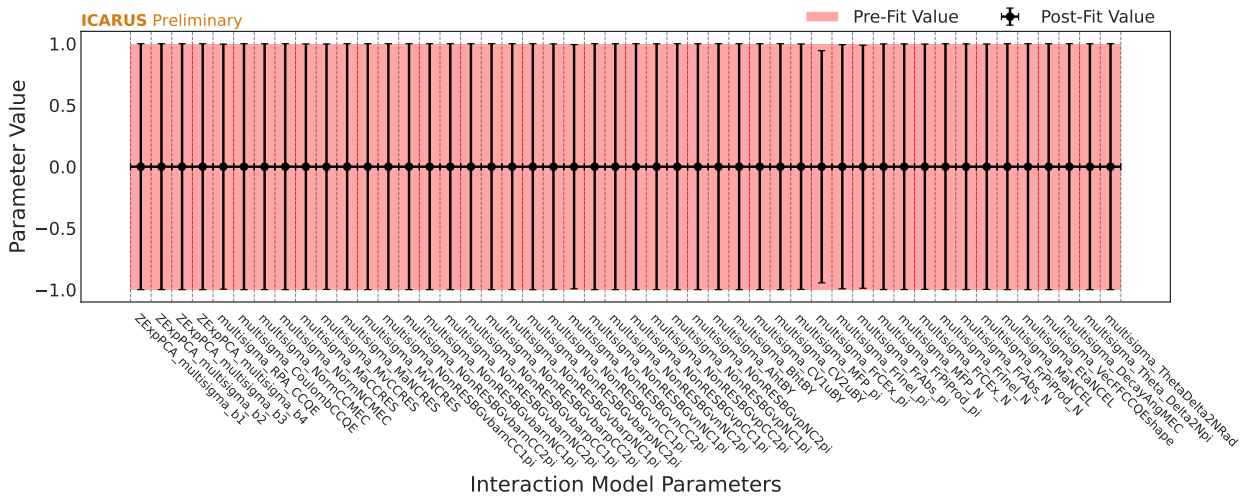

Figure 10.3: Neutrino interaction model parameters from an Asimov fit performed using the neutral pion momentum distribution. Uncertainties are shown before (red bands) and after (black error bars) the fit is performed.

same manner as template parameters, thus providing little information to the fitter for constraining prior uncertainties.

The Asimov mock data study also serves as a closure test to verify the fit is able to recover the expected cross section from the neutrino event generator used in simulation, which in this case is GENIE. Figure 10.4 shows that good agreement is reached for all analysis variables, with any discrepancy covered by statistical differences between the GENIE sample used to produce the analysis files processed through GUNDAM and the GENIE sample used to produce the reference curve.

As a logical extension to the Asimov study, one can construct a mock dataset in which observed event counts are determined by randomly drawing from a Poisson distribution defined by the central value Monte Carlo simulation prediction in each bin. With an ensemble of these random Poisson throws, the robustness of the uncertainty model is tested against random statistical fluctuations. For each cross section variable considered in this analysis, Figure 10.5 shows the distribution of post-fit template parameters for one thousand random throws. Each distribution is highlighted by the recovery of template parameter values near unity, on average, as desired.

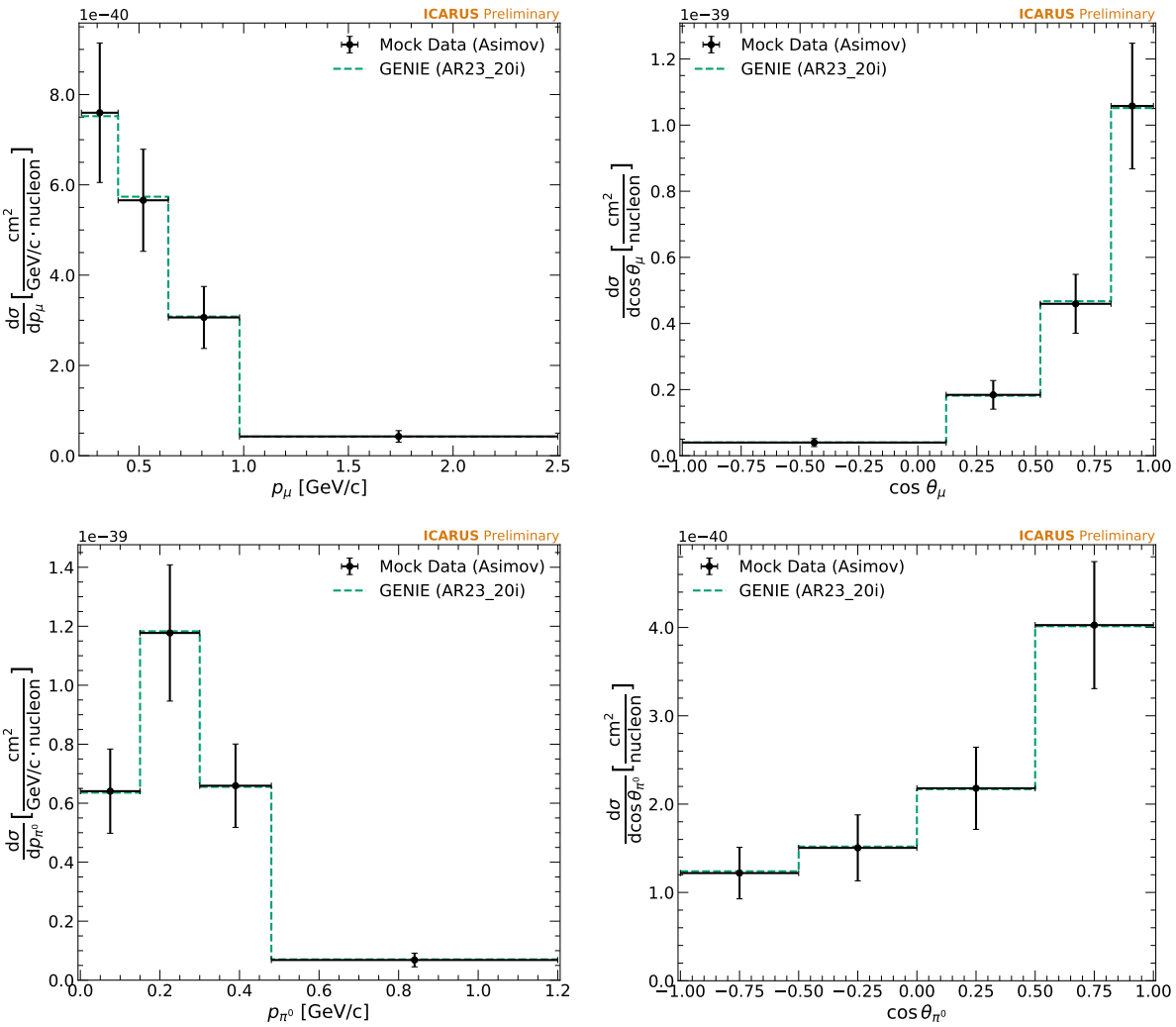

Figure 10.4: Comparison of cross sections extracted with an Asimov dataset (black scatter points) to cross sections predicted by the GENIE model used in the nominal ICARUS simulation (green dashed line).

In another stress test to the fitting procedure, observed bin counts are inferred from scaling simulated neutrino events according to their interaction mode (e.g. QE, RES, DIS). Given resonance interactions involving neutral pions are the dominant source of selected events and the fact that uncertainties related to the associated model parameters are large, mock datasets in which resonance interactions are weighted upward and downward by 20% are considered. As an example, reconstructed distributions and fit results for the latter case are shown in Figure 10.6 for neutral pion momentum. As expected, scaling resonance interactions downward results in observed mock data bin counts that have been reduced with respect to the nominal simulated prediction. Fit pa-

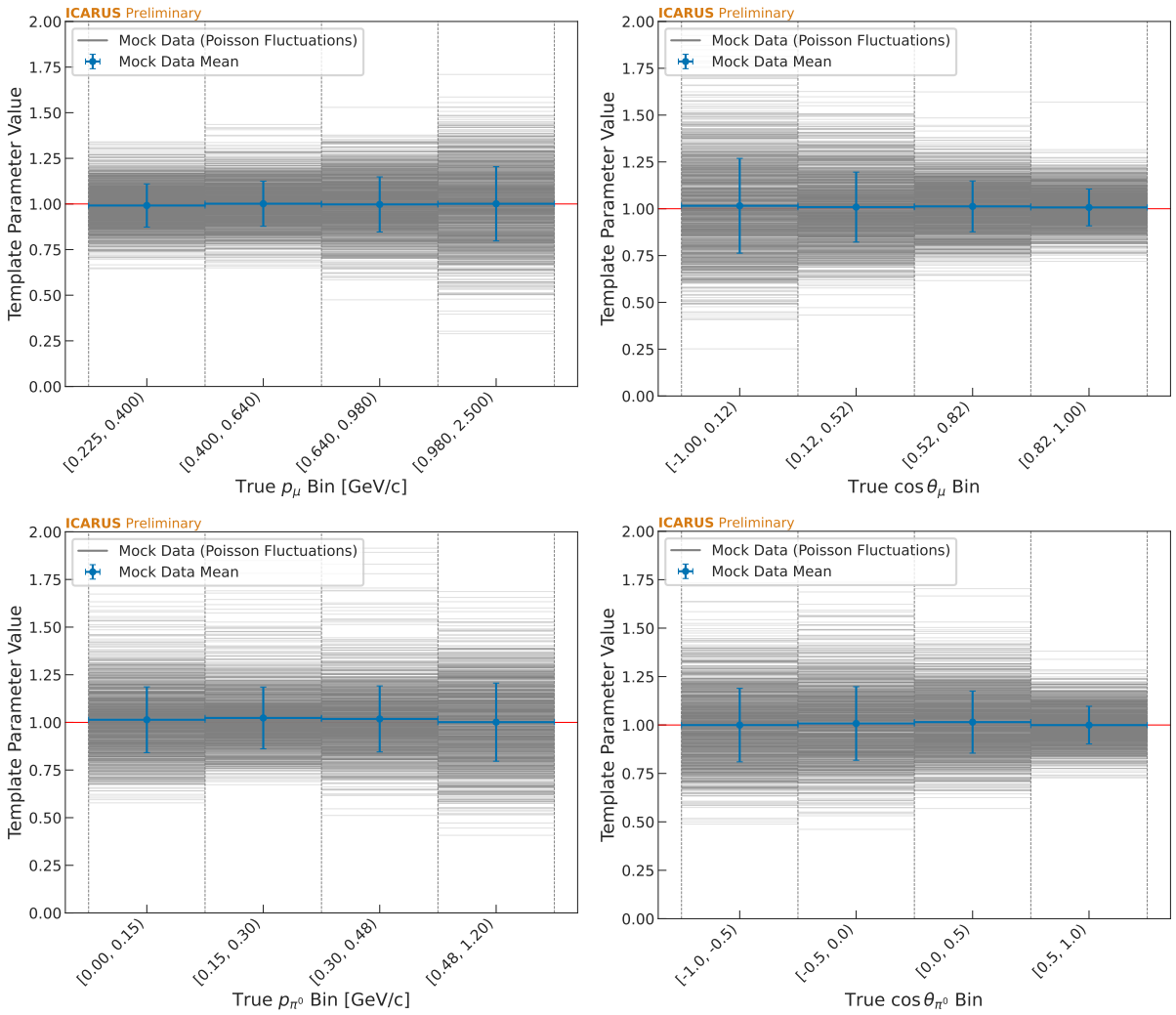

Figure 10.5: Post-fit template parameters for ν_μ CC π^0 analysis variables as determined with random Poisson throws specified with central value ICARUS Monte Carlo simulation bin counts.

rameters are pulled from their prior values accordingly, with template parameters seeing the most significant pulls.

Fit results of the RES-scaled mock data study are carried through to extracted cross sections for each analysis variable and shown in Figures 10.7 (downward weighting) and 10.8 (upward weighting). In each case, the extracted cross section closely matches the prediction obtained by dividing true weighted signal events by the integrated flux, number of targets, and bin width.

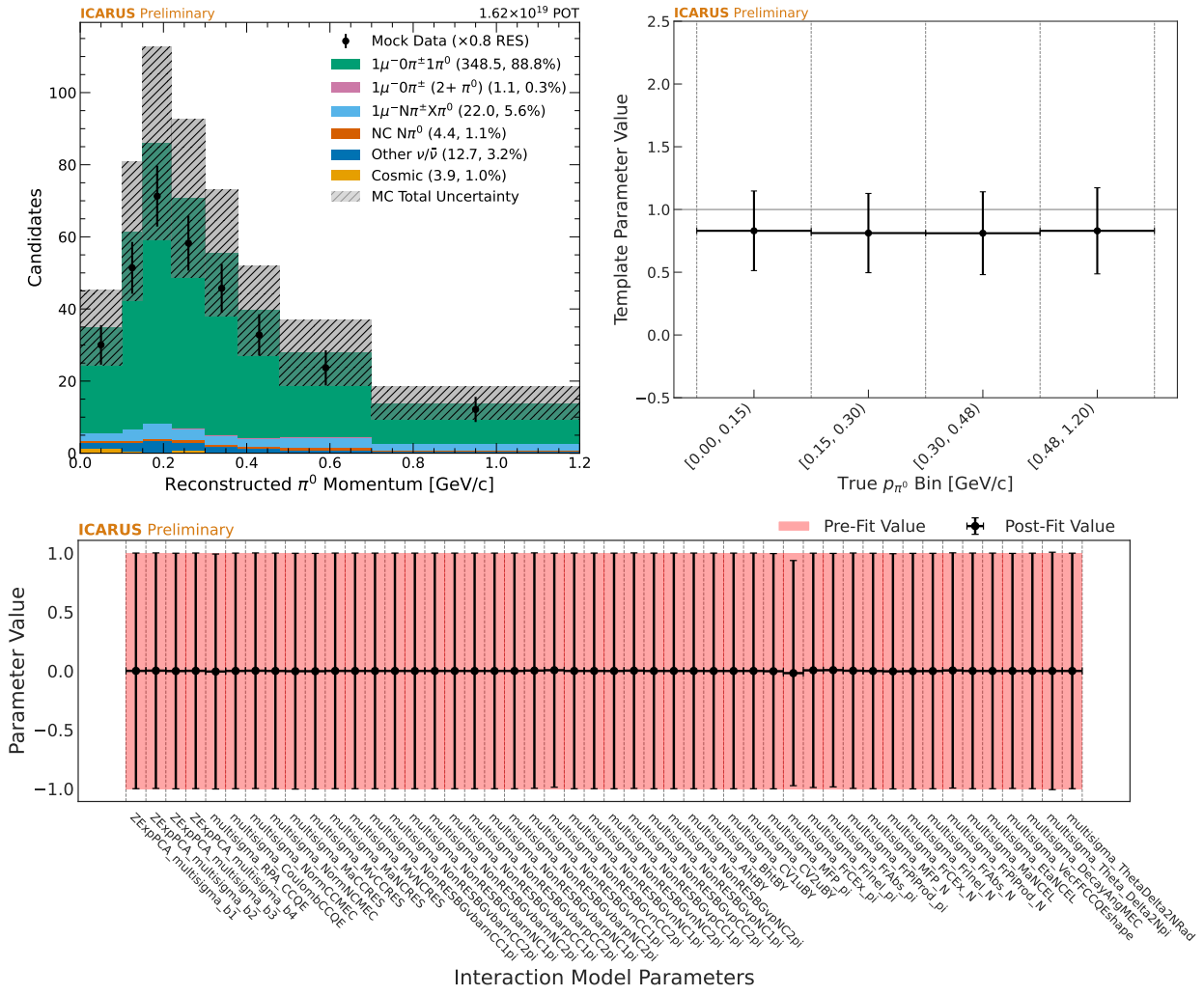

Figure 10.6: Mock data study where GENIE resonance interactions are weighted downward by 20%. Top left: Resultant reconstructed distribution. Top right: Post-fit template parameters. Bottom: Post-fit interaction model parameters.

10.3 Results

Following mock data studies, binned likelihood fits are performed using the unblinded 10% of BNB Run 2 data. The reconstructed distributions of analysis variables used in the fits are the same that were shown previously in Section 9.5. Post-fit template parameter values are shown in Figure 10.9, while interaction model parameters for muon (neutral pion) kinematic observables are shown in Figure 10.10 (10.11). Fit sensitivity is seen for parameters related to resonance production and FSI, as expected for the ν_μ CC π^0 selection.

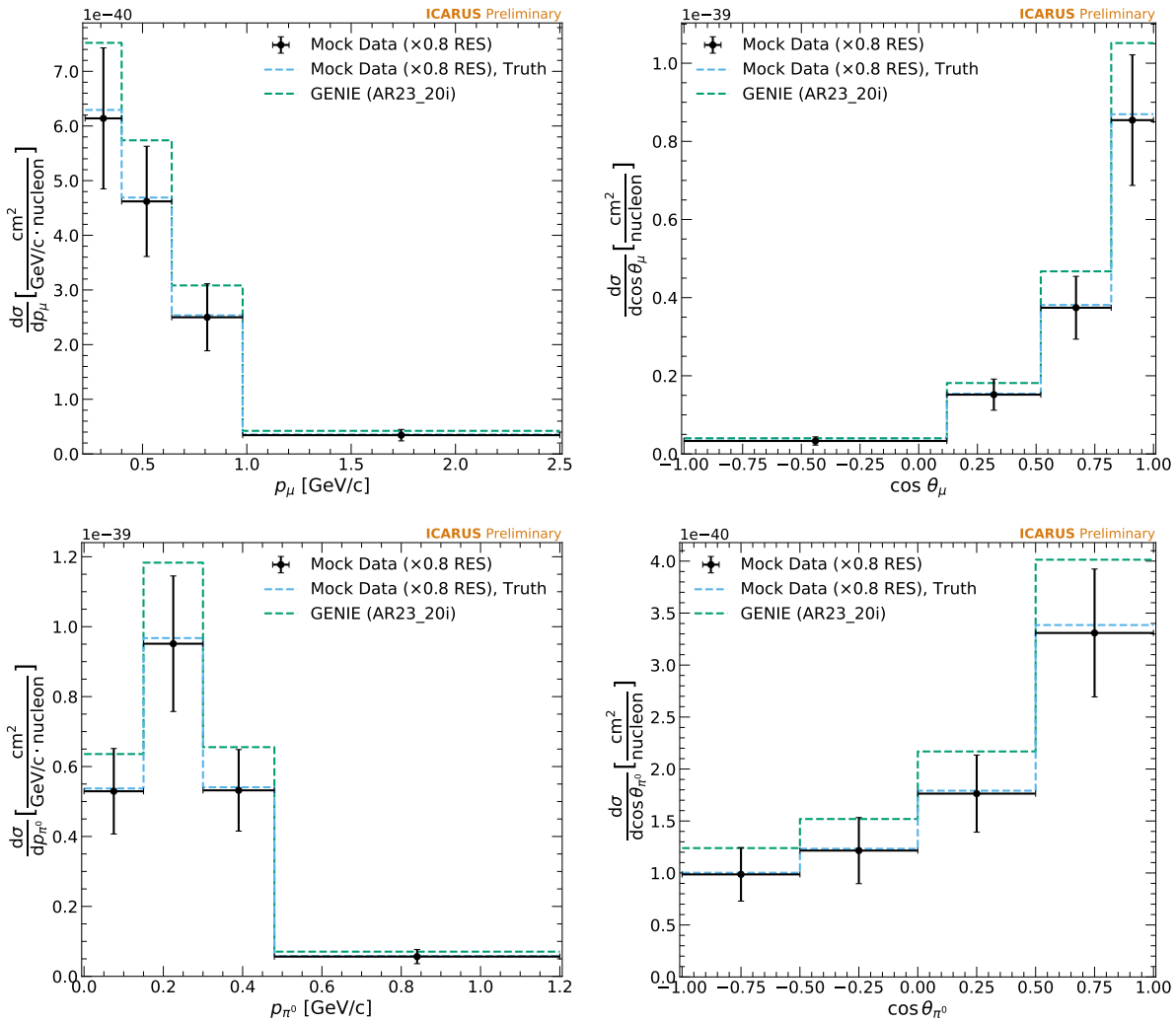

Figure 10.7: Extracted cross sections for mock dataset where resonance interactions have been weighted downward by 20%. Also shown are predicted cross sections as determined from the weighted signal counts (blue dashed line) and reference generator (purple dashed line).

Fit results are validated by comparing the log-likelihood (LLH) from the fit with BNB data against LLHs found from toy dataset fits where observed counts are determined by varying the central value prediction within pre-fit systematic and statistical uncertainties. With one thousand toy datasets, a p-value is calculated as the fraction of toy LLHs greater than or equal to the LLH from the fit with data. Comparisons of the BNB data fit LLH and toy dataset LLH distributions are shown for each analysis variable in Figure 10.12. All p-values are found to be greater than 0.05, leading to the conclusion that the model composed of post-fit parameters is compatible with observations from data.

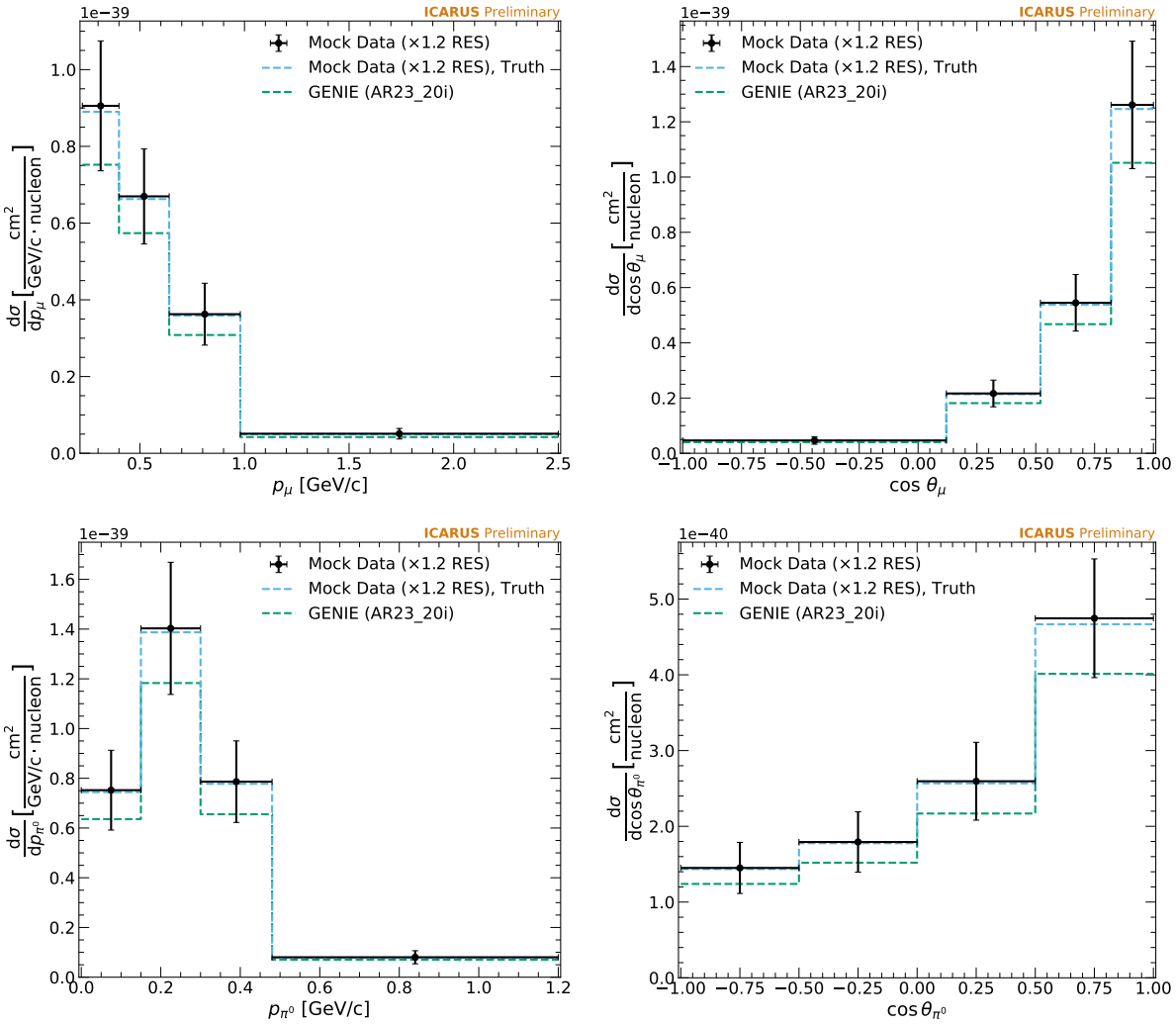

Figure 10.8: Extracted cross sections for mock dataset where resonance interactions have been weighted upward by 20%. Also shown are predicted cross sections as determined from the weighted signal counts (blue dashed line) and reference generator (purple dashed line).

Unfolded signal event counts in each analysis bin are calculated using best-fit parameters according to Equation 10.4, and cross section extraction follows from Equation 10.1. Single-differential cross sections measured with 10% of BNB Run 2 data are presented in Figure 10.13 for muon and neutral pion kinematic observables. The uncertainty reported in each bin is determined by varying best-fit parameter values according to the post-fit covariance matrix in one thousand universes and taking the standard deviation across all universes. While the nature of this error propagation method makes it nontrivial to assess contributions from different uncertainty sources, the analysis is expected to be statistically limited at this time. This can be seen by

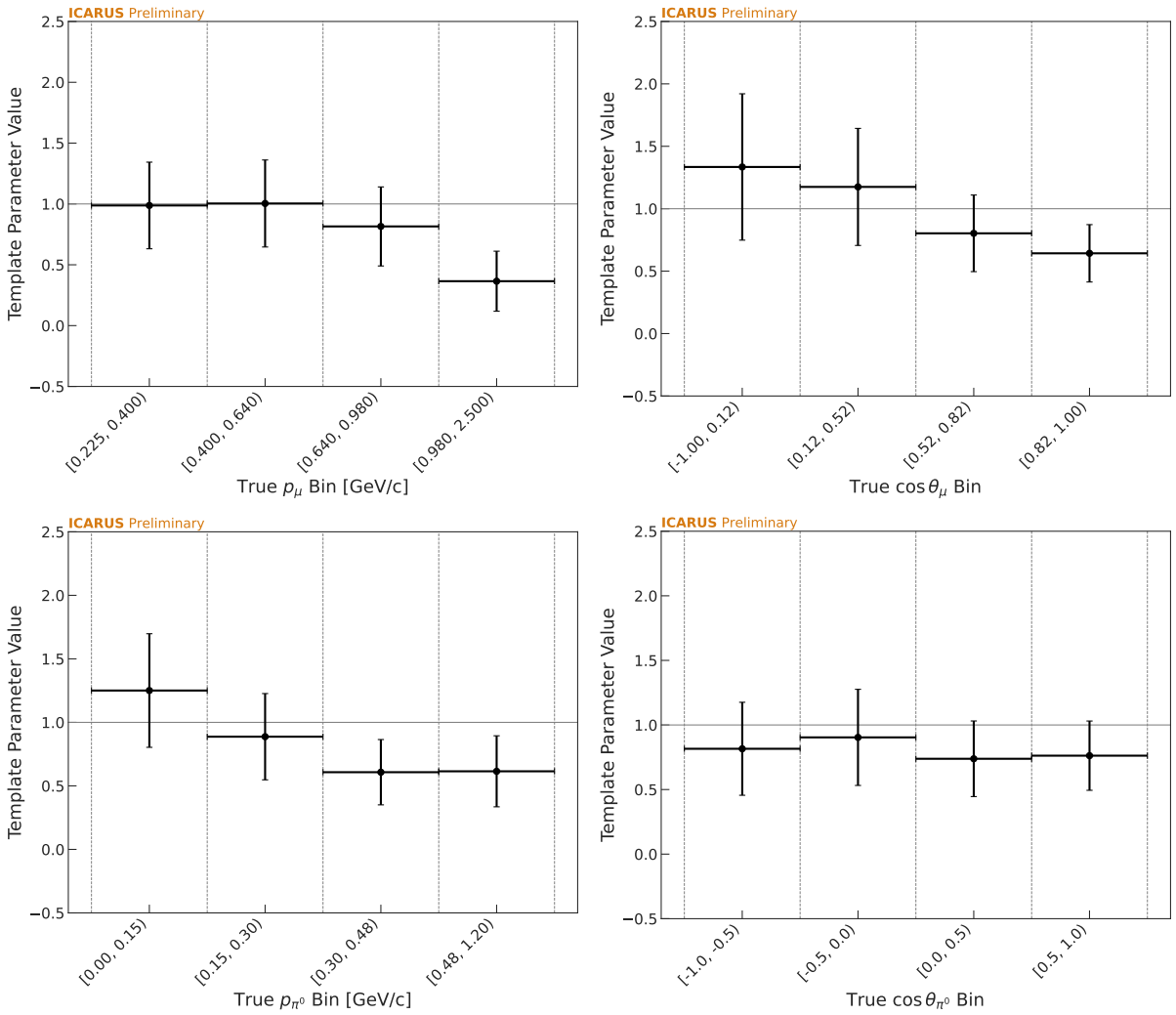

Figure 10.9: Template parameters for muon (top row) and neutral pion (bottom row) kinematic observables from binned likelihood fit with 10% of BNB Run 2 data.

comparing the uncertainty in the standard Asimov fit to that of an Asimov fit with all nuisance parameters excluded. Uncertainty in the latter scenario is taken as the statistical component of the total uncertainty, to which it is compared against in Figure 10.14.

Figure 10.13 also shows how measured cross sections compare against various neutrino event generator predictions. In addition to the reference model GENIE, predictions from NuWro [70], GiBUU [71], and NEUT [72] are included. With regard to resonant neutral pion production, GENIE and NEUT both employ the Berger-Sehgal model while NuWro makes use of the Adler-Rarita-Schwinger formalism. In contrast to the effective INTRANUKE/hA model of FSI used by

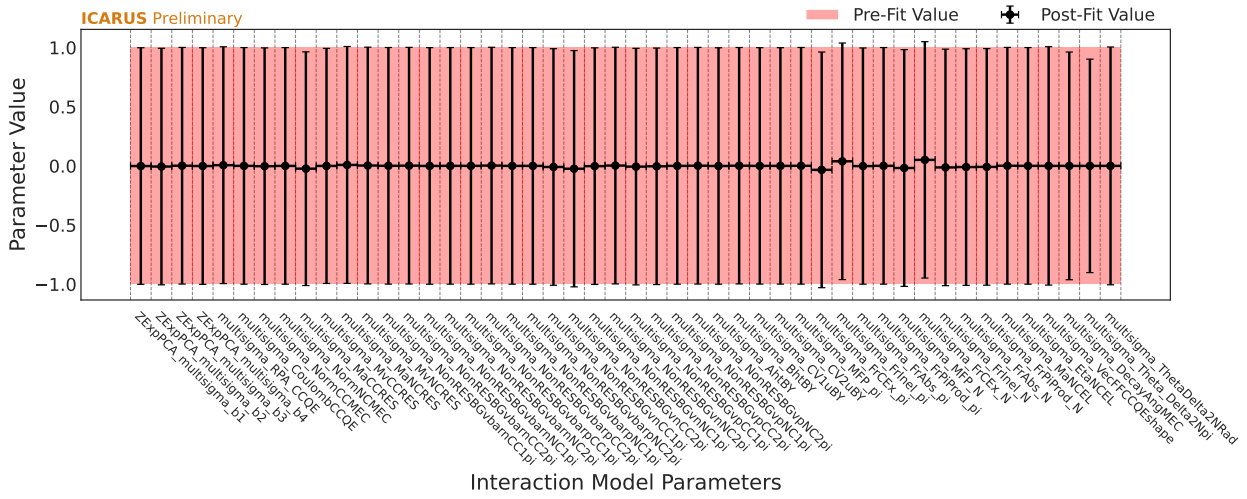

(a) Fit to muon momentum

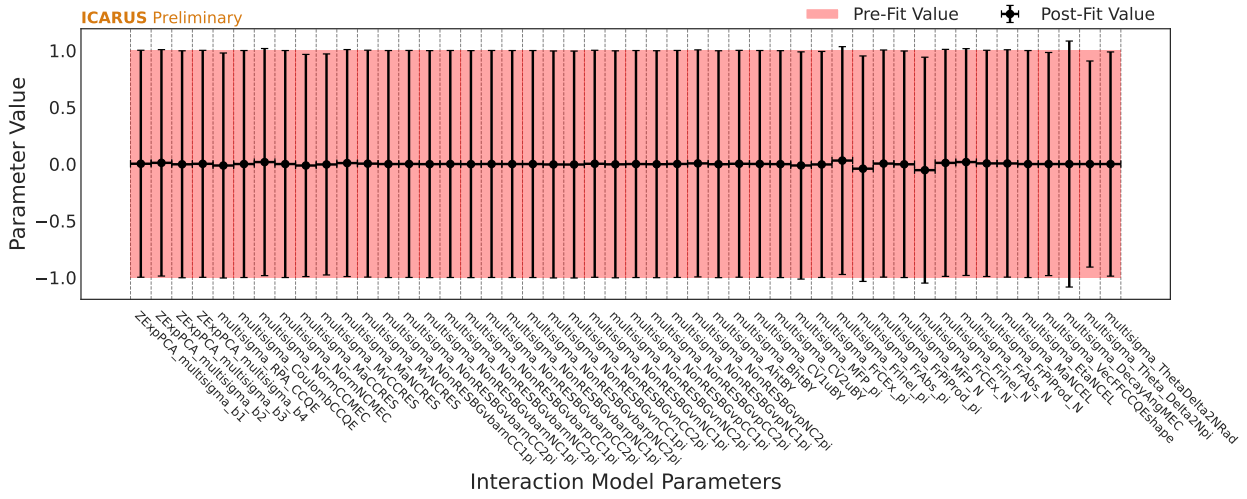

(b) Fit to muon angle relative to BNB direction

Figure 10.10: Neutrino interaction model parameters for muon kinematic observables from binned likelihood fit with 10% of BNB Run 2 data.

GENIE, NuWro and NEUT use different implementations of a semiclassical intranuclear cascade model. Event generation in GiBUU follows a different approach from the other generators entirely, with the hadronic system evolving from the initial point of interaction according to the Boltzmann-Uehling-Uhlenbeck equation. Despite limited statistics, certain trends can still be seen, such as the overprediction of events at forward scattering angles. Upon opening the analysis to the full Run 2 dataset and transitioning to a finer binning scheme, more detailed comparisons to each generator will be made.

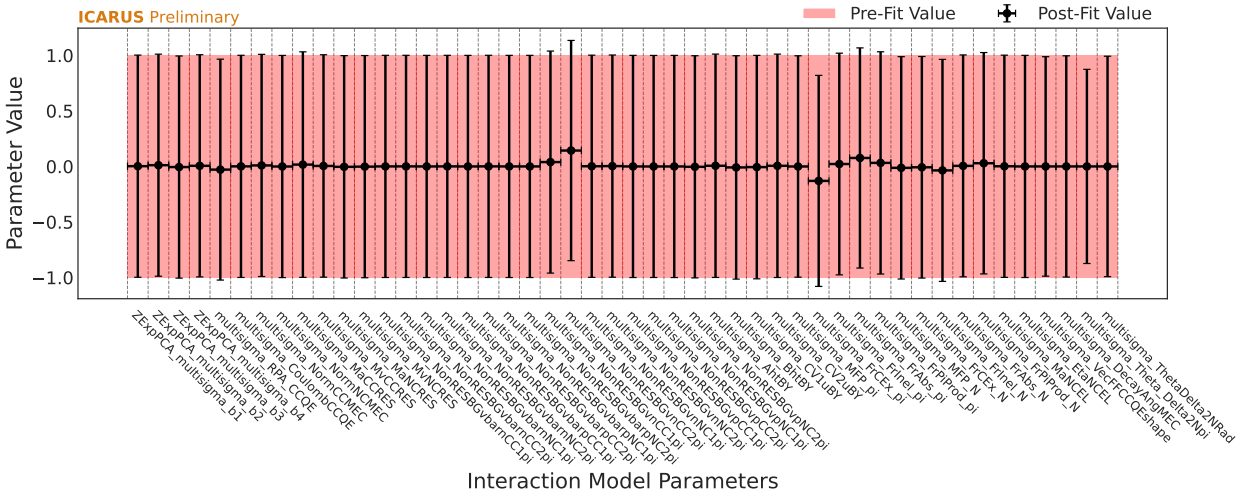

(a) Fit to neutral pion momentum

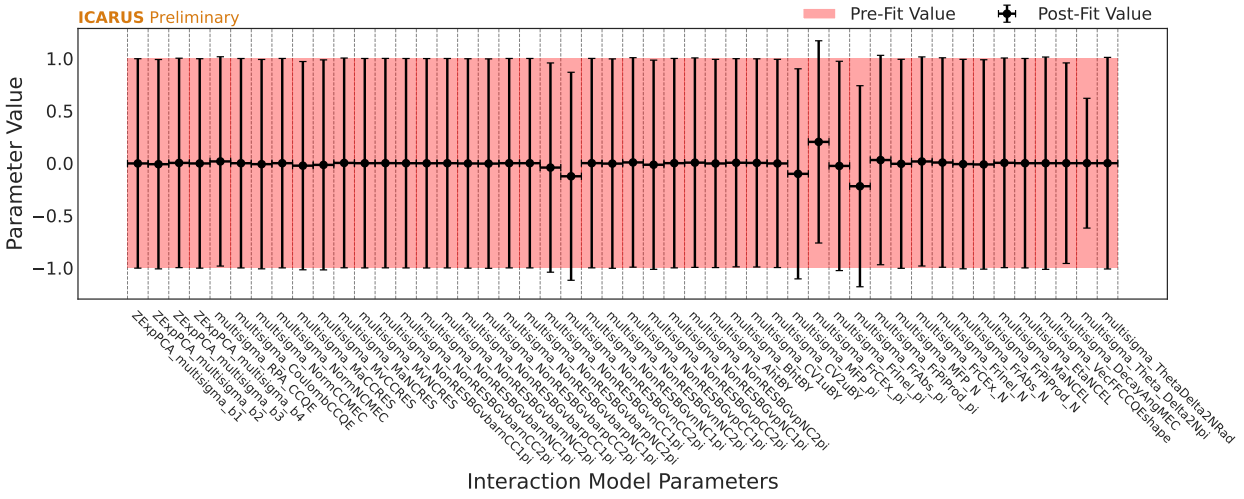

(b) Fit to neutral pion angle relative to BNB direction

Figure 10.11: Neutrino interaction model parameters for neutral pion kinematic observables from binned likelihood fit with 10% of BNB Run 2 data.

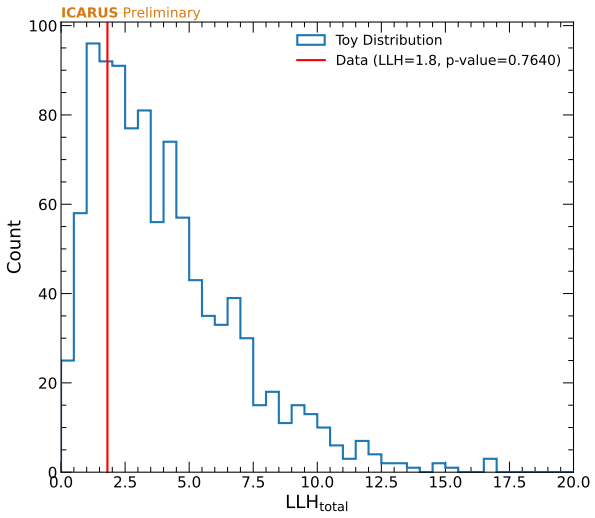

(a) Fit to muon momentum

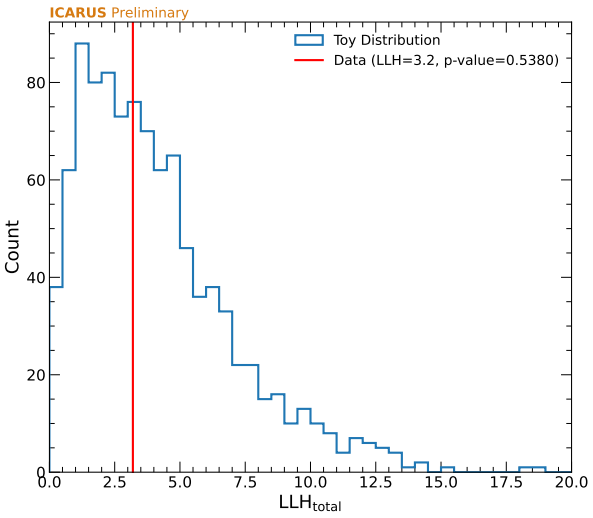

(b) Fit to muon angle relative to BNB direction

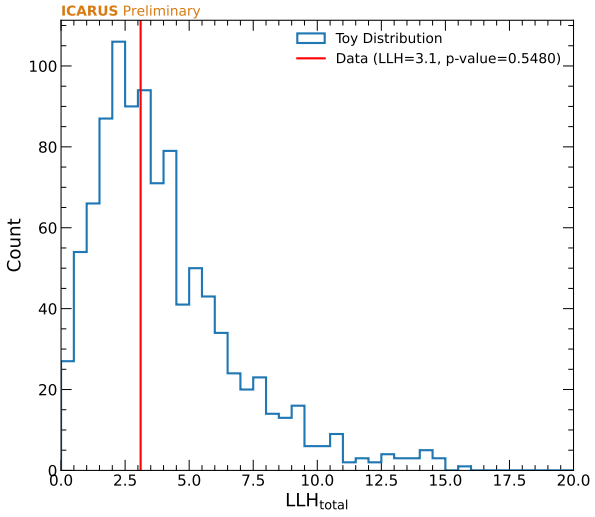

(c) Fit to neutral pion momentum

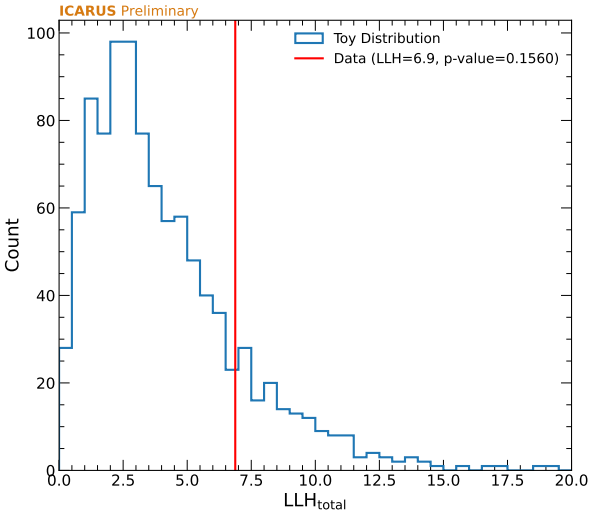

(d) Fit to neutral pion angle relative to BNB direction

Figure 10.12: Log-likelihood (LLH) distribution from toy dataset fits where observed bin counts are determined by varying simulated central value counts within statistical and systematic uncertainties. Also shown is the LLH from the fit using 10% of BNB Run 2 data.

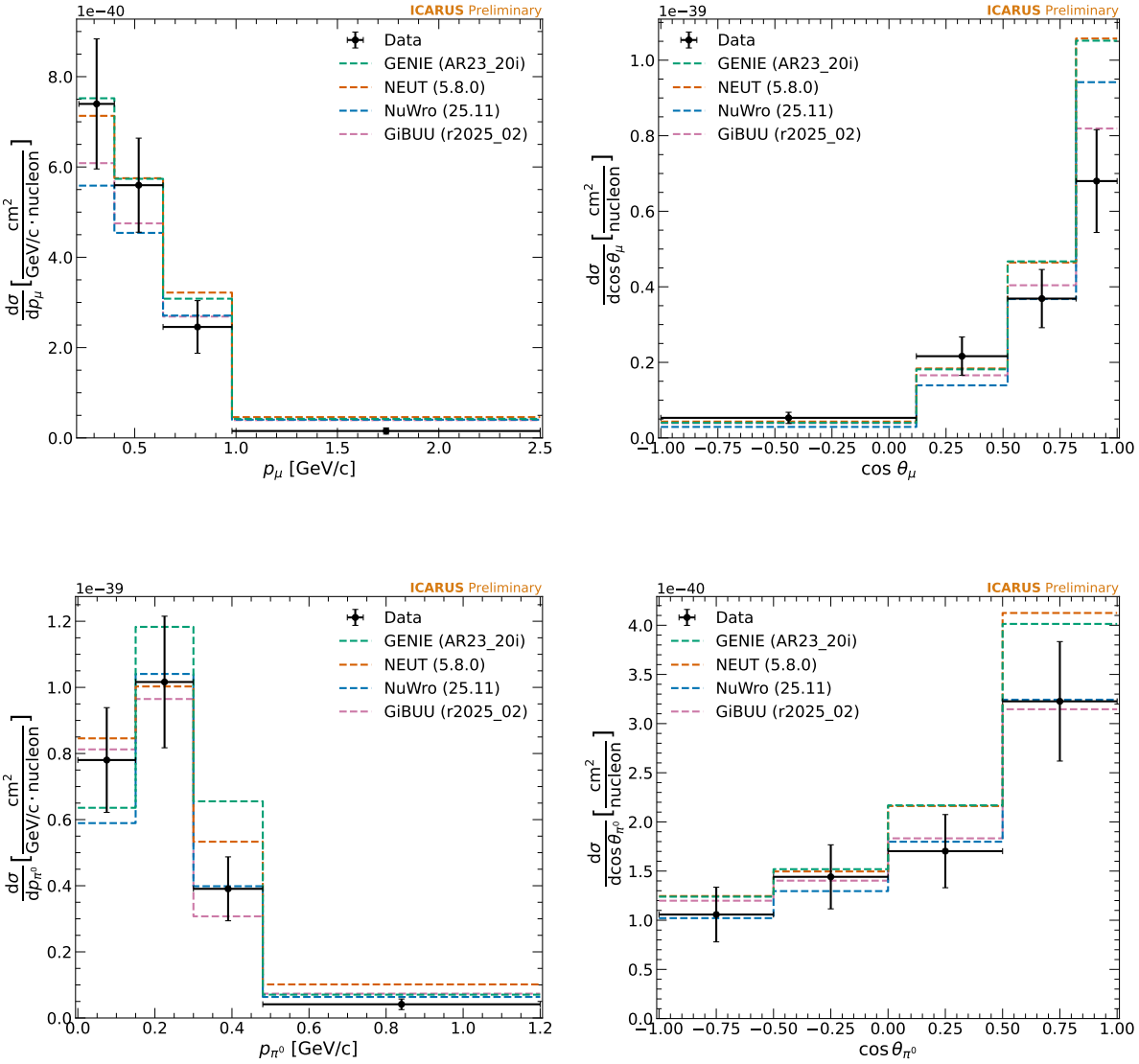

Figure 10.13: Measured cross sections in bins of muon and neutral pion kinematics using 10% of BNB Run 2 data. For comparison, predictions from various neutrino event generators are included and depicted by dashed lines.

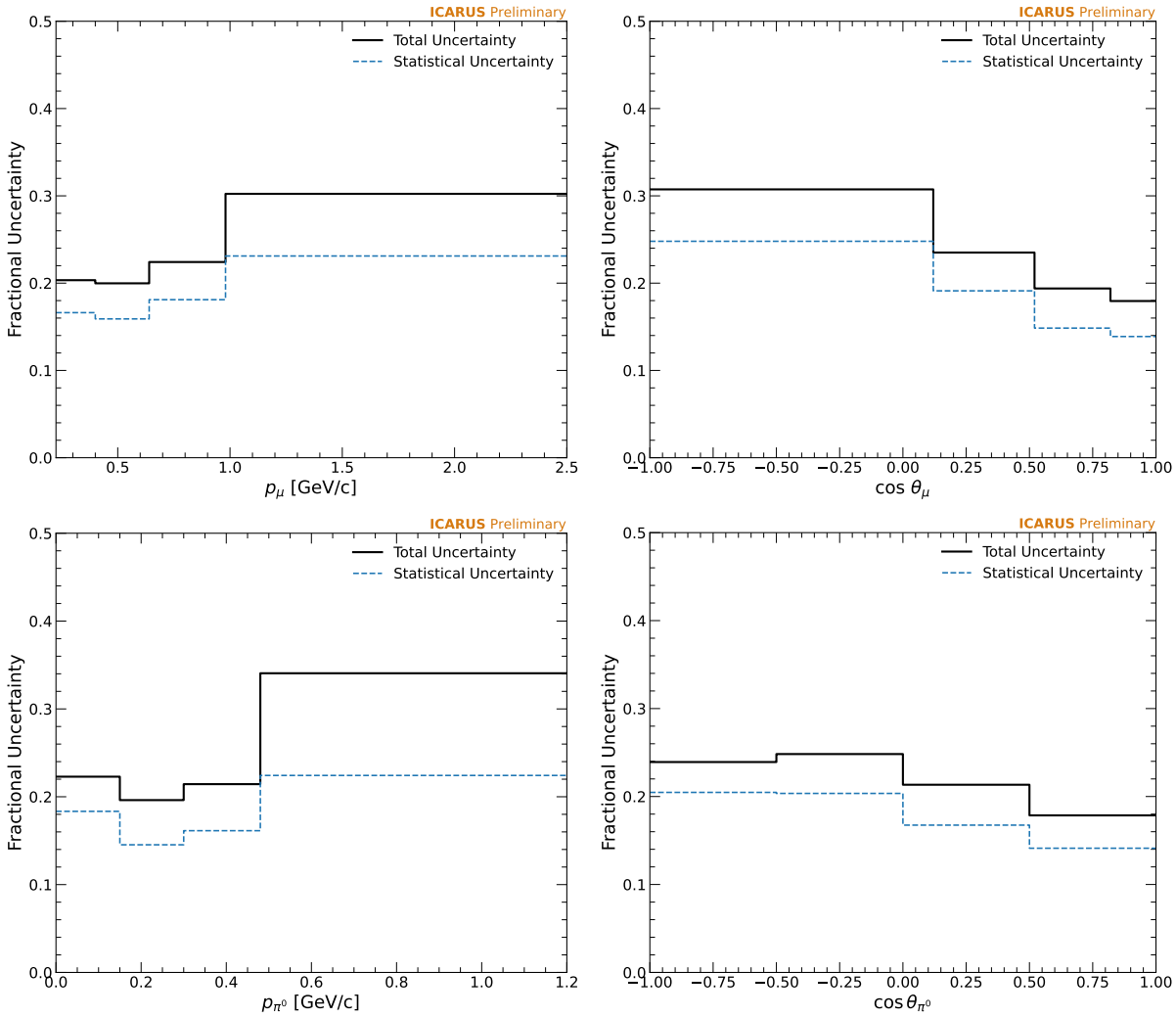

Figure 10.14: Fractional uncertainties on cross section measurements in bins of muon kinematics (top row) and neutral pion kinematics (bottom row). The solid black curve represents the total uncertainty in a standard Asimov fit and the dashed blue line represents the uncertainty in an Asimov fit with no nuisance parameters included.

Chapter 11

Conclusions

The analysis presented in this thesis has demonstrated the selection of charged-current muon neutrino interactions with a single neutral pion in the final state, or ν_μ CC π^0 interactions. This selection makes use of neutrino interaction events recorded with the ICARUS T600 detector at Fermilab while exposed to the Booster Neutrino Beam and highlights the ability to study channels with both track and electromagnetic shower topologies. Benefiting from an intensive detector calibration program and novel machine-learning reconstruction techniques, the efficiency (66%) and purity (89%) of the selection are the highest reported among similar selections at other LArTPC neutrino experiments.

Furthermore, the ν_μ CC π^0 selection has effectuated cross section measurements of these interactions on argon, for which few data points in the field exist. Performing these measurements as functions of muon and neutral pion kinematics has allowed the analysis to identify regions where data is poorly modeled (e.g. forward scattering angles) and enabled comparisons to various neutrino event generators. Having utilized 10% of the ICARUS BNB Run 2 dataset, results shown in this thesis are statistically-limited. Work is ongoing to unblind the entire Run 2 dataset, at which point a more detailed comparison of models will be made.

Above all, it is important to note that the the tools developed for this analysis, from event selection to cross section extraction, are completely detector-agnostic and can be shared between experiments. This is particularly valuable for extending the analysis to SBND, where close proximity to the BNB target enables a rich cross section program with world-leading statistical precision. For context, SBND expects to record over half a million ν_μ CC π^0 interactions per 10^{21} protons on target, corresponding to approximately three years of operation. Measurements of neutral pion production on such a dataset will inform choices in resonance modeling for future experiments like DUNE, where it is expected to be a dominant neutrino interaction mode.

A selection of ν_μ CC π^0 interactions nearly identical to the one presented for ICARUS has been carried out using a small sample of BNB data at SBND. The reconstructed neutral pion mass distribution for this selection is shown in Figure 11.1a. The same distribution is shown for a more recently-developed selection of NC π^0 interactions in Figure 11.1b, highlighting the ability for SPINE to reconstruct challenging topologies without a primary muon. With selection efficiency (purity) already found to be greater than 50% (75%) for both signal channels at SBND through the use of the SPINE machine learning package, the groundwork has been laid to improve upon the results shown in this thesis at the SBN Program in the next several years.

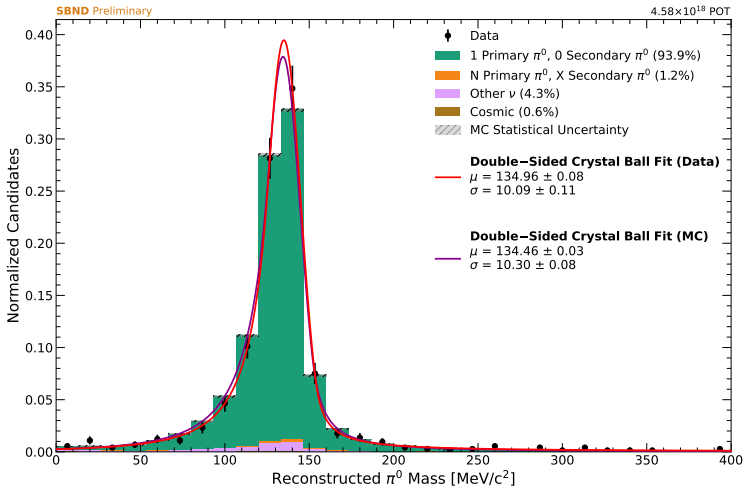

(a) ν_μ CC π^0 Selection

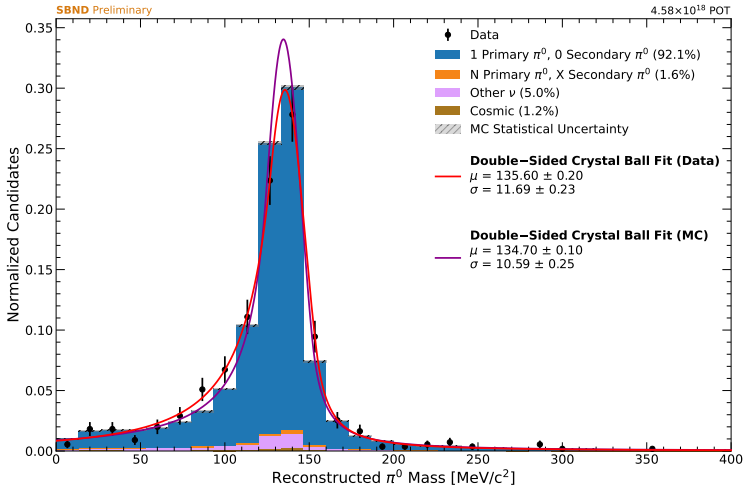

(b) NC π^0 Selection

Figure 11.1: Reconstructed neutral pion mass for ν_μ CC π^0 (a) and NC π^0 (b) selections at SBND using the SPINE machine learning package. Crystal Ball fits are shown for data and simulation, and the mean (μ) and sigma (σ) parameters of the Gaussian component are reported in each case.

Bibliography

[1] J. A. Formaggio and G. P. Zeller, "From eV to EeV: Neutrino Cross Sections Across Energy Scales", Rev. Mod. Phys. **84**, 1307–1341 (2012).

[2] N. Palanque-Delabrouille et al., "Neutrino masses and cosmology with Lyman-alpha forest power spectrum", JCAP **11**, 011 (2015).

[3] C. L. Cowan, F. Reines, F. B. Harrison, H. W. Kruse, and A. D. McGuire, "Detection of the free neutrino: A Confirmation", Science **124**, 103–104 (1956).

[4] C. Mariani et al. (K2K), "Measurement of inclusive π^0 production in the Charged-Current Interactions of Neutrinos in a 1.3-GeV wide band beam", Phys. Rev. D **83**, 054023 (2011).

[5] A. A. Aguilar-Arevalo et al. (MiniBooNE), "Measurement of Neutrino-Induced Charged-Current Charged Pion Production Cross Sections on Mineral Oil at $E_\nu \sim 1$ GeV", Phys. Rev. D **83**, 052007 (2011).

[6] O. Altinok, "Measurement of Muon Neutrino Charged Current Single π^0 Production on Hydrocarbon using MINERvA", PhD thesis (Tufts U., 2017).

[7] P. Abratenko et al. (MicroBooNE), "Measurement of the differential cross section for neutral pion production in charged-current muon neutrino interactions on argon with the MicroBooNE detector", Phys. Rev. D **110**, 092014 (2024).

[8] R. Davis, "A review of the Homestake solar neutrino experiment", Prog. Part. Nucl. Phys. **32**, 13–32 (1994).

[9] Q. R. Ahmad et al. (SNO), "Measurement of the rate of $\nu_e + d \rightarrow p + p + e^-$ interactions produced by ^{8}B solar neutrinos at the Sudbury Neutrino Observatory", Phys. Rev. Lett. **87**, 071301 (2001).

[10] Y. Fukuda et al. (Super-Kamiokande), "Evidence for oscillation of atmospheric neutrinos", Phys. Rev. Lett. **81**, 1562–1567 (1998).

[11] M. Agostini et al. (BOREXINO), "Comprehensive measurement of pp-chain solar neutrinos", Nature **562**, 505–510 (2018).

[12] I. Esteban, M. C. Gonzalez-Garcia, M. Maltoni, I. Martinez-Soler, J. P. Pinheiro, and T. Schwetz, "NuFit-6.0: updated global analysis of three-flavor neutrino oscillations", JHEP **12**, 216 (2024).

[13] E. Richard et al. (Super-Kamiokande), "Measurements of the atmospheric neutrino flux by Super-Kamiokande: energy spectra, geomagnetic effects, and solar modulation", Phys. Rev. D **94**, 052001 (2016).

[14] A. Gando et al. (KamLAND), "Reactor On-Off Antineutrino Measurement with KamLAND", Phys. Rev. D **88**, 033001 (2013).

[15] B. Abi et al. (DUNE), "Long-baseline neutrino oscillation physics potential of the DUNE experiment", Eur. Phys. J. C **80**, 978 (2020).

[16] A. Aguilar et al. (LSND), "Evidence for neutrino oscillations from the observation of $\bar{\nu}_e$ appearance in a $\bar{\nu}_\mu$ beam", Phys. Rev. D **64**, 112007 (2001).

[17] A. A. Aguilar-Arevalo et al. (MiniBooNE), "Updated MiniBooNE neutrino oscillation results with increased data and new background studies", Phys. Rev. D **103**, 052002 (2021).

[18] M. A. Acero et al., "White paper on light sterile neutrino searches and related phenomenology", J. Phys. G **51**, 120501 (2024).

[19] A. Blondel, "The Number of Neutrinos and the Z Line Shape", Adv. Ser. Direct. High Energy Phys. **26**, 145–160 (2016).

[20] M. Bonesini (SBND, MicroBooNe, Icarus), "The Short Baseline Neutrino Program at Fermilab", PoS **NuFact2021**, 009 (2022).

[21] M. A. Acero et al. (NOvA), "New constraints on oscillation parameters from ν_e appearance and ν_μ disappearance in the NOvA experiment", Phys. Rev. D **98**, 032012 (2018).

[22] K. Abe et al. (T2K), "Measurements of neutrino oscillation parameters from the T2K experiment using 3.6×10^{21} protons on target", Eur. Phys. J. C **83**, 782 (2023).

[23] B. Abi et al. (DUNE), "Deep Underground Neutrino Experiment (DUNE), Far Detector Technical Design Report, Volume II: DUNE Physics", (2020).

[24] K. Abe et al. (Hyper-Kamiokande), "Sensitivity of the Hyper-Kamiokande experiment to neutrino oscillation parameters using acceleration neutrinos", (2025).

[25] R. Acciarri et al. (MicroBooNE, LAr1-ND, ICARUS-WA104), "A Proposal for a Three Detector Short-Baseline Neutrino Oscillation Program in the Fermilab Booster Neutrino Beam", (2015).

[26] A. P. Wood, "The NuMI Neutrino Flux Prediction at ICARUS", PhD thesis (Houston U., Houston U., Dec. 2024).

[27] C. Adams et al. (MicroBooNE), "Ionization electron signal processing in single phase LArTPCs. Part I. Algorithm Description and quantitative evaluation with MicroBooNE simulation", JINST **13**, P07006 (2018).

[28] M. J. Berger, J. S. Coursey, M. A. Zucker, and J. Chang, *ESTAR, PSTAR, and ASTAR: Stopping-Power and Range Tables for Electrons, Protons, and Helium Ions*, NIST Physical Measurement Laboratory, Version 1.2.3, Online available: https://physics.nist.gov, Gaithersburg, MD, 2005.

[29] M. J. Berger et al., *XCOM: Photon Cross Section Database (version 1.5)*, National Institute of Standards and Technology, Gaithersburg, MD, [Online] Available: https://physics.nist.gov, 2010.

[30] P. Abratenko et al. (MicroBooNE), "Measurement of space charge effects in the MicroBooNE LArTPC using cosmic muons", JINST **15**, P12037 (2020).

[31] P. Abratenko et al. (MicroBooNE), "Measurement of the flux-averaged inclusive charged-current electron neutrino and antineutrino cross section on argon using the NuMI beam and the MicroBooNE detector", Phys. Rev. D **104**, 052002 (2021).

[32] B. Behera (ICARUS), "Cosmogenic background suppression at the ICARUS using a concrete overburden", J. Phys. Conf. Ser. **2156**, 012181 (2021).

[33] F. A. Alrahman et al. (ICARUS), "Operation of the trigger system for the ICARUS detector at Fermilab", JINST **20**, P10044 (2025).

[34] K. Biery, C. Green, J. Kowalkowski, M. Paterno, and R. Rechenmacher, "artdaq: An Event-Building, Filtering, and Processing Framework", IEEE Trans. Nucl. Sci. **60**, 3764–3771 (2013).

[35] E. L. Snider and G. Petrillo, "LArSoft: Toolkit for Simulation, Reconstruction and Analysis of Liquid Argon TPC Neutrino Detectors", J. Phys. Conf. Ser. **898**, edited by R. Mount and C. Tull, 042057 (2017).

[36] S. Agostinelli et al. (GEANT4), "GEANT4 - A Simulation Toolkit", Nucl. Instrum. Meth. A **506**, 250–303 (2003).

[37] A. A. Aguilar-Arevalo et al. (MiniBooNE), "The Neutrino Flux Prediction at MiniBooNE", Phys. Rev. D **79**, 072002 (2009).

[38] L. Aliaga et al. (MINERvA), "Neutrino Flux Predictions for the NuMI Beam", Phys. Rev. D **94**, [Addendum: Phys.Rev.D 95, 039903 (2017)], 092005 (2016).

[39] NOvA Collaboration, *NuMI flux systematic uncertainties for NOvA third analyses*, Internal Note NOνA-doc-17608 (2017).

[40] M. G. Catanesi et al. (HARP), "Measurement of the production cross-section of positive pions in the collision of 8.9-GeV/c protons on beryllium", Eur. Phys. J. C **52**, 29–53 (2007).

[41] C. Alt et al. (NA49), "Inclusive production of charged pions in p+p collisions at 158-GeV/c beam momentum", Eur. Phys. J. C **45**, 343–381 (2006).

[42] T. Anticic et al. (NA49), "Inclusive production of protons, anti-protons and neutrons in p+p collisions at 158-GeV/c beam momentum", Eur. Phys. J. C **65**, 9–63 (2010).

[43] J. M. Paley et al. (MIPP), "Measurement of Charged Pion Production Yields off the NuMI Target", Phys. Rev. D **90**, 032001 (2014).

[44] C. Andreopoulos et al., "The GENIE Neutrino Monte Carlo Generator", Nucl. Instrum. Meth. A **614**, 87–104 (2010).

[45] D. Rein and L. M. Sehgal, "Neutrino Excitation of Baryon Resonances and Single Pion Production", Annals Phys. **133**, 79–153 (1981).

[46] R. P. Feynman, M. Kislinger, and F. Ravndal, "Current matrix elements from a relativistic quark model", Phys. Rev. D **3**, 2706–2732 (1971).

[47] C. Berger and L. M. Sehgal, "Lepton mass effects in single pion production by neutrinos", Phys. Rev. D **76**, 113004 (2007).

[48] S. Dytman, "Neutrino event generators", AIP Conf. Proc. **896**, edited by M. Albrow and R. Raja, 178–184 (2007).

[49] D. Heck, J. Knapp, J. N. Capdevielle, G. Schatz, and T. Thouw, "CORSIKA: A Monte Carlo code to simulate extensive air showers", (1998).

[50] R. Acciarri et al. (ArgoNeuT), "A Study of Electron Recombination Using Highly Ionizing Particles in the ArgoNeuT Liquid Argon TPC", JINST **8**, P08005 (2013).

[51] P. Abratenko et al. (ICARUS), "Angular dependent measurement of electron-ion recombination in liquid argon for ionization calorimetry in the ICARUS liquid argon time projection chamber", JINST **20**, P01033 (2025).

[52] C. Adams et al. (MicroBooNE), "Ionization electron signal processing in single phase LArTPCs. Part II. Data/simulation comparison and performance in MicroBooNE", JINST **13**, P07007 (2018).

[53] R. Veenhof, "GARFIELD, recent developments", Nucl. Instrum. Meth. A **419**, edited by M. Krammer, G. Neuhofer, M. Regler, and A. Taurok, 726–730 (1998).

[54] P. Abratenko et al. (ICARUS), "Calibration and simulation of ionization signal and electronics noise in the ICARUS liquid argon time projection chamber", JINST **20**, P01032 (2025).

[55] D. H. Koh, *2D Classical ROI Finding*, Internal Note SBN-doc-20606 (2021).

[56] R. Acciarri et al. (MicroBooNE), "The Pandora multi-algorithm approach to automated pattern recognition of cosmic-ray muon and neutrino events in the MicroBooNE detector", Eur. Phys. J. C **78**, 82 (2018).

[57] F. Drielsma, K. Terao, L. Dominé, and D. H. Koh, "Scalable, End-to-End, Deep-Learning-Based Data Reconstruction Chain for Particle Imaging Detectors", (2021).

[58] O. Ronneberger, P. Fischer, and T. Brox, "U-Net: Convolutional Networks for Biomedical Image Segmentation", (2015).

[59] V. L. Highland, "Some Practical Remarks on Multiple Scattering", Nucl. Instrum. Meth. **129**, 497 (1975).

[60] M. Oreglia, "A Study of the Reactions $\psi' \to \gamma\gamma\psi$", Other thesis (Dec. 1980).

[61] M. Mooney, S. Ruterbories, and A. Mogan, *Measurement of the Transverse and Longitudinal Diffusion of Ionization Electrons in Liquid Argon with the ICARUS Detector*, tech. rep. SBN-doc-28805 (2025).

[62] N. Gee, M. A. Floriano, T. Wada, S. S.-S. Huang, and G. R. Freeman, "Ion and electron mobilities in cryogenic liquids: argon, nitrogen, methane, and ethane", Journal of Applied Physics **57**, 1097–1101 (1985).

[63] S. Palestini and F. Resnati, "Space charge in liquid argon time-projection chambers: a review of analytical and numerical models, and mitigation methods", JINST **16**, P01028 (2021).

[64] S. Amerio et al. (ICARUS), "Design, construction and tests of the ICARUS T600 detector", Nucl. Instrum. Meth. A **527**, 329–410 (2004).

[65] M. A. Pons et al., *ICARUS BNB ν_μ Disappearance Technical Note*, tech. rep. SBN-doc-28805 (2025).

[66] P. Abratenko et al. (MicroBooNE), "Measurement of nuclear effects in neutrino-argon interactions using generalized kinematic imbalance variables with the MicroBooNE detector", Phys. Rev. D **109**, 092007 (2024).

[67] G. D'Agostini, "A Multidimensional unfolding method based on Bayes' theorem", Nucl. Instrum. Meth. A **362**, 487–498 (1995).

[68] W. Tang, X. Li, X. Qian, H. Wei, and C. Zhang, "Data Unfolding with Wiener-SVD Method", JINST **12**, P10002 (2017).

[69] GUNDAM Organization, *Gundam*, https://github.com/gundam-organization/gundam.

[70] T. Golan, J. T. Sobczyk, and J. Zmuda, "NuWro: the Wroclaw Monte Carlo Generator of Neutrino Interactions", Nucl. Phys. B Proc. Suppl. **229-232**, edited by G. S. Tzanakos, 499–499 (2012).

[71] O. Buss et al., "Transport-theoretical Description of Nuclear Reactions", Phys. Rept. **512**, 1–124 (2012).

[72] Y. Hayato and L. Pickering, "The NEUT neutrino interaction simulation program library", Eur. Phys. J. ST **230**, 4469–4481 (2021).